Masteroppgave

NTNU
Norges teknisk-naturvitenskapelige universitet
Fakultet for naturvitenskap
Institutt for materialteknologi

Vegard Gjeldvik Jervell

The Kinetic Gas Theory of Mie fluids

Exploring Gas-Phase Thermal Diffusion with Kinetic Gas Theory and Thermodynamic Considerations

Masteroppgave i Industriell Kjemi og Bioteknologi
Veileder: Øivind Wilhelmsen
Medveileder: Vilde Bråten

Juni 2022

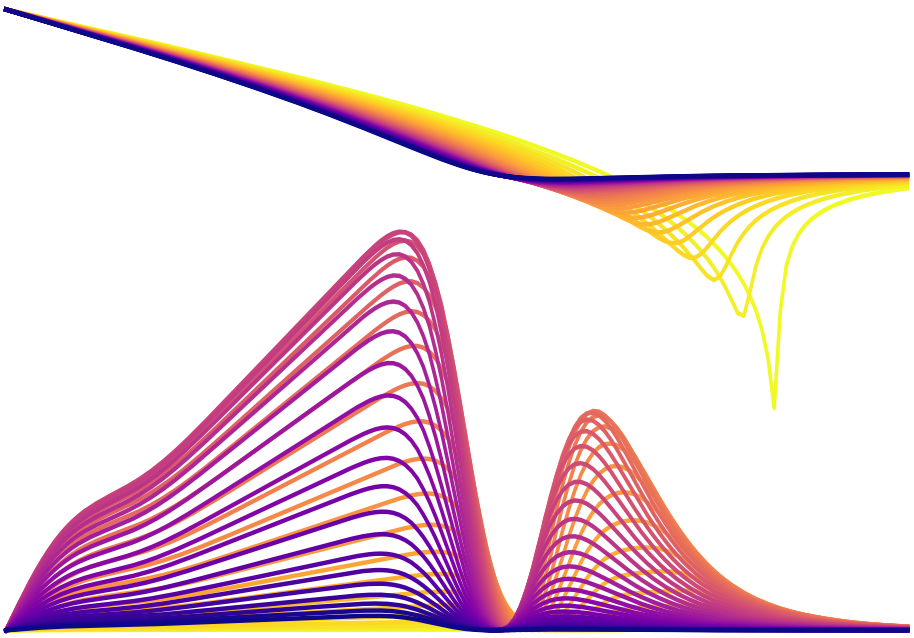

NTNU
Kunnskap for en bedre verden

Vegard Gjeldvik Jervell

The Kinetic Gas Theory of Mie fluids

Exploring Gas-Phase Thermal Diffusion with Kinetic Gas Theory and Thermodynamic Considerations

Masteroppgave i Industriell Kjemi og Bioteknologi
Veileder: Øivind Wilhelmsen
Medveileder: Vilde Bråten
Juni 2022

Norges teknisk-naturvitenskapelige universitet
Fakultet for naturvitenskap
Institutt for materialteknologi

NTNU

Kunnskap for en bedre verden

Sammendrag

Termisk diffusjon er et facinerende fenomen med mange mulige, fremtidige anvendelsesområder. Fenomenet observeres i blandinger som utsettes for en termisk gradient, hvor denne gradienten kan drive en massefluks. Det ble først oppdaget av C. Ludwig, og senere undersøkt nærmere av C. Soret allerede sent på 1800-tallet. Siden den gang har mye forskning blitt investert i å forsøke å forstå og beskrive det som nå ofte kalles Soret-effekten. Ikke minst har man lenge forsøkt å utvikle modeller for å kunne kvantitativt prediktere hvor sterkt masse- og varmestransport kobler i et gitt system. Likevel har til dags dato ingen generelt anvendbar og pålitelig modell blitt presentert i den åpne litteraturen.

Moderne utvikling innen både nano- og bioteknologi, samt hydrogen- og CO_2 lagring, energiteknologi og kjernekraft vil ha stor nytte av muligheten til å prediktere virkningen av termisk diffusjon. Derfor har dette arbeidet undersøkt to forskjellige fremgangsmåter for å modellere termisk diffusjon.

Enskog-løsningene til Boltzmannlikningene for hardkulesystemer har tidligere blitt vist å gi gode prediksjoner for transportkoeffisienter i lavtetthetsregimet. I dette arbeidet evalueres Enskog-løsningene for Mie fluider. Dette resulterer i svært nøyaktige og pålitelige prediksjoner for transportkoeffisienter i gassfasen. Det vises at Mie-potensial-parametre tilpasset til likevektsdata ved bruk av SAFT-tilstandslikninger kan brukes i kombinasjon med Enskog-løsningene for å prediktere transportkoeffisienter med høy nøyaktighet. Dermed kan Enskog-løsningene for Mie-fluider brukes som et bindeledd mellom modellering av likevekts- og ikke-likevektsfenomen.

Prediksjonene til Enskog-løsningene for Mie-fluider har blitt sammenliknet med prediksjonene for harde kuler. Det demonstreres at løsningene for Mie-fluider fanger opp både temperatur- og sammensetningsavhengigheter som ikke fanges opp av løsningene for harde kuler. Fordi disse avhengighetene fanges opp, gir denne nye implementasjonen en vesentlig bedre representasjon av virkelige systemer enn de mer hyppig brukte hardkuleløsningene.

I nylige arbeider har det blitt vist at en modell foreslått av Kempers for prediksjon av Soretkoeffisienten er upålitelig. Den nye implementasjonen av Enskog-løsningene for Mie-fluider har blitt brukt for å undersøke antakelsene bak Kempers-modellen i detalj. Det vises at antakelsene vedrørende sammenhengen mellom kinetisk gassteori, likevektstermodynamikk og den stasjonære tilstanden etter all sannsynlighet ikke holder. Følgelig bør fremtidige forsøk på å utvikle universelle modeller for Soretkoeffisienten fokusere på andre fremgangsmåter, heller enn å forsøke å utbedre Kempers-modellen.

Abstract

Thermal diffusion is an intriguing phenomenon with an extensive list of possible applications. The effect is that in which a temperature gradient drives a mass flux, originally discovered by Ludwig and investigated further by Soret already in the late 19th century. Much research has gone into understanding this effect, and specifically into quantitatively predicting the coupling coefficient between heat and mass transport, still, no universally reliable model has so far been presented in the open literature.

Current developments within nano-engineering, bio-processing, hydrogen and CO_2 storage and energy- and nuclear technology all warrant the development of an ability to accurately predict the effects of thermal diffusion in complex systems. Thus, this work will investigate more closely two approaches to modelling thermal diffusion.

The Enskog solutions to the Boltzmann equations for hard sphere systems have been shown to give accurate predictions in the low density regime. In this work, explicit evaluation of the collision integrals using Mie potentials is shown to produce highly accurate predictions of transport coefficients in the gas phase. Mie potential parameters obtained by regressing SAFT-type equations of state to equilibrium properties are revealed to give reliable predictions of transport coefficients when used with the Enskog solutions for Mie fluids. This provides a powerful link between the modelling of equilibrium and non-equilibrium properties using the same molecular interaction parameters and mixing rules.

The predictions obtained from the Enskog solutions for Mie fluids are compared to those obtained for hard spheres. It is found that the solutions for Mie fluids capture both temperature- and compositional effects that are not captured by the hard sphere solutions. This new implementation represents a significant improvement compared to the more commonly used solutions for hard spheres.

In a recent work, a specific model proposed by Kempers has been shown to give highly unreliable predictions of the Soret coefficient. The new implementation of the Enskog solutions for Mie fluids is used to investigate the underlying assumptions behind the Kempers model, and it is found that these assumptions likely do not hold. This analysis shows that future development of models for the Soret coefficient in the liquid phase should follow other approaches than that used by Kempers.

Forord

Jeg innser når jeg skriver dette at denne oppgaven på mange måter er kulminasjonen av ikke bare et femårig masterløp, men et attenårig utdanningsløp og tjuefem år med erfaringer, tilfeldigheter og påvirkninger. Det er flere samtaler, opplevelser og mennesker enn jeg kan telle som til sammen har ført til at jeg sitter akkurat her, akkurat nå, og skriver denne oppgaven. Og for å være helt tydelig: Jeg er utrolig glad for at det er akkurat her jeg har endt opp. Med det vil jeg gjerne takke dere som har hjulpet meg på veien.

Jeg vil begynne med å takke Øivind, for at han dro meg med inn i kaninhullet som er teoretisk kjemi allerede høsten i fjerdeklasse, og siden både har vist meg nye kaninhull og trukket meg ut av dem når jeg begynner å grave for dypt til å komme meg opp selv. Videre vil jeg takke alle dere som har gjort studietiden til de beste fem årene jeg kunne tenkt meg, dere som legger ned dag og natt for å holde studentkulturen levende, enten det er på fotballbanen, på kontoret, på tur eller på fest. Dere skaper, har skapt, og har inkludert meg i, et fantastisk miljø som jeg aldri hadde kommet meg gjennom studietiden uten. Det har vært en ære og en glede å bli kjent med dere.

Så vil jeg takke dere som gjorde at jeg endte opp her i Trondheim i første omgang. Farmor, for samtalene ved kjøkkenbordet i Lyngåsveien hvor du vekket til live en interesse for alt som er vanskelig å forklare, og Farfar for de morsomme historiene om hvordan det kan gå når man bestemmer seg for å ta en grad i kjemi. Bestefar for at du har vist meg hvor spennende verden er når du aldri slutter å interessere deg for alt mellom himmel og jord, og Mormor for den tryggheten og varmen det er å vite at jeg alltid får mer kost og losji enn jeg har plass til når jeg er hos deg. Jeg vil takke Mamma og Pappa for en konstant støtte fra da jeg ville bli skuespiller, til fotballspiller, til økonom og til slutt kjemiker. Uansett hva det har dreid seg om har dere alltid stilt opp, enten med å hjelpe meg på veien eller å minne meg på å ta en pause med en tur på fjellet eller sjøen. Jeg tror den støtten har vært helt avgjørende for at jeg endte opp med å drive med noe jeg virkelig synes er spennende.

Til slutt vil jeg takke Alexandra, for at du alltid er her, og gjør hver eneste dag til en solskinnsdag. Enten du ringer meg på lesesalen, kommer på besøk, eller forteller om alt det du har planlagt at vi skal gjøre, er det en glede i deg som er så smittsom at jeg ikke kan annet enn å være lykkelig. Jeg gleder meg til å våkne hver dag, og vite at jeg får enda en dag med deg.

Til alle dere som har gjort de siste tjuefem årene til den reisen det har vært, tusen takk.

Symbols and abbreviations

Here an exhaustive list of all mathematical symbols used in this text, and their definitions, is collected. Notation wise, boldface roman font, such as $\mathbf{U}$ is used for vectors, and calligraphic font, $\mathscr{U}$ is used for dimensionless quantities, except in the case of dimensionless state variables, which are denoted with a star, such as T^*. The length of a vector $\mathbf{U}$ is denoted in serif font as U. Matrices are denoted with underlined boldface symbols, such as $\underline{\boldsymbol{B}}$.

The symbols φ and ψ are reserved to indicate arbitrary, or placeholder, variables and functions respectively.

Due to the large volume of notation, a few symbols carry several definitions, these are summarised at the end of the table to facilitate differentiating them based on context.

Symbols used in the text

Symbol	Description	Unit
A	Helmholtz energy	J
$A_{pqr\ell}, A'_{pqrl}, A'''_{pqr\ell}$	Specific scalar values, see Section 2.3.6	–
a_{pq}	Specific integrals, see Eq. 2.83	$\mathrm{m^3\,s^{-1}}$
$\mathbf{a}_i^{(p)}$	Specific Sonine polynomials, see Eq. (2.74)	–
b	Impact parameter, see Figures 2.1 and 2.2	m
D_{ij}	Diffusion coefficient	$\mathrm{mol\,m^{-2}\,s^{-1}}$
$\hat{D}$	Predicted diffusion coefficient	$\mathrm{mol\,m^{-2}\,s^{-1}}$
D_T	Thermal diffusion coefficient	$\mathrm{mol\,m^{-2}\,s^{-1}}$
$\mathbf{D}$	Velocity distribution response to $\mathbf{d}_{12}$, see Eq. (2.56)	m
$\mathbf{d}_{12}$	Specific driving force, see Eq. 2.55	$\mathrm{m^{-1}}$
d_p	Sonine polynomial expansion coefficient, see Eq. (2.71)	m
$\mathbf{F}$	Force	N
f	Exact velocity distribution function (vdf.)	$\mathrm{s^3\,m^{-6}}$
$f^{(r)}$	r-th approximation term to the vdf.	$\mathrm{s^3\,m^{-6}}$
$\mathbf{g}$	Relative particle velocity	$\mathrm{m\,s^{-1}}$
g	Relative particle speed	$\mathrm{m\,s^{-1}}$
$\mathscr{g}$	Dimensionless relative particle speed	–
H	Enthalpy	J
$H_1^{(1)}, H_{12}^{(1)}, H_{12}^{(12)}$	Specific bracket integrals, see Eq. (2.89)	–
h	Molar enthalpy	$\mathrm{J\,mol^{-1}}$
h_i	Partial molar enthalpy of species i	$\mathrm{J\,mol^{-1}}$
h_x, h_y	Integration step, $h_x = N_x\delta_x$, $h_y = N_y\delta_y$	–
I	Several specific integrals, see Eq. (2.40)	*
$\mathbf{J}_i$	Mass flux of species i	$\mathrm{mol\,m^{-2}\,s^{-1}}$
$\mathbf{J}_q$	Measurable heat flux	$\mathrm{W\,m^{-2}}$
J	Several specific integrals, see Eq. (2.24)	$\mathrm{m^{-1}}$
k_B	Boltzmann constant	$\mathrm{J\,K^{-1}}$
k_T	Thermal diffusion ratio	–
k_{ij}, ℓ_{ij}	Modified Lorentz-Berthelot mixing rule parameters	–

* Various units

Continued

Symbol	Description	Unit
L	Onsager phenomenological coefficient	$*$
$\mathcal{L}$	Lagrange target function	$*$
l_p	Sonine polynomial expansion coefficient, see Eq. (2.71)	m
M_i	m_i/m_0	–
m_i	Molar or particle mass of species i	$\mathrm{g\,mol^{-1}}$ or kg
m_0	Sum of particle masses	kg
	Number of species	–
N	Order of approximation	–
	Number of intervals	–
N_A	Avogadros number	$\mathrm{mol^{-1}}$
N_x, N_y	Multiple of minimum integration step, δ_x, δ_y	–
n	Total moles in system	mol
n_i	Moles of species i	mol
$\mathbf{n}$	Vector of all mole numbers in system	mol
p	Pressure	Pa
Q	Canonical partition function	–
R	Distance of closes approach between particles, see Figure 2.5	m
	Universal gas constant	$\mathrm{J\,mol^{-1}\,K}$
$\mathbf{r}$	Positional vector	m
r	Polar coordinate radial position	m
S	Entropy	$\mathrm{J\,K^{-1}}$
S_T	Soret coefficient	$\mathrm{K^{-1}}$
$S_m^{(n)}$	Sonine polynomial	$*$
$\mathcal{S}$	Integration domain	–
$\mathcal{S}^*$	Discretised integration domain	–
$\mathcal{S}_{ij}^*$	Continuous subdomain of $\mathcal{S}^*$, see Eq. (3.19)	–
$\mathcal{S}_{ij}^\Delta$	Discretisation of $\mathcal{S}_{ij}^*$, see Eq. (3.19)	–
$\mathcal{S}_{ij}^x, \mathcal{S}_{ij}^{xy}, \mathcal{S}_{ij}^y$	Specific domain mappings, see Eq. (3.22)	–
T	Thermodynamic temperature	K
t	Time	s
U_i	Peculiar speed of particles of species i	$\mathrm{m\,s^{-1}}$
$\mathbf{U}_i$	Peculiar velocity of particles of species i, $\mathbf{u}_i - \mathbf{u}^n$	$\mathrm{m\,s^{-1}}$
$\bar{U}_i$	Average peculiar speed of particles of species i	$\mathrm{m\,s^{-1}}$
$\mathscr{U}$	Dimensionless peculiar speed of particles of species i	–
$\mathbf{u}^n$	Mole average velocity of system	$\mathrm{m\,s^{-1}}$
u_i	Speed of particles of species i	$\mathrm{m\,s^{-1}}$
$\bar{u}_i$	Average speed of particles of species i	$\mathrm{m\,s^{-1}}$
$\mathbf{u}_i$	Velocity of particles of species i	$\mathrm{m\,s^{-1}}$
u_{p-HS}	Pseudo hard-sphere potential, defined in Eq. (3.30)	J
u^{Mie}	Mie potential, defined in Eq. (2.13)	J
V	Volume	$\mathrm{m^3}$
v	Molar volume	$\mathrm{m^3\,mol^{-1}}$

* Various units

Continued

Symbol	Description	Unit
v_i	Partial molar volume of species i	$\mathrm{m^3\,mol^{-1}}$
$W_{ij}^{(\ell)}(r)$	Dimensionless collision integral, see Eq. (2.91)	–
x_i	Mole fraction of species i	–
$\mathbf{x}$	Vector of all mole fractions in the system	–
x, y, z	Cartesian coordinates	–
Z	Compressibility factor	–
α_T	Thermal diffusion factor	–
α_q	Value of specific integrals, see Eq. (2.78)	$\mathrm{m^4 s^{-1}}$
Γ	Gamma function	–
γ, ϕ	Lagrange multipliers	–
δ_q	Value of specific integrals, see Eq. (2.76)	$\mathrm{m^4 s^{-1}}$
δ_{ij}	Kronecker delta	–
δ_x, δ_y	Minimum integration step	–
ϵ	Angular collision coordinate, see Figure 2.2	–
	Small number, identified by sub- and superscripts	*
ε	Mie potential well depth	J
$\hat{\epsilon}$	Descriptor for deviation	–
η	Packing fraction	–
θ	Angular collision coordinate, see Figure 2.1	–
Λ	Thermal response function, see Eq. (2.47)	$\mathrm{K\,s}$
$\mathbf{\Lambda}$	Velocity distribution function response to $\nabla \ln T$	$\mathrm{K\,m}$
$\tilde{\mathbf{\Lambda}}$	$\mathbf{\Lambda} - k_T \mathbf{D}$	
λ	Thermal conductivity	$\mathrm{W\,m^{-1}\,K^{-1}}$
$\hat{\lambda}$	Predicted conductivity	$\mathrm{W\,m^{-1}\,K^{-1}}$
λ_a	Mie potential attractive exponent	–
λ_r	Mie potential repulsive exponent	–
μ	Chemical potential	$\mathrm{J\,mol^{-1}}$
ρ	Molar density or particle density	$\mathrm{mol\,m^{-3}}$ or $\mathrm{m^{-3}}$
ρ_m	Mass density	$\mathrm{kg\,m^{-3}}$
ρ_P	Pearson correlation coefficient	–
σ	Mie potential parameter	m
σ^{HS}	Hard sphere diameter	m
$\bar{\sigma}_{ij}$	Average distance of closest approach, see Eq. (2.128)	m
$\bar{\sigma}$	Mixture average of $\bar{\sigma}_{ij}$, see Eq. (2.129)	m
τ	Kempers target function, see Eq. (2.146)	$\mathrm{J\,K^{-1}}$
Φ	Perturbation to the velocity distribution function	–
φ	Arbitrary variable	*
χ	Deflection angle, see Figures 2.1 and 2.5	–
$\tilde{\chi}$	Density correction factor	–
ψ	Arbitrary function	*
$\Omega_{ij}^{(\ell)}(r), \Omega_i^{(\ell)}(r)$	Collision integral, see Eq. (2.91) and (2.92)	$\mathrm{m^3\,s^{-1}}$

* Various units

Superscripts

Symbol	Description	Unit
CS	Carnahan-Starling value	–
E	Enskog value	–
HS	Hard sphere	–
ig	Ideal gas state	–
α, β	Bulb indices	–
$*$	Reduced state point	–
∞	Value at infinite dilution	–

Operators

$\mathrm{Cov}[\varphi_1, \varphi_2]$	Covariance of φ_1 and φ_2	$*$
$\mathscr{D}$	Differential operator, see Section 2.3.1	–
$\mathrm{Var}[\varphi]$	Variance of φ	$*$
$\underset{\alpha,\beta}{\Delta}$	Difference between bulbs	$*$
$\underset{ig}{\Delta}$	Difference between real and ideal gas state	$*$
$\underset{HS}{\Delta}$	Difference between real and hard sphere state	$*$
Δ_x^2	Numeric second derivative along x-coordinate	$*$
Δ_y^2	Numeric second derivative along y-coordinate	$*$
Δ_{xy}^2	Numeric second cross derivative	$*$
∇	Spatial gradient	m^{-1}
∇_T	Spatial gradient at constant temperature	m^{-1}

* Various units

Multiply defined symbols

	Context and definition		
Symbol	Thermodynamics	Kinetic gas theory	Numerics
A	Helmholtz energy	-	Interpolating coefficient
I	-	Specific integrals	Numeric integral
N	Number of species	Order of approximation	Number of intervals
R	Gas constant	Distance of closest approach	-
x	Mole fraction	Mole fraction	Cartesian coordinate axis
ϵ	-	Angular coordinate	Small scalar
ρ	Molar density	Particle density	-

Abbreviations

Abbreviation	Definition
AAD	Average absolute deviation
AD	Average deviation
BH	Barker-Henderson
CoV	Centre of volume
CoM	Centre of mass
CS	Carnahan-Starling
EoS	Equation of State
FoR	Frame of Reference
HS	Hard-sphere
LB	Lorenz-Berthelot
MD	Molecular dynamics
NDP	Number of data points
rdf.	Radial distribution function
SAFT	Statistical associating fluid theory
vdf.	Velocity distribution function

Contents

1 Introduction

Thermal diffusion, also known as the Soret effect or Ludwig-Soret effect, is an intriguing phenomenon that has interested researchers for over a hundred years since it was first described by Carl Friedrich Wilhelm Ludwig in the mid 19th century.[1] The phenomenon is that a mixture with an imposed temperature gradient will develop a concentration gradient. This a consequence of the well known result from irreversible thermodynamics, that there are cross-coupling coefficients between fluxes and driving forces.[2] The inverse effect - a heat flux resulting from an imposed gradient in chemical potential is known as the Dufour effect.

Onsager showed that the coefficient matrix that describes coupling of fluxes and forces is symmetrical, introducing the famous Onsager reciprocal relations.[3] These relations imply that the coefficient coupling a thermal gradient to a mass flux is equal to the coefficient that couples a chemical potential gradient to a heat flux. This means that if one is capable of modelling the Soret coefficient, the same model can be used to predict the Dufour effect.

As modern science progresses, engineering applications also require ever increasing modelling capabilities. Nano-scale precision is commonly used in the production and development of modern technology, both in the texturing of surfaces and structuring of pores in nano-porous materials.[4] At this scale small variations in concentration and temperature lead to enormous gradients. In the design of battery electrodes and electrolytes, transport properties are of major importance, and during operation a temperature gradient arises in the battery due to the electrode reactions and internal resistance.[5] Further development in these fields therefore warrants precise descriptions of the coupling of heat and mass transfer.

Modern material applications on the macro scale require materials that can perform reliably when subjected to temperature gradients.[2] This includes the materials used in reactors, both chemical and nuclear, as well as materials in pipes and containers containing fluids far from ambient temperature, and the coatings used on said materials. The effects of thermal diffusion on these materials can be relevant even with small temperature gradients, and can become highly significant in environments with large temperature gradients. To further progress the development of materials subjected to extreme conditions, increased precision in the modelling and prediction of diffusive behaviour is required. Among prominent examples of conditions in which thermal diffusion is of significant importance is in the storage of nuclear waste.[6] Temperature gradients resulting from the activity of the partially active waste can lead to migration of radioactive materials and thereby contamination of the environment.

In the field of Biochemical engineering, precise control of heat- and oxygen flow is required.[7] This is also a major hurdle in the up-scaling of bio-reactors. Specifically, the transfer of oxygen into the reactor solution at a rate high enough to keep a high concentration of microorganisms alive is challenging. More precise modelling of how the thermal gradients in the reactor and the mass transfer of oxygen interact may be of use in overcoming this challenge.

In short, the list of possible future applications of a reliable model for thermal diffusion

is long.[8] The current lack of such a model therefore warrants further study into the fundamentals of developing a model for the Soret effect.

1.1 Modelling the Soret effect

A variety of different models have been proposed to quantitatively predict the Soret effect. Already in the early 20th century Chapman and Enskog developed solutions to the Boltzmann equations that provided results in agreement with experiment for dilute gases.[9] These solutions are central to this work, and will be referred to as the Enskog solutions. The theory was later extended to the denser gas region, however extending the theory to the liquid phase has been shown to introduce significant difficulties.[10]

The most common method of employing the Enskog solutions is by evaluating the solutions for mixtures of hard spheres. Approximating a real gas as a hard sphere system greatly simplifies the evaluation of the solutions, and allows one to use tabulated values for a range of otherwise complicated computations.[9,11] Additionally, one can find in the literature a variety of correlations that intend to correct the tabulated hard sphere values such that they can be used with higher accuracy for real systems.[12] In fact, in the making of this work, no attempts at explicitly employing a more advanced potential to the Enskog solutions was found.

It has been suggested that in order to develop a model capable of reproducing the Soret effect in both the gas and liquid phase, one can split the Soret effect in to several contributions. One manner of accomplishing this is splitting the Soret coefficient into an isotopic contribution, S_T^{iso}, depending only on molecular masses and moments of inertia, and a chemical contribution, S_T^{ch}, depending on molecular interactions.[13] The Soret coefficient is then $S_T = S_T^{iso} + S_T^{ch}$, Debuschewitz and Köhler have shown that this manner of splitting the coefficient is likely reasonable. Others have proposed subdividing the Soret coefficient into a reversible and an irreversible contribution,[14] or a kinetic and a configurational contribution.[15].

Through the years, a series of different approaches to modelling thermal diffusion in dense fluids have been proposed. The different approaches primarily have their roots in kinetic theory, irreversible thermodynamics or statistical thermodynamics.[1] Among the more prominent examples are the kinetic based model by Artola et al.[16] the Shukla and Firoozabadi model based on relating the Soret coefficient to the heats of transport,[17,18] and the Kempers model, based in maximisation of the number of microstates in a system.[15,19] There are other models than those presented here, the models by Artola et al., Kempers, and Firoozabadi and Shukla are used here to exemplify the general frameworks within which most models are developed. Different models developed within the same framework tend to be similar in form, and exhibit similar challenges and advantages.[1]

The kinetic, or transition theory approach is based in the works by Prigogine and Tichacek.[20,21] This approach seeks to describe thermal diffusion as an activated process, and to predict the Soret coefficient from the activation free enthalpies of the components in a mixture. The immediate difficulty within this approach is obtaining these activation energies, with the result that they have been used by some as fitting parameters in the interpretation of experimental data.[22] Additionally, the original models within this approach fail to

account for the effects of the different molecular masses of the diffusing species, i.e. they fail to capture the isotopic contribution.[23] Artola et al. propose a new derivation within the transition theory framework that incorporates the isotope effect, and obtain the activation energies from MD simulations.[16] They demonstrate that their model is in good quantitative agreement with simulation results for some simple fluids, and also in somewhat qualitative agreement with measurements in the ethanol-water system. The issue still remains, however, of obtaining the relevant activation energies for a given mixture without requiring time-consuming simulations, and they propose that the reason for the poor quantitative agreement with data in the ethanol-water system is due to a failure of the potential model they use to obtain said energies.

Approaching the task of modelling the the Soret effect by use of the heats of transport originated with the model by Denbigh.[1,24] Much work and improvement within this framework has been made since, resulting in the model proposed by Shukla and Firoozabadi.[17,18] The challenge of applying this model in practice is similar to the challenges of transition theory based models. Accurate values for the heats of transport are not necessarily trivial to obtain. Additionally the model contains a parameter that is commonly treated as a fitting parameter, thereby somewhat reducing its predictive value. Despite these challenges, it has been shown that the model can be capable of accurately reproducing simulation- and experimental results in dense fluids.[23]

The statistical thermodynamic approach, here represented by the models proposed by Kempers,[15,19] has its appeal in the lack of dubiously defined or hard-to-obtain parameters. The underlying hypothesis of these models is that the steady state of a system is characterised by a constrained maximum in the canonical partition function, such that by minimising the Helmholtz energy of a system under certain constraints one can relate the Soret coefficient to thermodynamic properties that may be obtained from an equation of state (EoS). The original Kempers model has the issue of being dependent on accurate values for the enthalpy of the reference state, but later Kempers proposed a modification to the model that removes this inconsistency. Using kinetic gas theory to acquire the value of the Soret coefficient in the ideal gas state, the dependency on the reference state is removed. The derivation of this model is covered in more detail in Section 2.4.

It has been shown that the Kempers model is incapable of reliably predicting the Soret coefficient of binary mixtures.[23,25,26] Kempers claims that the model is highly sensitive to the EoS employed, and this has been confirmed in recent work.[25] An investigation was made into the possibility of predicting whether the model would be capable of predicting the Soret coefficient when coupled with a specific EoS, based on how the given EoS performed in predictions of other thermodynamic quantities. No clear method of achieving this was found, and questions were raised regarding the fundamentals of the statistical thermodynamic approach used by Kempers. Additionally, the question of whether the use of kinetic gas theory should in fact be coupled with an ideal gas reference state was raised.

1.2 Scope

In this work, both the Enskog solutions and the Kempers model are investigated in greater detail. As mentioned in the previous section, the Enskog solutions have been shown to give

agreement with experiments in the low density region, but no attempts at explicitly solving the necessary equations for more advanced potentials than the hard sphere potential have been found in the litterature.

Successfully employing the Enskog solutions with a realistic intermolecular potential could provide the possibility of reliably predicting diffusion coefficients, conductivities, thermal diffusion coefficients and viscosity in the gas phase. This approach is explored using a Mie potential to model intermolecular interactions, with potential parameters obtained from the literature. The potential parameters are deliberately not used as fitting parameters, as part of the goal is to assess feasibility of using parameters from the literature that have been fit to equilibrium properties, rather than transport properties, in order to accurately predict transport properties from the Enskog solutions.

With regard to the Kempers model, the implemented Enskog solutions are used to investigate the assumptions behind the model. In particular the usage of Kinetic gas theory, and the assumption of the steady state as a constrained minimum in Helmholtz energy. The goal of this part is to uncover whether this line of approach is feasible but requiring improvement, or whether future work should be centred around other principles.

2 Theory

In this section, the theory integral to this work are presented. The section begins with more general considerations regarding the relevant flux-force relations and equations of state. Later, important, established results from kinetic gas theory are introduced and some derivations specific to this work are presented. Finally, the derivation and theoretical basis of the Kempers model is presented.

2.1 Flux relations

In this section, relationships between various common transport coefficients and the phenomenological coefficients of a binary mixture subjected to a thermal gradient are presented. Additionally, the relationships between various coefficients used to describe thermal diffusion are given. For a binary system, the independent flux-force relations may be written as

$$\begin{aligned} \mathbf{J}_q &= L_{qq}\nabla\left(\frac{1}{T}\right) + L_{q\mu}\left(-\frac{1}{T}\nabla_T\mu_1\right) \\ \mathbf{J}_1 &= L_{\mu q}\nabla\left(\frac{1}{T}\right) + L_{\mu\mu}\left(-\frac{1}{T}\nabla_T\mu_1\right) \end{aligned} \tag{2.1}$$

where $\mathbf{J}_q$ is the measurable heat flux, and $\mathbf{J}_1$ is the molar flux of species 1 in the centre-of-volume (CoV) frame of reference (FoR), T is the absolute temperature, μ_1 is the chemical potential of specie 1, and L_{ij} are the phenomenological coefficients. ∇_T indicates that the gradient is taken at constant temperature. It is assumed that all transport coefficients are independent of the fluxes and gradients, depending only on the state point of the system i.e. linear response.

First the gradient in chemical potential is related to the mole fraction gradient. Expressing the chemical potential as $\mu_1 = \mu_1(T, p, \mathbf{x})$,

$$\begin{aligned} \nabla\mu_1 &= \left(\frac{\partial\mu_1}{\partial T}\right)_{p,\mathbf{x}}\nabla T + \left(\frac{\partial\mu_1}{\partial p}\right)_{T,\mathbf{x}}\nabla p + \sum_i\left(\frac{\partial\mu_1}{\partial x_i}\right)_{T,p}\nabla x_i \\ (\nabla_T\mu_1)_{\nabla p=0} &= \left[\left(\frac{\partial\mu_1}{\partial x_1}\right)_{T,p} - \left(\frac{\partial\mu_1}{\partial x_2}\right)_{T,p}\right]\nabla x_1 \\ &\equiv \left(\frac{\mathrm{d}\mu_1}{\mathrm{d}x_1}\right)_{T,p}\nabla x_1 \end{aligned} \tag{2.2}$$

where x_i is the mole fraction of specie i and p is the pressure. The final equality defines the quantity $\left(\frac{\mathrm{d}\mu_1}{\mathrm{d}x_1}\right)_{T,p}$.

Now the phenomenological coefficients can be related to the Soret coefficient ($S_{T,1}$), the interdiffusion coefficient (D_{12}) and the conductivity (λ). In the absence of a temperature gradient $L_{\mu\mu}$ can be related to the diffusion coefficient as

$$
\begin{aligned}
(\mathbf{J}_1)_{\nabla T=0} &= -\frac{L_{\mu\mu}}{T}\nabla_T\mu_1 = -\frac{D_{12}}{x_1x_2}\nabla x_1 \\
\frac{L_{\mu\mu}}{T}\left(\frac{\mathrm{d}\mu_1}{\mathrm{d}x_1}\right)_{T,p}\nabla x_1 &= \frac{D_{12}}{x_1x_2}\nabla x_1 \\
D_{12} &= \frac{1}{T}x_1x_2L_{\mu\mu}\left(\frac{\mathrm{d}\mu_1}{\mathrm{d}x_1}\right)_{T,p}.
\end{aligned}
\tag{2.3}
$$

Further, in the state of no mass flux,

$$
\begin{aligned}
L_{\mu q}\nabla\left(\frac{1}{T}\right) + L_{\mu\mu}\left(-\frac{1}{T}\nabla_T\mu_1\right) &= 0 \\
-\frac{L_{\mu q}}{T^2}\nabla T &= \frac{L_{\mu\mu}}{T}\left(\frac{\mathrm{d}\mu_1}{\mathrm{d}x_1}\right)_{T,p}\nabla x_1 \\
L_{\mu q} &= -TL_{\mu\mu}\left(\frac{\mathrm{d}\mu_1}{\mathrm{d}x_1}\right)_{T,p}\frac{\nabla x_1}{\nabla T} \\
L_{\mu q} &= TL_{\mu\mu}\left(\frac{\mathrm{d}\mu_1}{\mathrm{d}x_1}\right)_{T,p}x_1x_2S_{T,1} \\
S_{T,1} &= \frac{L_{\mu q}}{TL_{\mu\mu}\left(\frac{\mathrm{d}\mu_1}{\mathrm{d}x_1}\right)_{T,p}x_1x_2}.
\end{aligned}
\tag{2.4}
$$

Where the Soret coefficient is defined as

$$
S_{T,i} \equiv -\left(\frac{\nabla x_i}{x_i(1-x_i)\nabla T}\right)_{\mathbf{J}_1=0},
\tag{2.5}
$$

with $1 - x_1 = x_2$ for a binary system. The conductivity, λ, is related to the phenomenological coefficients by observing the heat flux in the absence of a mass flux,

$$
\left(\mathbf{J}_q\right)_{\mathbf{J}_1=0} = L_{qq}\nabla\left(\frac{1}{T}\right) + L_{q\mu}\left(-\frac{1}{T}\nabla_T\mu_1\right) = -\lambda\nabla T
\tag{2.6}
$$

When $\mathbf{J}_1 = 0$, the chemical potential gradient can be related to the temperature gradient as

$$
\begin{aligned}
\mathbf{J}_1 = L_{\mu q}\nabla\left(\frac{1}{T}\right) + L_{\mu\mu}\left(-\frac{1}{T}\nabla_T\mu_1\right) &= 0 \\
\left(-\frac{1}{T}\nabla_T\mu_1\right) &= \frac{L_{\mu q}}{L_{\mu\mu}T^2}\nabla T
\end{aligned}
\tag{2.7}
$$

Inserting this into Equation (2.6) yields

$$
\begin{aligned}
-\frac{L_{qq}}{T^2}\nabla T + \frac{L_{q\mu}^2}{L_{\mu\mu}T^2}\nabla T &= -\lambda\nabla T \\
\lambda &= \frac{L_{qq}}{T^2} - \frac{L_{\mu q}^2}{T^2L_{\mu\mu}^2}.
\end{aligned}
\tag{2.8}
$$

There are several common ways of quantifying thermal diffusion, one is through the Soret coefficient. Alternatively, one may use the thermal diffusion coefficient D_T, considering the mass flux in the absence of a compositional or pressure gradient,

$$\begin{aligned}(\mathbf{J}_1)_{\nabla x_1=\nabla p=0} &\equiv -\frac{D_T}{x_1 x_2}\nabla \ln T \\ &= L_{\mu q}\nabla\left(\frac{1}{T}\right) \\ &\implies D_T = \frac{x_1 x_2 L_{\mu q}}{T}.\end{aligned} \tag{2.9}$$

The thermal diffusion ratio, $k_T \equiv \frac{D_T}{D_{12}}$ is also in common use, related to the phenomenological coefficients as

$$k_T \equiv \frac{D_T}{D_{12}} = \frac{L_{\mu q}}{L_{\mu\mu}\left(\frac{\mathrm{d}\mu_1}{\mathrm{d}x_1}\right)_{T,p}} = T x_1 x_2 S_{T,1}. \tag{2.10}$$

Finally, the dimensionless thermal diffusion factor α_T is commonly used, defined as

$$\alpha_{T,i} \equiv \left(\frac{T\nabla x_1}{x_1(1-x_1)\nabla T}\right)_{\mathbf{J}_1=0} = T S_{T,1}. \tag{2.11}$$

2.2 Equations of state

An equation of state (EoS) is an equation that relates various thermodynamic state variables.[12] Often, these are expressed on the form $p = p(n, V, T; \varphi_1, \varphi_2, ...\varphi_n)$ where p, V, n, T are the pressure, mole number, volume and temperature and the φ_i are parameters determined either empirically, from first principles or a combination of the two. Common manners of expressing an EoS are by the use of the compressibility factor $Z \equiv \frac{pV}{nRT}$, or by expressing pressure as a polynomial in $\frac{1}{v}$, where v denotes the molar volume, known as a virial expansion.

An EoS worth mentioning is the Carnahan-Starling (CS) EoS for hard spheres.[27] This equation is based on approximating the virial expansion in volume as an infinite geometric series. Manipulation of this series yields an explicit expression for the compressibility factor for hard spheres as a function of the packing fraction, η, given as

$$\eta = \frac{\pi N_A n \left(\sigma^{HS}\right)^3}{6V} \tag{2.12}$$

where σ^{HS} is the hard sphere diameter and N_A is Avogadros number. Once an expression for the compressibility factor is known, other properties of interest may be related by various derivatives of this. This EoS has been proven to be highly accurate when measured against MD-simulations of hard-sphere particles.[27] Nevertheless, several propositions of extensions and modifications have been made to the theory from its introduction until today, in attempts to further improve its performance.[28,29] An important area of usage for the CS EoS is the ability to accurately represent a theoretical hard sphere state, which can be a convenient reference state.

A frequent starting point in the development of an EoS is describing the Helmholtz energy (A) of the system, this can be done by regarding the intermolecular potential. Observable properties, and other properties of interest, such as the entropy, chemical potential and so on can be calculated in terms of the derivatives of the Helmholtz energy. This approach opens several doors: The possibility to estimate molecular parameters from macroscopic observations;[30] firm control of the microscopic description of the system; the option to explicitly include quantum effects,[31] and the possibility of creating equations of state for theoretical fluids, such as the Lennard-Jones fluid. Apart from accurately describing real fluids, this means that one can construct an EoS that, in principle, should reproduce the results of molecular dynamics (MD) simulations. This can be useful in the development of thermodynamic models.

Many equations of state have been developed using the approach outlined above. Of particular interest in the context of this work is the SAFT-VR Mie EoS. This EoS aims to describe a fluid molecule as a chain of monomers interacting through a Mie-potential, given as

$$u_{ij}^{Mie} = C\varepsilon_{ij}\left[\left(\frac{\sigma_{ij}}{r_{ij}}\right)^{\lambda_{r,ij}} - \left(\frac{\sigma_{ij}}{r_{ij}}\right)^{\lambda_{a,ij}}\right], \quad C = \frac{\lambda_{r_{ij}}}{\lambda_{r,ij}-\lambda_{a,ij}}\left(\frac{\lambda_{r,ij}}{\lambda_{a,ij}}\right)^{\frac{\lambda_{a,ij}}{\lambda_{r,ij}-\lambda_{a,ij}}}, \quad (2.13)$$

where r_{ij} is the inter-particle distance, ε_{ij} is the potential well depth, σ_{ij} is the point at which $u_{ij}^{Mie} = 0$, related to the particle sizes, and $\lambda_{r,ij}$ and $\lambda_{a,ij}$ are adjustable exponents. Further, the Helmholtz energy of the fluid is related to the radial distribution function (rdf.) of these monomers. Using the framework of Barker-Henderson (BH) perturbation theory it can then be shown that the residual Helmholtz energy of the fluid may be written as the sum of a hard sphere term, which may be determined by the CS EoS,[27] and a series of perturbation terms. This EoS has been shown to give highly accurate predictions of fluid-phase equilibria, pressure-volume-temperature (PVT) behaviour and second-derivative properties for both pure fluids and mixtures.

When applying an EoS to a mixture, composition must be taken into account. This is accomplished by the use of mixing rules.[12] A mixing rule is an equation that in some way combines or averages the parameters of the components in a mixture such that an EoS can be applied. These equations are to a large degree empirical in nature, and are often expressed on the form

$$\varphi_m = \sum_i \sum_j x_i x_j \varphi_{ij} \quad (2.14)$$

where φ_m is some property of the mixture, and φ_{ii}, φ_{jj} are the properties of the pure components. Various combining rules can be chosen to determine the interaction terms φ_{ij}. An example of such combining rules are the Lorentz-Berthelot (LB) rules for combining the parameters of a Mie-potential

$$\sigma_{ij} = \frac{1}{2}\left(\sigma_{ii} + \sigma_{jj}\right), \qquad \varepsilon_{ij} = \sqrt{\varepsilon_{ii}\varepsilon_{jj}}. \quad (2.15)$$

These are of special significance in this work, and may be modified to create the more general mixing rules hereafter termed the modified Lorentz-Berthelot rules,[32,33] given as

$$\sigma_{ij} = \frac{1}{2}\left(\sigma_{ii} + \sigma_{jj}\right), \quad \varepsilon_{ij} = (1 - k_{ij})\frac{\left(\sigma_{ii}\sigma_{jj}\right)^{\frac{3}{2}}}{\sigma_{ij}^3}\sqrt{\varepsilon_{ii}\varepsilon_{jj}}$$
$$\lambda_{r,ij} - 3 = (1 - \ell_{ij})\sqrt{(\lambda_{r,ii} - 3)(\lambda_{r,jj} - 3)} \tag{2.16}$$

where k_{ij} and ℓ_{ij} are parameters that may be adjusted represent the behaviour of fluids for which particle interaction is energetically favourable ($k_{ij} > 0$), stabilising the liquid phase; or fluids for which interaction is less favourable ($k_{ij} < 0$), destabilising the liquid phase and lowering the boiling point.

2.3 Kinetic gas theory

The kinetic theory of gases was initiated with the development of the Maxwell-Boltzmann equations in the mid- to late 19th century.[9] The equations are based in statistical mechanics, and consider the effects of collisions between particles. The solutions to these equations, developed by Chapman and Enskog in the early 20th century, are termed the Chapman-Enskog or Enskog solutions, and the resulting theory is often referred to as Enskog theory. This theory has later been expanded and elaborated upon by Chapman and Cowling, among many others.[34,35] For the remainder of this work, the term *Kinetic gas theory* will be used to refer to the theory as a whole, while the term *Enskog solutions* will refer to the specific equations for the transport coefficients that are presented here.

The theory is highly mathematical in nature and at times difficult to follow. Nevertheless the goal of this section is to present a pedagogical summary of the derivations and results integral to this work. For a complete, rigorous explanation of the theory, the reader is referred to the text by Chapman and Cowling.[9] It is worth mentioning that despite being a compressed summary, this section is characterised by a large volume of notation and definitions. This is due to the theory itself being characterised by multiply nested definitions, and notation that requires explaining. Note also that the notation employed here differs somewhat from that of Chapman and Cowling so as to remain self-consistent within the current work.

This section consists of two main parts, first a general introduction to kinetic gas theory will be given, then some derivations specific to this work are presented. The first part will introduce the nomenclature and mathematical basis behind the Enskog solutions, without regard to the intermolecular potential. In the second part the equations necessary to evaluate the solutions for a Mie potential are derived.

The goal of this section is to arrive at a set of explicit equations that can be solved for the interdiffusion- and thermal diffusion coefficients, such that a value for the Soret coefficient in the ideal gas state, S_T^{ig}, may be supplied to the Kempers-model, described in Section 2.4. This will require a rigorous definition of how these coefficients relate to the average velocities of particles in a mixture. It may be fruitful to have the final result in mind when reading, to have this as a reference point as new variables and functions are introduced.

By the end of this section the integrals

$$\begin{aligned} D_{12} \equiv & \frac{\rho_1\rho_2}{3\rho}\{\mathbf{D},\mathbf{D}\} \\ = & \frac{\rho_1\rho_2}{3\rho^3}\int \mathbf{D}_1 \iiint f_1^{(0)} f_{1'}^{(0)} (\mathbf{D}_1 + \mathbf{D}_{1'} - \mathbf{D}_1' - \mathbf{D}_{1'}') b\mathrm{d}b\mathrm{d}\epsilon\mathrm{d}\mathbf{u}_{1'}\mathrm{d}\mathbf{u}_1 \\ & + \frac{\rho_1\rho_2}{6\rho^3}\iiiint f_1^{(0)} f_2^{(0)} (\mathbf{D}_1 + \mathbf{D}_2 - \mathbf{D}_1' - \mathbf{D}_2')^2 b\mathrm{d}b\mathrm{d}\epsilon\mathrm{d}\mathbf{u}_1\mathrm{d}\mathbf{u}_2 \\ & + \frac{\rho_1\rho_2}{3\rho^3}\int \mathbf{D}_2 \iiint f_2^{(0)} f_{2'}^{(0)} (\mathbf{D}_2 + \mathbf{D}_{2'} - \mathbf{D}_2' - \mathbf{D}_{2'}') b\mathrm{d}b\mathrm{d}\epsilon\mathrm{d}\mathbf{u}_{2'}\mathrm{d}\mathbf{u}_2 \end{aligned} \tag{2.17}$$

$$\begin{aligned} D_T \equiv & \frac{\rho_1\rho_2}{3\rho}\{\mathbf{D},\mathbf{\Lambda}\} \\ = & \frac{\rho_1\rho_2}{3\rho^3}\int \mathbf{\Lambda}_1 \iiint f_1^{(0)} f_{1'}^{(0)} (\mathbf{D}_1 + \mathbf{D}_{1'} - \mathbf{D}_1' - \mathbf{D}_{1'}') b\mathrm{d}b\mathrm{d}\epsilon\mathrm{d}\mathbf{u}_{1'}\mathrm{d}\mathbf{u}_1 \\ & + \frac{\rho_1\rho_2}{6\rho^3}\iiiint f_1^{(0)} f_2^{(0)} (\mathbf{D}_1 + \mathbf{D}_2 - \mathbf{D}_1' - \mathbf{D}_2')(\mathbf{\Lambda}_1 + \mathbf{\Lambda}_2 - \mathbf{\Lambda}_1' - \mathbf{\Lambda}_2') b\mathrm{d}b\mathrm{d}\epsilon\mathrm{d}\mathbf{u}_1\mathrm{d}\mathbf{u}_2 \\ & + \frac{\rho_1\rho_2}{3\rho^3}\int \mathbf{\Lambda}_2 \iiint f_2^{(0)} f_{2'}^{(0)} (\mathbf{D}_2 + \mathbf{D}_{2'} - \mathbf{D}_2' - \mathbf{D}_{2'}') b\mathrm{d}b\mathrm{d}\epsilon\mathrm{d}\mathbf{u}_{2'}\mathrm{d}\mathbf{u}_2 \end{aligned} \tag{2.18}$$

will be defined, and a method for approximating their value will be introduced.

2.3.1 The Boltzmann-equations

To begin, the Maxwell-Boltzmann equations are derived by assuming that collisions - i.e. interactions between particles, take up only a very small amount of a particles lifetime. This gives rise to a differential equation for the velocity distribution function (vdf.) $f_i = f_i(\mathbf{u}_i, \mathbf{r}, t)$, describing the probability of finding a particle of species i with velocity $\mathbf{u}_i$ at position $\mathbf{r}$ at time t. This equation reads

$$\frac{\partial f_i}{\partial t} + \mathbf{u}_i \nabla f_i + \mathbf{F_i}\frac{\partial f_i}{\partial \mathbf{u}_i} = \frac{\partial_e f_i}{\partial t} \tag{2.19}$$

where $\mathbf{F}$ denotes an external force on the particle and $\frac{\partial_e f}{\partial t}$ describes the rate of change due to encounters between molecules. The latter of these may be expanded as a sum over the change due to encounters of different types, that is

$$\frac{\partial_e f_i}{\partial t} = \sum_j \left(\frac{\partial_e f_i}{\partial t}\right)_j \tag{2.20}$$

where subscript j denotes the particle type that particle i encounters, and the sum runs over all particle species. To describe this differential, a description of the dynamics of a binary encounter between particles is required. This description is done through a set of geometric considerations that are difficult to summarise in a short manner, these considerations are treated in detail in Section 2.3.9. For the time being, only a summary of the variables involved, their significance and their dependencies are included here, shown

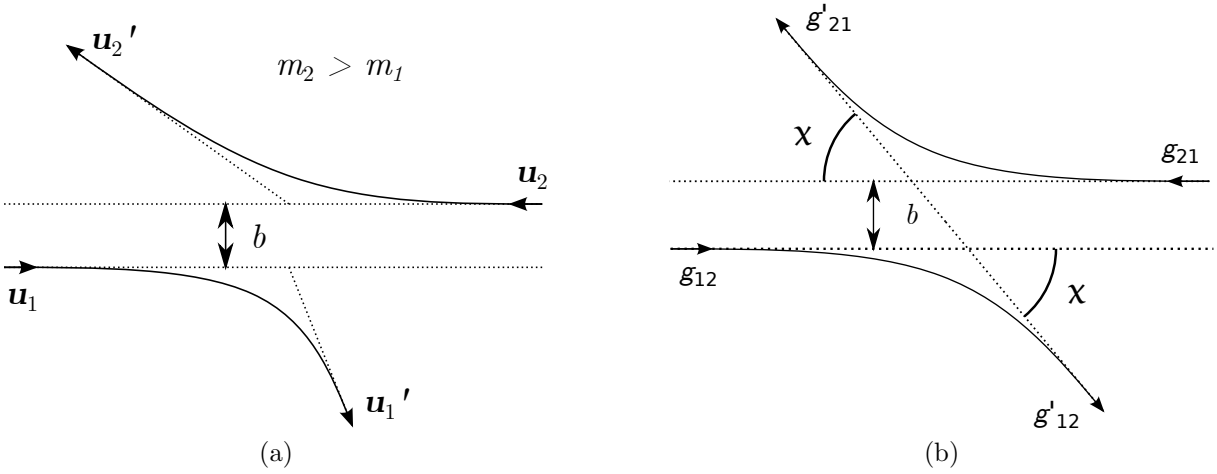

Figure 2.1: The geometry of a binary encounter.

graphically in Figure 2.1. Let $\mathbf{g}_{12}$ and $\mathbf{g}_{21}$ denote the initial velocity of particle 1 relative to 2, and 2 relative to 1. Such that $\mathbf{g}_{12} = \mathbf{u}_1 - \mathbf{u}_2 = -\mathbf{g}_{21}$. Primes on the velocities will denote the post-collision velocities, $\mathbf{g}'_{12} = \mathbf{u}'_1 - \mathbf{u}'_2 = -\mathbf{g}'_{21}$. The relative speeds are then $g_{12} = |\mathbf{g_{12}}| = |\mathbf{g_{21}}| \equiv g$, where the subscript is dropped due to the equivalency. Due to conservation of energy and momentum, the encounter can be completely described by the change in direction of the relative velocities, as the centre of mass velocity is constant. Further, assume that the forces acting between the particles act along the line connecting their centres of mass. For spherical particles this is clearly correct, but for chain-like molecules it cannot be expected to hold.

Now, let χ denote the deflection angle of the relative velocity, that is $\cos\chi = \mathbf{g}_{12} \cdot \mathbf{g}'_{12}$. To describe χ, one must also define the impact parameter b. This can be thought of as the "closest passing distance" the particles would have had if they had been non-interacting point particles, as visualised in Figure 2.1. It is clear that χ is a function of b, and that the functional form is dependent on the intermolecular potential. For a hard-sphere potential, an analytical expression can be derived without extended effort. For other potentials however, the dependency on $\mathbf{g}_{12}$ and the molecular masses requires one to employ numerical methods. For now, χ will be left as some function of $\mathbf{g}_{12}$, b, m_1 and m_2.

Finally, to expand the geometry of Figure 2.1 to three dimensions, define a cylindrical coordinate system centred on particle 1, with the vertical axis perpendicular to $\mathbf{g}_{12}$, such that b takes the role of the radial coordinate. Denote the angular coordinate of this system as ϵ. This coordinate system is shown in Figure 2.2. Following these geometric considerations it can be shown that

$$\left(\frac{\partial_e f_i}{\partial t}\right)_j = \iiint \left(f'_i f'_j - f_i f_j\right) b \mathrm{d}b \mathrm{d}\epsilon \mathrm{d}\mathbf{u}_j. \tag{2.21}$$

The truncation of an interaction potential at some distance now amounts to limiting the integral over $\mathrm{d}b$ to that distance. The case of $i = j$ follows the exact same row of arguments as the case $i \neq j$, but the notation employed can quickly lead to confusion. The

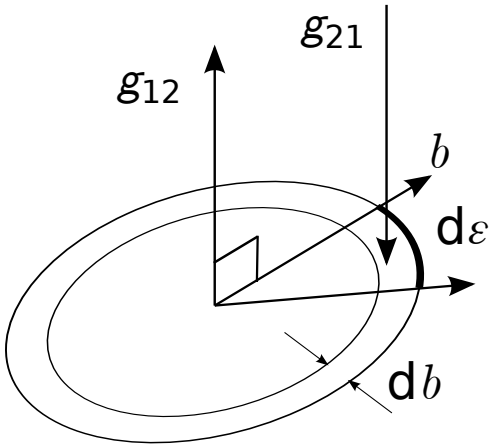

Figure 2.2: Cylindrical coordinate system to describe an encounter.

integral in Equation (2.21) passes over $\mathbf{u}_j$, and is therefore a function only of $\mathbf{u}_i$. If $i = j$, recognise that the integral still only passes over the velocity of one particle in the colliding pair, such that it is still a function of the velocity of the other particle. Notation-wise, Chapman and Cowling solve this by denoting the velocity of the two particles as $\mathbf{u}$ and $\mathbf{u}_i$ and writing

$$\left(\frac{\partial_e f_i}{\partial t}\right)_i = \iiint \left(f_i' f' - f_i f\right) b \mathrm{d}b \mathrm{d}\epsilon \mathrm{d}\mathbf{u}. \tag{2.22}$$

To avoid confusion as to what function f at any time refers to, the notation employed here will denote the velocity of the two particles as $\mathbf{u}_{i'}$ and $\mathbf{u}_i$, such that

$$\left(\frac{\partial_e f_i}{\partial t}\right)_i = \iiint \left(f_i' f_{i'}' - f_i f_{i'}\right) b \mathrm{d}b \mathrm{d}\epsilon \mathrm{d}\mathbf{u}_{i'}. \tag{2.23}$$

For brevity, the integral in equation (2.21) will later be written as

$$-\left(\frac{\partial_e f_i}{\partial t}\right)_j \equiv \begin{cases} J_{ij}(f_i f_j) & i \neq j \\ J_i(f_{i'} f_i) & i = j \end{cases} \tag{2.24}$$

where the prime in $J_i(f_{i'} f_i)$ indicates the variable of integration, the differentiation will become important later. The left hand side of equation (2.19) will be written as $\mathscr{D}_i f_i$, thus the Boltzmann equation for a single-component (simple) gas reads

$$\mathscr{D}_i f_i + J_i(f_{i'} f_i) = 0 \tag{2.25}$$

Already now, the reader should be made aware of one of the inherent limitations of kinetic gas theory: The assumption of uncorrelated collisions. Notice that J_i is only a function of a particles current velocity, thus implying that the rate of change to a particles vdf. due to collisions is independent of its previous velocity. This holds well for gases in which there is little long time-correlation in a particles position, but breaks down at liquid-like densities, where the collision of one particle with another can lead to a long chain of correlated collisions in what are known as cage- and vortex effects.[36]

2.3.2 The first approximation for a simple gas

Now that the notation and formulation of the Boltzmann-equations has been established, the time is ripe for introducing the Enskog solution method. Assume that the true solution, f, of equation (2.19) can be written as an infinite series $f = \sum_{r=0}^{\infty} f^{(r)}$. The operators $\mathscr{D}$ and J can also be subdivided. First, introduce the operator $\frac{\partial_r}{\partial t}$, with the property

$$\frac{\partial \varphi}{\partial t} \equiv \sum_r \frac{\partial_r \varphi}{\partial t}, \quad \varphi = \{\rho, T, \mathbf{u}^n\} \tag{2.26}$$

where $\mathbf{u}^n$ denotes the mole average velocity of the gas, and ρ denotes the number density of the gas. For the formal definition of $\frac{\partial_r}{\partial t}$ the reader is referred to Chapman and Cowling, pp. 116.[9] Enskog now subdivides the operator $\mathscr{D}$ such that

$$\begin{aligned} \mathscr{D}_1 f_1 &= \sum_r \mathscr{D}^{(r)}, \quad \mathscr{D}^{(0)} = 0 \\ \mathscr{D}_1^{(r)} &= \sum_{i=0}^{r-1} \frac{\partial_r f_1^{(r-1-i)}}{\partial t} + \mathbf{u} \cdot \nabla f_1^{(r-1)} + \mathbf{F}_1 \cdot \nabla f_1^{(r-1)}, \quad r > 0. \end{aligned} \tag{2.27}$$

Similarly, J can be subdivided such that

$$J_1^{(r)} = \sum_{i=0}^{r} J_1(f_{1'}^{(i)} f_1^{(r-i)}). \tag{2.28}$$

It is important to note that this manner of subdividing $\mathscr{D}$ and J is a matter of choice, and that the key to the Enskog solution lies in choosing to subdivide them in this way. The result of the subdivision is that Equation (2.25) may be written as

$$\sum_r \mathscr{D}_1^{(r)} + J_1^{(r)} = 0 \tag{2.29}$$

This equation is fulfilled if $\mathscr{D}_1^{(r)} + J_1^{(r)} = 0, \forall\, r$, and the manner in which $\mathscr{D}$ and J have been subdivided ensures that each of these equations is solvable. The equation corresponding to $r = 0$ becomes $J_1(f_{1'}^{(0)} f_1^{(0)}) = 0$, of which

$$f_1^{(0)} = \exp\left(\varphi^{(1)} + \boldsymbol{\varphi^{(2)}} m\mathbf{u}_1 + \varphi^{(3)} \frac{1}{2} m u_1^2\right) \tag{2.30}$$

is the general solution, with $\varphi^{(1)}, \boldsymbol{\varphi^{(2)}}$ and $\varphi^{(3)}$ arbitrary quantities independent of $\mathbf{u}_1$, and $u_1 = |\mathbf{u}_1|$ is the particle speed. Making some convenient choices for these, yields

$$f_1^{(0)} = \rho \left(\frac{m_1}{2\pi k_B T}\right)^{\frac{3}{2}} \exp\left(-\frac{m_1 U_1^2}{2k_B T}\right), \tag{2.31}$$

where $\mathbf{U}_i \equiv \mathbf{u}_i - \mathbf{u}^n$ is the peculiar velocity of species i, and U is its magnitude, the peculiar speed, with $\mathbf{u}^n$ the mole average velocity. Note that $J_1(f_{1'}^{(0)} f_1^{(0)}) = 0$ is the exact equation describing a gas in which collisions have no net effect on the velocity distribution function, such that $f^{(0)}$ is the velocity distribution function in a homogeneous (uniform) steady state gas. It is evident then, that to describe a non-uniform state, a solution for

the second approximation $f^{(1)}$ must be found. Before moving on, note some properties of the velocity distribution function regarding the *summational invariants*, ρ, $m\mathbf{U}$ and $\frac{1}{2}mU^2$. That is, the number density, momentum and kinetic energy of the gas. These must all be conserved over time. It then follows that

$$\begin{aligned} \int f_1^{(0)} \mathrm{d}\mathbf{u}_1 = \rho_1 = \int f_1 \mathrm{d}\mathbf{u}_1 \\ \int (f_1 - f_1^{(0)}) \mathrm{d}\mathbf{u}_1 = 0 \end{aligned} \tag{2.32}$$

and similarly for the other invariants,

$$\int (f_1 - f_1^{(0)}) \varphi \mathrm{d}\mathbf{u}_1 = 0, \qquad \varphi = \{m\mathbf{U}_1, \frac{1}{2}mU_1^2\}. \tag{2.33}$$

Inserting for $f_1 = \sum_{r=0}^{\infty} f_1^{(r)}$ then yields

$$\sum_{r=1}^{\infty} \int f_1^{(r)} \varphi \mathrm{d}\mathbf{u}_1 = 0, \qquad \varphi = \{1, m\mathbf{U}_1, \frac{1}{2}mU_1^2\}. \tag{2.34}$$

This equation is clearly fulfilled if

$$\int f_1^{(r)} \varphi \mathrm{d}\mathbf{u}_1 = 0 \ \ \forall \ \ i > 0, \qquad \varphi = \{1, m\mathbf{U}_1, \frac{1}{2}mU_1^2\}. \tag{2.35}$$

2.3.3 The second approximation for a simple gas

It can be shown that a valid second approximation to f can be written on the form $f_1^{(1)} = f_1^{(0)} \Phi_1^{(1)}$. Just like the first approximation, the second approximation satisfies Equation (2.29) if

$$\mathscr{D}_1^{(1)} + J_1^{(1)} = 0. \tag{2.36}$$

Here, $\mathscr{D}^{(1)}$ may be expanded as

$$\begin{aligned} \mathscr{D}_1^{(1)} &= f_1^{(0)} \left[\left(\frac{mU_1^2}{2k_BT} - \frac{5}{2} \right) \mathbf{U}_1 \nabla \ln T + \frac{m}{k_BT} \mathbf{U}_1 \overset{\circ}{\mathbf{U}}_1 : \nabla \mathbf{u}^n \right] \\ &= f_1^{(0)} \left[\left(\mathscr{U}_1 - \frac{5}{2} \right) \mathbf{U}_1 \nabla \ln T + \frac{m}{k_BT} \boldsymbol{\mathscr{U}}_1 \overset{\circ}{\boldsymbol{\mathscr{U}}}_1 : \nabla \mathbf{u}^n \right] \end{aligned} \tag{2.37}$$

where for a 3d vector $\mathbf{v}$, $\overset{\circ}{\mathbf{v}}\mathbf{v}$ is the operation

$$\overset{\circ}{\mathbf{v}}\mathbf{v} = \begin{bmatrix} v_1 & & \\ & v_2 & \\ & & v_3 \end{bmatrix} \begin{bmatrix} v_1 & v_2 & v_3 \\ v_1 & v_2 & v_3 \\ v_1 & v_2 & v_3 \end{bmatrix} - \frac{1}{3} v^2 \underline{\boldsymbol{I}} \tag{2.38}$$

and for two matrices $\underline{\boldsymbol{\varphi}}_1 : \underline{\boldsymbol{\varphi}}_2 = \varphi_{1,ij}\varphi_{2,ji} = \sum_i \sum_j \varphi_{1,ij}\varphi_{2,ji}$ denotes the double dot product. $\boldsymbol{\mathscr{U}}_i$ is the dimensionless peculiar velocity $\boldsymbol{\mathscr{U}}_i \equiv \left(\frac{m_i}{2k_BT} \right)^{\frac{1}{2}} \mathbf{U}_i$, and $\mathscr{U} \equiv |\boldsymbol{\mathscr{U}}|$ is the peculiar speed. Further, the term $J^{(1)}$ can be expanded and rewritten as

$$\begin{aligned} J_1^{(1)} &= J_1(f_{1'}^{(0)} f_1^{(1)}) + J_1(f_{1'}^{(1)} f_1^{(0)}) \\ &= \rho^2 I_1 \left(\Phi_1^{(1)} \right) \end{aligned} \tag{2.39}$$

where the integral $I_1\left(\Phi_1^{(1)}\right)$ has been introduced.

This is a convenient time to step aside and introduce some integral notation that will be heavily employed later. Recognise how Equations (2.17) and (2.18) consist of exactly these types of integrals. Let F and G be functions defined on $\mathbf{u}_1$ and K be a function defined on $\mathbf{u}_1$ and $\mathbf{u}_2$. Then, using the notation $F_i = F(\mathbf{u}_i)$, $F_i' = F(\mathbf{u}_i')$, $K_{ij} = K_{ji} = K(\mathbf{u}_i, \mathbf{u}_j)$ and $K_{ij}' = K_{ji}' = K(\mathbf{u}_i', \mathbf{u}_j')$,

$$\begin{aligned}
\rho_1^2 I_1(F) &\equiv \iiint f_1^{(0)} f_{1'}^{(0)} \left(F_1 + F_{1'} - F_1' - F_{1'}'\right) g b \mathrm{d}b \mathrm{d}\epsilon \mathrm{d}\mathbf{u}_{1'} \\
\rho_2^2 I_2(F) &\equiv \iiint f_2^{(0)} f_{2'}^{(0)} \left(F_2 + F_{2'} - F_2' - F_{2'}'\right) g b \mathrm{d}b \mathrm{d}\epsilon \mathrm{d}\mathbf{u}_{2'} \\
\rho_1 \rho_2 I_{12}(K) &\equiv \iiint f_1^{(0)} f_2^{(0)} \left(K_{12} - K_{12}'\right) g b \mathrm{d}b \mathrm{d}\epsilon \mathrm{d}\mathbf{u}_2 \\
\rho_1 \rho_2 I_{21}(K) &\equiv \iiint f_1^{(0)} f_2^{(0)} \left(K_{12} - K_{12}'\right) g b \mathrm{d}b \mathrm{d}\epsilon \mathrm{d}\mathbf{u}_1
\end{aligned} \tag{2.40}$$

Note that $I_1(F)$ and $I_{12}(K)$ are functions of $\mathbf{u}_1$, while $I_2(F)$ and $I_{21}(K)$ are functions of $\mathbf{u}_2$. Further define the bracket integrals

$$[F, G]_i \equiv \int G_i I_i(F) \mathrm{d}\mathbf{u}_i, \qquad i = \{1, 2\}. \tag{2.41}$$

For functions F and H defined on $\mathbf{u}_1$, and G and K defined on $\mathbf{u}_2$, define

$$[F_1 + G_2, H_1 + K_2]_{12} \equiv \int F_1 I_{12}(H_1 + K_2) \mathrm{d}\mathbf{u}_1 + \int G_2 I_{21}(H_1 + K_2) \mathrm{d}\mathbf{u}_2 \tag{2.42}$$

Expanding Equation (2.42), one will find that $[F_1 + G_2, H_1 + K_2]_{12} = [H_1 + K_2, F_1 + G_2]_{12}$. Finally, for functions F and G both defined on $\mathbf{u}_1$ and $\mathbf{u}_2$, define the bracket integral

$$\rho^2 \{F, G\} = \rho_1^2 [F, G]_1 + \rho_1 \rho_2 [F_1 + F_2, G_1 + G_2]_{12} + \rho^2 [F, G]_2. \tag{2.43}$$

Returning to the problem of determining the second approximation $f_1^{(1)} = f_1^{(0)} \Phi_1^{(1)}$, inserting Equations (2.39) and (2.37) into Equation (2.36) yields

$$\rho^2 I_1\left(\Phi_1^{(1)}\right) = -f_1^{(0)} \left[\left(\mathscr{U}_1^2 - \frac{5}{2}\right) \mathbf{U}_1 \nabla \ln T + \frac{m}{k_B T} \boldsymbol{\mathscr{U}}_1 \mathring{\boldsymbol{\mathscr{U}}}_1 : \nabla \mathbf{u}^n\right]. \tag{2.44}$$

Observe that $I_1\left(\Phi_1^{(1)}\right)$ is linear in $\Phi_1^{(1)}$, and that the right hand side of this equation is linear in the components of $\nabla \ln T$ and $\mathbf{u}^n$. Thereby, $\Phi_1^{(1)}$ can be written as a linear combination of the components of $\nabla \ln T$ and $\mathbf{u}^n$ and the solution to the equation $I_1\left(\Phi_1^{(1)}\right) = 0$. The latter can be recognised as a solution of the form in equation (2.30), such that for some vector $\boldsymbol{\Lambda}$, matrix $\underline{\boldsymbol{B}}$, and constants $\varphi^{(1,1)}, \boldsymbol{\varphi}^{(\mathbf{2,1})}, \varphi^{(3,1)}$

$$\Phi_1^{(1)} = -\frac{1}{\rho} \left(\frac{2 k_B T}{m_1}\right)^{\frac{1}{2}} \boldsymbol{\Lambda} \nabla \ln T - \frac{2}{\rho} \underline{\boldsymbol{B}} : \nabla \mathbf{u}^n + \varphi^{(1,1)} + \boldsymbol{\varphi}^{(\mathbf{2,1})} m_1 \mathbf{u}_1 + \varphi^{(3,1)} \frac{1}{2} m_1 U_1^2, \tag{2.45}$$

Where the prefactors to $\mathbf{\Lambda}$ and $\underline{\boldsymbol{B}}$ are chosen for later convenience. Substituting this into equation (2.44), using the fact that $I_1(F+G) = I_1(F) + I_1(G)$, and equating the coefficients to each of the gradient terms yields a set of equations for $\mathbf{\Lambda}$ and $\underline{\boldsymbol{B}}$,

$$\begin{aligned} \rho I_1(\mathbf{\Lambda}) &= f_1^{(0)} \left(\mathscr{U}_1^2 - \frac{5}{2} \right) \mathbf{U}_1 \\ \rho I_1(\underline{\boldsymbol{B}}) &= f_1^{(0)} \boldsymbol{\mathscr{U}}_1 \mathring{\boldsymbol{\mathscr{U}}}_1. \end{aligned} \tag{2.46}$$

It is clear from the first of these equations that $\mathbf{\Lambda}$ must be a vector parallel to $\mathbf{U}_1$, which is parallel to $\boldsymbol{\mathscr{U}}_1$, such that one can write

$$\mathbf{\Lambda} = \Lambda(\mathscr{U}_1, \rho, T) \boldsymbol{\mathscr{U}}_1, \tag{2.47}$$

where $\mathscr{U} \equiv |\boldsymbol{\mathscr{U}}|$ is the dimensionless peculiar speed. It is less clear, but can be shown, that $\underline{\boldsymbol{B}}$ is a symmetric, traceless matrix. All symmetric, traceless matrices that can be formed from $\boldsymbol{\mathscr{U}}_1$ are multiples of $\boldsymbol{\mathscr{U}}_1 \mathring{\boldsymbol{\mathscr{U}}}_1$. Therefore, $\underline{\boldsymbol{B}}$ can be written as

$$\underline{\boldsymbol{B}} = B(\mathscr{U}_1, \rho, T) \boldsymbol{\mathscr{U}}_1 \mathring{\boldsymbol{\mathscr{U}}}_1. \tag{2.48}$$

The constants $\varphi^{(1,1)}, \boldsymbol{\varphi^{(2,1)}}$ and $\varphi^{(3,1)}$ can be chosen such that $f_1^{(1)}$ satisfies the constraints posed by the summational invariants, from Equation (2.35). Analysing these constraints, one finds that $\varphi^{(1,1)} = \boldsymbol{\varphi^{(2,1)}} = \varphi^{(3,1)} = 0$ is a valid choice. Equation (2.45) then reduces to

$$\Phi_1^{(1)} = -\frac{1}{\rho_1} \left(\frac{2 k_B T}{m_1} \right)^{\frac{1}{2}} \mathbf{\Lambda} \nabla \ln T - \frac{2}{\rho} \underline{\boldsymbol{B}} : \nabla \mathbf{u}^n. \tag{2.49}$$

Until now, only a unary gas has been considered. The method for arriving at Equation (2.49) for a binary system follows the exact same steps as those presented so far. Because the goal of this section is to describe diffusion, we now move to a binary case and in short words describe how the equation for $\Phi_1^{(1)}$ will differ from Equation (2.49).

2.3.4 The binary solutions

The Boltzmann equations for a binary system are directly analogous to those of a unary system,

$$\frac{\partial f_i}{\partial t} + \mathbf{u} \nabla f_i + \mathbf{F_i} \frac{\partial f_i}{\partial \mathbf{u}} = \frac{\partial_e f_i}{\partial t}, \qquad i = \{1, 2\}. \tag{2.50}$$

Rewriting this in terms of the operators $\mathscr{D}$ and J gives

$$\begin{aligned} \mathscr{D}_1 f_1 + J_1(f_1 f_{1'}) + J_{12}(f_1 f_2) = 0 \\ \mathscr{D}_2 f_2 + J_2(f_2 f_{2'}) + J_{21}(f_2 f_1) = 0 \end{aligned} \tag{2.51}$$

The subdivision of f_i and $\mathscr{D}_i$ follow the same procedure as the one outlined in the unary case. For J_i, the function $J_i^{(r)}$ takes the form

$$J_i^{(r)} \equiv \sum_{k=0}^{r} J_i(f_i^{(k)} f_{i'}^{(r-k)}) + J_{ij}(f_i^{(k)} f_j^{(r-k)}). \tag{2.52}$$

Again, requiring that $\mathscr{D}_i^{(r)} + J_i^{(r)} = 0 \; \forall \; r$ gives solutions to the first approximation identical to Equation (2.31). In the solution of the second approximation, a difference turns up. Inserting $f_1^{(1)} = f_1^{(0)}\Phi_1^{(1)}$ and $f_2^{(1)} = f_2^{(0)}\Phi_2^{(1)}$ into the expression for $J_1^{(1)}$ yields

$$J_1^{(1)} = \rho_1^2 I_1(\Phi_1^{(1)}) + \rho_1\rho_2 I_{12}(\Phi_1^{(1)} + \Phi_2^{(1)}). \tag{2.53}$$

Expanding $\mathscr{D}_1^{(1)}$ now yields

$$\mathscr{D}_1^{(1)} = f_1^{(0)}\left[\left(\mathscr{U}_1^2 - \frac{5}{2}\right)\mathbf{U}_1\nabla\ln T + \frac{m}{k_B T}\boldsymbol{\mathscr{U}}_1\overset{\circ}{\boldsymbol{\mathscr{U}}}_1 : \nabla\mathbf{u}^n + x_1^{-1}\mathbf{d}_{12}\mathbf{U}_1\right] \tag{2.54}$$

Where the only difference from Equation (2.37) is the appearance of the trailing term

$$\mathbf{d}_{12} \equiv \nabla x_1 + \frac{\rho_1\rho_2(m_2 - m_1)}{\rho\rho_m}\nabla\ln p - \frac{\rho_{m,1}\rho_{m,2}}{\rho_m p}\left(\mathbf{F}_1 - \mathbf{F}_2\right), \tag{2.55}$$

where x_i denotes the mole fraction of species i, and ρ_m denotes the mass density. Just as in the previous section, it is now clear that $\Phi_1^{(1)}$ and $\Phi_2^{(1)}$ must be linear functions of $\nabla\ln T$, $\mathbf{d}_{12}$ and $\nabla\mathbf{u}^n$. Therefore, for some $\boldsymbol{\Lambda}$, $\mathbf{D}$ and $\underline{\boldsymbol{B}}$, the $\Phi_i^{(1)}$ may be written as

$$\Phi_i^{(1)} = -\boldsymbol{\Lambda}_i\nabla\ln T - \mathbf{D}_i\mathbf{d}_{12} - 2\underline{\boldsymbol{B}}_i : \nabla\mathbf{u}^n, \qquad i = \{1,2\} \tag{2.56}$$

Inserting Equations (2.56) and (2.54) for $\Phi_i^{(1)}$ and $\mathscr{D}_i^{(1)}$ into Equations (2.51) and matching the coefficients of the gradients now leads to a set of equations that uniquely determine $\boldsymbol{\Lambda}$, $\mathbf{D}$ and $\underline{\boldsymbol{B}}$, analogous to Equations (2.46),

$$\begin{aligned}
f_1^{(0)}(\boldsymbol{\mathscr{U}}_1^2 - \frac{5}{2})\mathbf{U}_1 &= \rho_1^2 I_1(\boldsymbol{\Lambda}_1) + \rho_1\rho_2 I_{12}(\boldsymbol{\Lambda}_1 + \boldsymbol{\Lambda}_2)\\
f_2^{(0)}(\boldsymbol{\mathscr{U}}_2^2 - \frac{5}{2})\mathbf{U}_2 &= \rho_2^2 I_2(\boldsymbol{\Lambda}_2) + \rho_2\rho_1 I_{21}(\boldsymbol{\Lambda}_2 + \boldsymbol{\Lambda}_1)\\
x_1^{-1}f_1^{(0)}\mathbf{U}_1 &= \rho_1^2 I_1(\mathbf{D}_1) + \rho_1\rho_2 I_{12}(\mathbf{D}_1 + \mathbf{D}_2)\\
-x_2^{-1}f_2^{(0)}\mathbf{U}_2 &= \rho_2^2 I_2(\mathbf{D}_2) + \rho_2\rho_1 I_{21}(\mathbf{D}_2 + \mathbf{D}_1)\\
f_1^{(0)}\boldsymbol{\mathscr{U}}_1\overset{\circ}{\boldsymbol{\mathscr{U}}}_1 &= \rho_1^2 I_1(\underline{\boldsymbol{B}}_1) + \rho_1\rho_2 I_{12}(\underline{\boldsymbol{B}}_1 + \underline{\boldsymbol{B}}_2)\\
f_2^{(0)}\boldsymbol{\mathscr{U}}_2\overset{\circ}{\boldsymbol{\mathscr{U}}}_2 &= \rho_2^2 I_2(\underline{\boldsymbol{B}}_2) + \rho_2\rho_1 I_{21}(\underline{\boldsymbol{B}}_2 + \underline{\boldsymbol{B}}_1)
\end{aligned} \tag{2.57}$$

Thus, to a second approximation, the velocity distribution function is given as

$$\begin{aligned}
f_i &= f_i^{(0)}(1 + \Phi_i^{(1)}), \qquad i = \{1,2\}\\
&= f_i^{(0)}\left[1 - \boldsymbol{\Lambda}_i\nabla\ln T - \mathbf{D}_i\mathbf{d}_{12} - 2\underline{\boldsymbol{B}}_i : \nabla\mathbf{u}^n\right].
\end{aligned} \tag{2.58}$$

Note that $\boldsymbol{\Lambda}$, $\mathbf{D}$ and $\underline{\boldsymbol{B}}$ have been established to be unique, but determining their exact functional form still remains.

2.3.5 Diffusion

Now that an expression for the velocity distribution function has been obtained, the analysis of diffusion can begin. The analysis of conductivity and viscosity is analogous,

only considering the conservation equations for momentum and energy rather than the particle number, these analyses will therefore not be covered in detail here. The two components of a mixture are diffusing relative to each other if $\bar{\mathbf{u}}_1 - \bar{\mathbf{u}}_2 \equiv \bar{\mathbf{U}}_1 - \bar{\mathbf{U}}_2 \neq 0$. Where the bar denotes the mole averaged values of the velocities. From the velocity distribution function, the differences in mean velocity are

$$\bar{\mathbf{U}}_1 - \bar{\mathbf{U}}_2 = \frac{1}{\rho_1}\int f_1 \mathbf{U}_1 \mathrm{d}\mathbf{u}_1 - \frac{1}{\rho_2}\int f_2 \mathbf{U}_2 \mathrm{d}\mathbf{u}_2. \tag{2.59}$$

Inserting the velocity distribution function from Equation (2.58), and noting that $f_i^{(0)}\mathbf{U}$, and $\underline{\boldsymbol{B}}_i : \nabla \mathbf{u}^n \mathbf{U}$ are odd functions such that their integrals vanish yields

$$\begin{aligned}\bar{\mathbf{U}}_1 - \bar{\mathbf{U}}_2 = -\frac{1}{3}\Bigg[&\left(\frac{1}{\rho_1}\int f_1^{(0)}\mathbf{U}_1\mathbf{D}_1\mathrm{d}\mathbf{u}_1 - \frac{1}{\rho_2}\int f_2^{(0)}\mathbf{U}_2\mathbf{D}_2\mathrm{d}\mathbf{u}_2\right)\mathbf{d}_{12} \\ &+ \left(\frac{1}{\rho_1}\int f_1^{(0)}\mathbf{U}_1\boldsymbol{\Lambda}_1\mathrm{d}\mathbf{u}_1 - \frac{1}{\rho_2}\int f_2^{(0)}\mathbf{U}_2\boldsymbol{\Lambda}_2\mathrm{d}\mathbf{u}_2\right)\nabla \ln T\Bigg]\end{aligned} \tag{2.60}$$

Now, from Equations (2.57) it can be shown that for any vector function $\mathbf{a}$ defined on $\mathbf{u}_1$ and $\mathbf{u}_2$,

$$\rho^2\{\mathbf{D},\mathbf{a}\} = x_1^{-1}\int f_1^{(0)}\mathbf{U}_1\mathbf{a}_1\mathrm{d}\mathbf{u}_1 - x_2^{-1}\int f_2^{(0)}\mathbf{U}_2\mathbf{a}_2\mathrm{d}\mathbf{u}_2. \tag{2.61}$$

Since $\boldsymbol{\Lambda}$ and $\mathbf{D}$ are exactly such vector functions, Equation (2.60) may be contracted to

$$\bar{\mathbf{U}}_1 - \bar{\mathbf{U}}_2 = -\frac{1}{3}\rho\left[\{\mathbf{D},\mathbf{D}\}\mathbf{d}_{12} + \{\mathbf{D},\boldsymbol{\Lambda}\}\nabla \ln T\right]. \tag{2.62}$$

Considering the cases in which either $\mathbf{d}_{12} = 0$ or $\nabla T = \mathbf{F}_1 = \mathbf{F}_2 = \nabla p = 0$ allows us to identify the interdiffusion coefficient D_{12} and the thermal diffusion coefficient D_T for a binary mixture. In the first case,

$$\begin{aligned}\bar{\mathbf{u}}_1 - \bar{\mathbf{u}}_2 &= -\frac{\rho^2}{\rho_1\rho_2}D_T\nabla \ln T, \qquad \mathbf{d}_{12} = 0 \\ -\frac{1}{3}\{\mathbf{D},\boldsymbol{\Lambda}\}\nabla \ln T &= -\frac{D_T}{x_1x_2}\nabla \ln T \\ D_T &= \frac{\rho_1\rho_2}{3\rho}\{\mathbf{D},\boldsymbol{\Lambda}\}\end{aligned} \tag{2.63}$$

and in the second,

$$\begin{aligned}\bar{\mathbf{u}}_1 - \bar{\mathbf{u}}_2 &= -\frac{\rho^2}{\rho_1\rho_2}D_{12}\nabla x_1, \qquad \nabla T = \mathbf{F}_1 = \mathbf{F}_2 = \nabla p = 0 \\ -\frac{1}{3}\{\mathbf{D},\mathbf{D}\}\nabla x_1 &= -\frac{D_{12}}{x_1x_2}\nabla x_1 \\ D_{12} &= \frac{\rho_1\rho_2}{3\rho}\{\mathbf{D},\mathbf{D}\}.\end{aligned} \tag{2.64}$$

Additionally, the thermal diffusion ratio may be identified as

$$k_T \equiv \frac{D_T}{D_{12}} = \frac{\{\mathbf{D},\boldsymbol{\Lambda}\}}{\{\mathbf{D},\mathbf{D}\}} \tag{2.65}$$

Conducting the same analysis, but regarding the heat flux

$$\mathbf{J}_q = \int f_1 \frac{1}{2} m_1 U_1^2 \mathbf{U}_1 \mathrm{d}\mathbf{u}_1 + \int f_2 \frac{1}{2} m_2 U_2^2 \mathbf{U}_2 \mathrm{d}\mathbf{u}_2 \tag{2.66}$$

rather than the mass flux, one finds that in the absence of a mass flux

$$\begin{aligned} \mathbf{J}_q &= -\frac{1}{3} k_B \rho^2 \left(\{\mathbf{\Lambda}, \mathbf{\Lambda}\} - \frac{\{\mathbf{\Lambda}, \mathbf{D}\}^2}{\{\mathbf{D}, \mathbf{D}\}} \right) \nabla T \\ \lambda &\equiv \frac{1}{3} k_B \rho^2 \left(\{\mathbf{\Lambda}, \mathbf{\Lambda}\} - \frac{\{\mathbf{\Lambda}, \mathbf{D}\}^2}{\{\mathbf{D}, \mathbf{D}\}} \right), \end{aligned} \tag{2.67}$$

where λ is the conductivity. Further, we may introduce the auxiliary function $\tilde{\mathbf{\Lambda}}_i = \mathbf{\Lambda}_i - k_T \mathbf{D}_i$ such that the conductivity can be written as

$$\lambda = \frac{1}{3} k_B \rho^2 \{\tilde{\mathbf{\Lambda}}, \tilde{\mathbf{\Lambda}}\}. \tag{2.68}$$

To acquire values for the diffusion coefficients and conductivity, it is thereby necessary to evaluate the integrals $\{\mathbf{D}, \mathbf{D}\}$, $\{\mathbf{D}, \mathbf{\Lambda}\}$ and $\{\tilde{\mathbf{\Lambda}}, \tilde{\mathbf{\Lambda}}\}$. To accomplish this, we write the functions $\tilde{\mathbf{\Lambda}}_i$ and $\mathbf{D}_i$ as polynomial expansions using an orthogonal set of polynomials known as the Sonine polynomials, denoted $S_m^{(n)}(\varphi)$. These have the property

$$\int_0^\infty e^{-\varphi} S_m^{(p)}(\varphi) S_m^{(q)}(\varphi) \varphi^m d\varphi = \frac{\Gamma(m+p+1)}{p!} \delta_{pq} \tag{2.69}$$

where Γ denotes the gamma function and δ_{pq} is the Kronecker delta. $\mathbf{D}$ and $\tilde{\mathbf{\Lambda}}$ are expanded as

$$\mathbf{D}_1 = \sum_{p=-\infty}^{\infty} d_p \mathbf{a}_1^{(p)} \qquad \mathbf{D}_2 = \sum_{p=-\infty}^{\infty} d_p \mathbf{a}_2^{(p)} \tag{2.70}$$

$$\tilde{\mathbf{\Lambda}}_1 = \sum_{\substack{p=-\infty \\ p \neq 0}}^{\infty} l_p \mathbf{a}_1^{(p)} \qquad \tilde{\mathbf{\Lambda}}_2 = \sum_{\substack{p=-\infty \\ p \neq 0}}^{\infty} l_p \mathbf{a}_2^{(p)} \tag{2.71}$$

where

$$\mathbf{a}_1^{(p)} \equiv 0 \qquad \mathbf{a}_2^{(p)} \equiv S_{3/2}^{(p)} \left(\mathscr{U}_2^2 \right) \boldsymbol{\mathscr{U}}_2 \qquad p < 0 \tag{2.72}$$

$$\mathbf{a}_1^{(0)} \equiv M_1^{\frac{1}{2}} \rho_{m,2} \rho_m^{-1} \boldsymbol{\mathscr{U}}_1 \qquad \mathbf{a}_2^{(0)} \equiv -M_2^{\frac{1}{2}} \rho_{m,1} \rho_m^{-1} \boldsymbol{\mathscr{U}}_2 \qquad p = 0 \tag{2.73}$$

$$\mathbf{a}_1^{(p)} \equiv S_{3/2}^{(p)} \left(\mathscr{U}_1^2 \right) \boldsymbol{\mathscr{U}}_1 \qquad \mathbf{a}_2^{(p)} \equiv 0 \qquad p > 0 \tag{2.74}$$

Now, recall from Equation (2.61) that for any vector function $\mathbf{a}_i^{(p)}$, we may write

$$\rho^2 \{\mathbf{D}, \mathbf{a}^{(p)}\} = x_1^{-1} \int f_1^{(0)} \mathbf{U}_1 \mathbf{a}_1^{(p)} \mathrm{d}\mathbf{u}_1 - x_2^{-1} \int f_2^{(0)} \mathbf{U}_2 \mathbf{a}_2^{(p)} \mathrm{d}\mathbf{u}_2. \tag{2.75}$$

After inserting for $\mathbf{a}_1^{(p)}$ from Equation (2.72) - (2.74) this integral can be evaluated analytically to give

$$\{\mathbf{D}, \mathbf{a}^{(p)}\} = \delta_p, \qquad \delta_p = \begin{cases} \frac{3}{2\rho}\left(\frac{2k_BT}{m_0}\right)^{\frac{1}{2}}, & p = 0 \\ 0, & p \neq 0, \end{cases} . \tag{2.76}$$

where $m_0 = m_1 + m_2$. Thus, by substituting the expansion of $\mathbf{D}$ from Equation (2.71) into Equation (2.76), and utilising the orthogonality properties of the Sonine polynomials,

$$\sum_{p=-\infty}^{\infty} d_p \{\mathbf{a}^{(p)}, \mathbf{a}^{(q)}\} = \delta_q. \tag{2.77}$$

Exposing the integral $\{\tilde{\mathbf{\Lambda}}, \mathbf{a}^{(p)}\}$ to the same procedure yields

$$\sum_{\substack{p=-\infty \\ p\neq 0}}^{\infty} l_p \{\mathbf{a}^{(p)}, \mathbf{a}^{(q)}\} = \alpha_q, \qquad \alpha_q = \begin{cases} -\frac{15}{4}\frac{\rho_1}{\rho^2}\left(\frac{2k_BT}{m_1}\right)^{\frac{1}{2}} & q = 1 \\ 0 & q \neq \pm 1 \\ -\frac{15}{4}\frac{\rho_2}{\rho^2}\left(\frac{2k_BT}{m_2}\right)^{\frac{1}{2}} & q = -1 \end{cases} \tag{2.78}$$

These sets of linear equations uniquely determine the d_p and l_p expansion coefficients, and thereby uniquely determine the functions $\mathbf{D}$, $\tilde{\mathbf{\Lambda}}$ and $\mathbf{\Lambda}$. For a finite approximation $|p| < N$, $|q| < N$, termed the Nth-order approximation, they may be written in matrix form as

$$\begin{bmatrix} a_{-N-N} & \dots & a_{-N0} & \dots & a_{-NN} \\ \vdots & \ddots & \vdots & & \vdots \\ a_{0-N} & \dots & a_{00} & \dots & a_{0N} \\ \vdots & & \vdots & \ddots & \vdots \\ a_{N-N} & \dots & a_{N0} & \dots & a_{NN} \end{bmatrix} \begin{pmatrix} d_{-N} \\ \vdots \\ d_0 \\ \vdots \\ d_N \end{pmatrix} = \begin{pmatrix} 0 \\ \vdots \\ 0 \\ \delta_0 \\ 0 \\ \vdots \\ 0 \end{pmatrix}, \tag{2.79}$$

$$\begin{bmatrix} a_{-N-N} & \dots & a_{-N-1} & a_{-N1} & \dots & a_{-NN} \\ \vdots & \ddots & \vdots & \vdots & & \vdots \\ a_{-1-N} & \dots & a_{-1-1} & a_{-11} & \dots & a_{-1N} \\ a_{1-N} & \dots & a_{1-1} & a_{11} & \dots & a_{1N} \\ \vdots & & \vdots & \vdots & \ddots & \vdots \\ a_{N-N} & \dots & a_{N-1} & a_{N1} & \dots & a_{NN} \end{bmatrix} \begin{pmatrix} l_{-N} \\ \vdots \\ l_{-1} \\ l_1 \\ \vdots \\ l_N \end{pmatrix} = \begin{pmatrix} 0 \\ \vdots \\ 0 \\ \alpha_{-1} \\ \alpha_1 \\ 0 \\ \vdots \\ 0 \end{pmatrix}, \tag{2.80}$$

Where $a_{pq} \equiv \{\mathbf{a}^{(p)}, \mathbf{a}^{(q)}\} = a_{qp}$. Further, inserting the expansions of $\mathbf{D}$ and $\tilde{\mathbf{\Lambda}}$ into the integrals $\{\mathbf{D}, \mathbf{D}\}$ and $\{\tilde{\mathbf{\Lambda}}, \tilde{\mathbf{\Lambda}}\}$ one arrives at

$$\{\mathbf{D}, \mathbf{D}\} = d_0\delta_0, \qquad \{\tilde{\mathbf{\Lambda}}, \tilde{\mathbf{\Lambda}}\} = l_1\alpha_1 + l_{-1}\alpha_{-1}, \qquad \{\mathbf{D}, \mathbf{\Lambda}\} = d_1\alpha_1 + d_{-1}\alpha_{-1}. \tag{2.81}$$

This means that evaluating the integrals a_{pq} is the final step to obtaining the transport coefficients.

We now take a moment to summarise the significance of these results, and give an overview of the procedure one must follow to obtain a value for the transport coefficients. The next section will then cover how the evaluation is done in practice.

Thus far, we have identified a valid second approximation to the velocity distribution functions for a binary system, given as

$$f_i = f_i^{(0)} \left[1 - \mathbf{\Lambda}_i \nabla \ln T - \mathbf{D}_i \mathbf{d}_{12} - 2\underline{\boldsymbol{B}}_i : \nabla \mathbf{u}^n\right], \quad i = \{1, 2\}. \tag{2.82}$$

This function satisfies the Boltzmann equations, given that $\mathbf{\Lambda}_i$, $\mathbf{D}_i$ and $\underline{\boldsymbol{B}}_i$ satisfy certain constraints posed by the summational invariants. That is, mass, momentum and energy must be conserved. The three functions describe how the vdf will change in response to different driving forces. $\underline{\boldsymbol{B}}$ describes the response to pressure and is connected to the viscosity, which is not investigated in further detail in this work. We have not obtained an explicit functional form for $\mathbf{\Lambda}_i$ and $\mathbf{D}_i$, but have approximated them as a polynomial expansion in the Sonine polynomials. Further, we have determined that the diffusion coefficients and conductivity may be expressed as integrals over $\mathbf{D}$ and $\mathbf{\Lambda}$, given in Equations (2.63), (2.64) and (2.68). It is these integrals we aim to evaluate.

Since $\mathbf{\Lambda}_i$ and $\mathbf{D}_i$ are subject to the constraints posed by the summational invariants, formulated in Equations (2.57), we may impose these constraints on their polynomial expansions. This yields two linear sets of equations which are given in matrix form in Equations (2.79) and (2.80). The first determines the expansion coefficients d_p for the approximation to $\mathbf{D}$, and the second determines the expansion coefficients l_p for the approximation to $\tilde{\mathbf{\Lambda}}$.

Even without determining these expansion coefficients, we may use the orthogonality properties to evaluate the integrals that determine D_T, D_{12} and λ in terms of the expansion coefficients, leading to the expressions in Equation (2.81). To obtain numerical values for the transport coefficients it is therefore necessary to compute the values a_{pq}, which are integrals over the Sonine polynomials, such that we may solve the sets of linear equations that determine the expansion coefficients. Evaluating the a_{pq} integrals is not a trivial task, but in more recent years, solutions have been introduced that greatly simplify it in practice.[37–40] It is these solutions that will be employed at the end of the next section.

2.3.6 The summational expressions

To evaluate the integral $\{\mathbf{a}^{(p)}, \mathbf{a}^{(q)}\}$, Chapman and Cowling begin by inserting the definitions of $\mathbf{a}^{(p)}$ into the integral, and simplifying the expressions by using the orthogonality properties of the polynomials. This gives expressions for a_{pq} in terms of the square bracket

integrals

$$\begin{aligned} a_{pq} &= x_1^2 H_1^{(1)}(p,q) + x_1 x_2 H_{12}^{(1)}(p,q) \\ a_{p-q} &= x_1 x_2 H_{12}^{(12)}(p,q) \\ a_{-pq} &= x_1 x_2 H_{21}^{(21)}(p,q) \\ a_{-p-q} &= x_2^2 H_2^{(2)}(p,q) + x_1 x_2 H_{21}^{(2)}(p,q), \end{aligned} \tag{2.83}$$

where

$$H_1^{(1)}(p,q) \equiv \left[S_{3/2}^{(p)}(\mathscr{U}_1^2)\boldsymbol{\mathscr{U}}_1, S_{3/2}^{(q)}(\mathscr{U}_1^1)\boldsymbol{\mathscr{U}}_1 \right]_1, \tag{2.84}$$

$$H_2^{(2)}(p,q) \equiv \left[S_{3/2}^{(p)}(\mathscr{U}_2^2)\boldsymbol{\mathscr{U}}_2, S_{3/2}^{(q)}(\mathscr{U}_2^1)\boldsymbol{\mathscr{U}}_2 \right]_2, \tag{2.85}$$

$$H_{12}^{(1)}(p,q) \equiv \left[S_{3/2}^{(p)}(\mathscr{U}_1^1)\boldsymbol{\mathscr{U}}_1, S_{3/2}^{(q)}(\mathscr{U}_1^2)\boldsymbol{\mathscr{U}}_1 \right]_{12}, \tag{2.86}$$

$$H_{21}^{(2)}(p,q) \equiv \left[S_{3/2}^{(p)}(\mathscr{U}_2^1)\boldsymbol{\mathscr{U}}_2, S_{3/2}^{(q)}(\mathscr{U}_2^2)\boldsymbol{\mathscr{U}}_2 \right]_{21}, \tag{2.87}$$

$$H_{12}^{(12)}(p,q) \equiv \left[S_{3/2}^{(p)}(\mathscr{U}_1^2)\boldsymbol{\mathscr{U}}_1, S_{3/2}^{(q)}(\mathscr{U}_2^2)\boldsymbol{\mathscr{U}}_2 \right]_{12}, \tag{2.88}$$

$$H_{21}^{(21)}(p,q) \equiv \left[S_{3/2}^{(p)}(\mathscr{U}_2^2)\boldsymbol{\mathscr{U}}_2, S_{3/2}^{(q)}(\mathscr{U}_1^2)\boldsymbol{\mathscr{U}}_1 \right]_{21}. \tag{2.89}$$

Notice that these integrals form three pairs with the same functional form,

$$H_1^{(1)}(p,q) \leftrightarrow H_2^{(2)}(p,q), \qquad H_{12}^{(1)}(p,q) \leftrightarrow H_{21}^{(2)}(p,q), \qquad H_{12}^{(12)}(p,q) \leftrightarrow H_{21}^{(21)}(p,q). \tag{2.90}$$

The only difference between the functions in each pair is swapping the indices. Therefore, one only needs to acquire explicit expressions for half of the integrals.

Further, all information about the intermolecular potential is contained in the integral over dbdg, the relative speed and impact parameter. Integrals over the directions of the velocity may be carried out without specifying any such potential. It is therefore convenient to define the collision integrals $\Omega_{12}^{(\ell)}(r)$ and $\Omega_i^{(\ell)}(r)$, $i = \{1,2\}$ as

$$\begin{aligned} \Omega_{12}^{(\ell)}(r) &\equiv \frac{1}{2}\sigma_{12}^2 \left(\frac{k_B T}{2\pi m_0 M_1 M_2} \right)^{\frac{1}{2}} W_{12}^{(\ell)}(r) \\ W_{12}^{(\ell)}(r) &\equiv 2 \int_0^\infty \exp(-g^2) g^{2r+3} \int_0^\infty \left(1 - \cos^\ell(\chi)\right) \left(\frac{b}{\sigma_{12}}\right) \mathrm{d}\left(\frac{b}{\sigma_{12}}\right) \mathrm{d}g_{12} \end{aligned} \tag{2.91}$$

where $g_{12} = \left(\frac{m_0 M_1 M_2}{2k_B T}\right)^{\frac{1}{2}} g_{12}$ is the non-dimensional relative speed, χ is the deflection angle as illustrated in Figure 2.1, and σ_{ij} is, in general, a scaling parameter with dimensions of length, in the range of the molecular sizes. ℓ and r are integer indices that arise from the manner in which these integrals are separated from those that do not depend on the intermolecular potential. A change of integration variables has been employed to map $\mathrm{d}b\mathrm{d}g_{12} \mapsto d\left(\frac{b}{\sigma_{12}}\right) dg_{12}$. The equivalent expression for $\Omega_i^{(\ell)}(r)$ is

$$\Omega_i^{(\ell)}(r) \equiv \sigma_i^2 \left(\frac{\pi k_B T}{m_1} \right)^{\frac{1}{2}} W_i^{(\ell)}(r), \quad i = \{1,2\} \tag{2.92}$$

where $W_i^{(\ell)}(r)$ is obtained by replacing σ_{12} with σ_i in Equation (2.91), and g_{12} with g_{ii}. These integrals contain all information about how the intermolecular potential effects the collisions, and may be evaluated numerically for any given intermolecular potential by using this potential to relate χ to b and g. This is done for a general spherical potential in Section 2.3.9. In addition, Reid et al. give several methods of approximating the collision integrals under various conditions.[12] However, for a HS-potential the integrals can be evaluated analytically to give

$$\begin{aligned}
\Omega_1^{(\ell),HS}(r) &= (\sigma_1^{HS})^2 \left(\frac{\pi k_B T}{m_1}\right)^{\frac{1}{2}} W_r^{(\ell),HS} \\
\Omega_2^{(\ell),HS}(r) &= (\sigma_2^{HS})^2 \left(\frac{\pi k_B T}{m_2}\right)^{\frac{1}{2}} W_r^{(\ell),HS} \\
\Omega_{12}^{(\ell),HS}(r) &= \frac{1}{2}(\sigma_{12}^{HS})^2 \left(\frac{2\pi k_B T}{m_0 M_1 M_2}\right)^{\frac{1}{2}} W_r^{(\ell),HS} \\
W_r^{(\ell),HS} &= \frac{1}{4}\left[2 - \frac{1}{l+1}\left(1+(-1)^l\right)\right](r+1)!.
\end{aligned} \tag{2.93}$$

Defining the collision integrals in this way, Chapman and Cowling expand the integrals over $\mathbf{u}_1$ and $\mathbf{u}_2$ and determine that the complete bracket integrals of Equations (2.84)-(2.89) may be written as linear combinations of the collision integrals,

$$\begin{aligned}
H_1^{(1)}(p,q) &= 8 \sum_{l=2}^{(\min[p,q]+1)} \sum_{r=l}^{(p+q+2-\ell)} A'''_{pqr\ell}\Omega_1^{(\ell)}(r) \\
H_{12}^{(1)}(p,q) &= 8 \sum_{l=1}^{(\min[p,q]+1)} \sum_{r=l}^{(p+q+2-\ell)} A'_{pqr\ell}\Omega_{12}^{(\ell)}(r) \\
H_{12}^{(12)}(p,q) &= 8M_2^{(p+\frac{1}{2})}M_1^{(q+\frac{1}{2})} \sum_{l=1}^{(\min[p,q]+1)} \sum_{r=l}^{(p+q+2-l)} A_{pqr\ell}\Omega_{12}^{(\ell)}(r)
\end{aligned} \tag{2.94}$$

with $A_{pqr\ell}$, $A'''_{pqr\ell}$ as yet undetermined weights, independent of any molecular properties. $A'_{pqr\ell}$ is an undetermined number that is a function of the particle masses. Note that only three of the integrals of Equations (2.84)-(2.89) are given, the rest are obtained via appropriate index swapping. Identifying explicit expressions for these weights is an abnormally extensive exercise in analytical integration and pattern matching that was carried out by Thompson et al.[37–40] For the derivation the reader is referred to their papers. The results they give are

$$\begin{aligned}
A'''_{pqr\ell} = &\left(\frac{1}{2}\right)^{(p+q+1)} \sum_{i=(l-1)}^{(\min[p,q,r,(p+q+1-r)])} \frac{8^i(p+q-2i)!\left(1+(-1)^l\right)}{(p-i)!(q-i)!(\ell)!(i+1-l)!} \\
&\times \frac{(-1)^{(r+i)}(r+1)!(2(p+q+2-i))!2^{2r}}{(r-i)!(p+q+1-i-r)!(2r+2)!(p+q+2-i)!4^{(p+q+1)}} \\
&\times \left[(i+1-l)(p+q+1-i-r) - \ell(r-i)\right],
\end{aligned} \tag{2.95}$$

$$
\begin{aligned}
A'_{pqr\ell} = & \sum_{i=(l-1)}^{\min[p,q,r,(p+q+1-r)]} \sum_{k=(l-1)}^{\min[l,i]} \sum_{w=0}^{(\min[p,q,(p+q+1-r)]-i)} \frac{8^i (p+q-2i-w)!}{(p-i-w)!(q-i-w)!} \\
& \times \frac{(-1)^{(r+i)}(r+1)!(2(p+q+2-i-w))!4^{(r+w)}F^{(i+k)}G^w M_1^i M_2^{(p+q-i-w)}}{(r-i)!(p+q+1-i-r-w)!(2r+2)!(p+q+2-i-w)!4^{(p+q+1)}(k)!(i-k)!(w)!} \\
& \times \left(M_1(p+q+1-i-r-w)\delta_{k,l} - M_2(r-i)\delta_{k,(l-1)}\right), \\
& F \equiv \frac{M_1^2+M_2^2}{M_1 M_2}, \qquad G \equiv \frac{M_1-M_2}{M_2},
\end{aligned}
\tag{2.96}
$$

$$
\begin{aligned}
A_{pqr\ell} = & \sum_{i=(l-1)}^{\min[p,q,r,(p+q+1-r)]} \frac{8^i (p+q-2i)!}{(p-i)!(q-i)!(\ell)!(i+1-l)!(r-i)!} \\
& \times \frac{(-1)^{(l+r+i)}(r+1)!(2(p+q+2-i))!4^r}{(p+q+1-i-r)!(2r+2)!(p+q+2-i)!4^{(p+q+1)}} \\
& \times \left[(i+1-l)(p+q+1-i-r) - \ell(r-i)\right].
\end{aligned}
\tag{2.97}
$$

With explicit expressions for these factors, one must only evaluate the required collision integrals in order to obtain the factors a_{pq} required to compute the diffusion coefficient, thermal diffusion coefficient and conductivity up to an arbitrary order of approximation. In practice, it is rare to pass beyond the 5th order approximation,[41] and it has been shown that computational limitations regarding floating point precision make it non-trivial to pass beyond the 7th-10th order of approximation, depending on conditions.[25]

2.3.7 The high density regime

The transport coefficients obtained from the Enskog solutions are known to deviate significantly from those measured at high densities. This is due to the theory describing a situation in which interactions are exclusively binary, and that the time between interactions is far larger than the time during which interactions occur. This implies that transport occurs via the motion of molecules between collisions, while the transfer of e.g. momentum from one molecule to the next during a collision is neglected. This is an inaccurate description of dense fluids, where interactions are far more common, and transfer of momentum and energy during collisions accounts for a significant portion of the total transport. As mentioned previously, the requirement of long time between collisions is a manner of saying that one requires subsequent collisions between particles to be uncorrelated.

The following "high density corrections" to the Boltzmann equations, often termed the Enskog equations,[36] take into account the first shortcoming of of the theory thus far; namely the occurrence of transport during collisions and the increased frequency of collisions due to a significant excluded volume at high densities. The latter issue, that of subsequent collisions in fact being correlated in dense fluids is not treated here. This is due to the first issue having explicit solutions that do not require additional parameters to

be added to the model that is to be implemented, while still greatly improving accuracy in the medium density regime. The latter issues requires that one has accurate available information about the structure factor and/or radial distribution function of the fluid in question. These are typically obtained either by simulation or experiment, and are in general not directly available from an intermolecular potential. Including these corrections would therefore somewhat restrict the fluids to which the model could be applied. In this work, the possibility of applying the model to a wider variety of mixtures at low to medium densities was considered to be of greater benefit than an increase in precision at liquid-like densities.

To account for the increase in collision frequency due to the excluded volume, Enskog introduces the function $\tilde{\chi}$, such that the probability of any two particles of species 1 occupying a volume in phase space $d\mathbf{u}_{1'}d\mathbf{u}_1\mathrm{d}\mathbf{r}$ is

$$\tilde{\chi}(\mathbf{r})f_{1'}f_1 d\mathbf{u}_{1'}d\mathbf{u}_1\mathrm{d}\mathbf{r} \tag{2.98}$$

Where $\tilde{\chi}$ is required to go to unity as the density goes to zero, and increase with increasing density. This will later be recognised as the pair distribution function. Furthermore, $\tilde{\chi}$ is assumed to be independent of the velocities. In the derivation outlined so far, this modification only serves to change the form of $\frac{\partial_e f}{\partial t}$, the change in the velocity distribution function owing to collisions. Following the derivation with this modification yields both easily applicable results, and some questions that are open to interpretation. For the full derivation the reader is referred to the derivation by Thorne.[42] Here, focus will be placed on the resulting correction factors, how to obtain them, and their interpretation.

The first result to note is that to a first approximation, for a single component system of hard spheres, the equations of conservation may be written in a form identical to that obtained without the density correction, only making the replacement

$$k_B\rho T \mapsto k_B\rho T\left(1+\frac{2\pi}{3}\rho\sigma^3\tilde{\chi}\right). \tag{2.99}$$

Recognising $k_B\rho T$ as the hydrostatic pressure of an ideal gas gives the insight that $\tilde{\chi}$ is intimately related to the second virial coefficient. Furthermore, the perturbation function of the second approximation to the vdf. given in Equation (2.49), is modified only by a multiplicative factor giving

$$\Phi_1^{(1)} \mapsto \frac{5+2\pi\rho\sigma^3\tilde{\chi}}{5\tilde{\chi}}\Phi_1^{(1)}. \tag{2.100}$$

This prefactor leads to the results

$$\begin{aligned}\lambda &= \frac{\left(1+\frac{2}{5}\pi\rho\sigma^3\tilde{\chi}\right)^2}{\tilde{\chi}}\lambda^\infty + \frac{2k_B}{3m}\tilde{\chi}\rho^2\sigma^4\left(\pi m k_B T\right)^{\frac{1}{2}} \\ D_{11} &= \frac{D_{11}^\infty}{\tilde{\chi}}\end{aligned} \tag{2.101}$$

where λ is the conductivity, D_{11} is the self diffusion coefficient, and the superscript ∞ indicates the solutions to the equations valid at infinite dilution, i.e. those presented previously in Section 2.3.5.

The binary case follows the same approach as the unary. First, introduce the functions $\tilde{\chi}_1$, $\tilde{\chi}_2$ and $\tilde{\chi}_{12}$ that modify the probability of any two particles occupying a volume in phase space. Regarding the pressure, this leads to a result similar to the unary case,

$$\begin{aligned} p_1 &= \rho k_B T \left(x_1 + \frac{2\pi}{3} \rho_1 \left[x_1 \sigma_1^3 \tilde{\chi}_1 + x_2 \sigma_1 2^3 \tilde{\chi}_{12} \right] \right) \\ p_2 &= \rho k_B T \left(x_2 + \frac{2\pi}{3} \rho_1 \left[x_2 \sigma_1^3 \tilde{\chi}_2 + x_1 \sigma_1 2^3 \tilde{\chi}_{12} \right] \right) \\ p &= p_1 + p_2. \end{aligned} \tag{2.102}$$

Also for the interdiffusion coefficient, a simple correction is obtained with

$$D_{12} = \frac{D_{12}^{\infty}}{\tilde{\chi}_{12}} \tag{2.103}$$

The corrections for the thermal conductivity and thermal diffusion ratio are somewhat more involved, and are not given here. The question that remains is what value to use for $\tilde{\chi}$. In the the publications by Chapman and Cowling, a value for $\tilde{\chi}$ for hard spheres is computed by regarding the excluded volume, which increases the probability of collisions, and the effect that particles can shield each other, which reduces the probability of collision. Neglecting the possibility of ternary and higher order collisions, they end up with the value

$$\tilde{\chi}^E(\rho; \sigma^{HS}) = 1 + \frac{5}{12} \pi \rho \left(\sigma^{HS} \right)^3 \tag{2.104}$$

Enskog suggests to use the connection between $\tilde{\chi}$ and the second virial coefficient to estimate its value either from measurements by computing the second virial coefficient from some established EoS.[42] Other authors recognise $\tilde{\chi}$ as the radial distribution function (rdf.) evaluated at particle contact, and suggest that its value is obtained from either experiments such as neutron scattering, simulations or some known expression for the rdf.[36] For a system of hard spheres, one can obtain from the CS EoS that,[31]

$$\tilde{\chi}^{CS}(\rho; \sigma^{HS}) = \frac{1 - \frac{1}{2}\eta}{(1-\eta)^3}, \quad \eta = \frac{\pi}{6} \rho \left(\sigma^{HS} \right)^3, \tag{2.105}$$

where $\tilde{\chi}^{CS}$ is the rdf. at contact. This function is tempting to use, as it has the desired property of describing the probability of two particles being in contact, and has been shown to be accurate for hard sphere systems.

Making a Taylor expansion of $\tilde{\chi}^{CS}$ about $\rho = 0$, one quickly finds that $\tilde{\chi}^E$ is exactly equal to the first order expansion. Chapman and Cowling also give a numerical value for an expansion of $\tilde{\chi}^E$ to second order in ρ that coincides closely with the second order Taylor expansion of $\tilde{\chi}^{CS}$. These observations are in agreement with recommendations in the literature that one should obtain a value for $\tilde{\chi}$ from the rdf. at contact.[36] Therefore, $\tilde{\chi}^{CS}$ is chosen as the starting point from which to determine a value for $\tilde{\chi}$ in Section 2.3.10.

2.3.8 Intermediate summary

Though the derivations outlined above are somewhat lengthy, recognise that we have arrived at an explicit set of equations that can be solved for the diffusion and thermal diffusion coefficient once the collision integrals have been evaluated. For a hard sphere potential an analytical expression for the collision integrals is available. To obtain the transport coefficients for a hard sphere mixture at the Nth approximation, the procedure is to first compute the a_{pq}, $(p,q) \in (-N,N) \times (-NN)$ matrix elements, by using the summational expressions given in Equation 2.94. Then, the matrix Equation (2.79) can be solved to obtain the coefficients d_{-1}, d_0 and d_1. The transport coefficients are computed from these with Equations (2.81) by using the definitions in Equations (2.63) and (2.64). The procedure for computing the conductivity is equivalent, as the conductivity is related to the integral $\{\tilde{\mathbf{\Lambda}}, \tilde{\mathbf{\Lambda}}\}$, and thereby the to the expansion coefficients l_p.

The presented density corrections, which have been shown to be accurate at low to medium densities, do not enter the computation until the final step. Employing them thus consists of computing the non-corrected transport coefficients before applying Equations (2.101) or (2.103). The only remaining question in this regard is what value one should use for $\tilde{\chi}$ if the employed potential model is not that of a rigid sphere.

Note that the equations presented thus far are valid for any potential model. Information about the intermolecular potential is contained within the collision integrals, and the factor $\tilde{\chi}$. For hard spheres analytical expressions for both have been presented. The remainder of this section will treat the evaluation of the collision integrals and $\tilde{\chi}$ for a spherical potential that is not a hard sphere.

2.3.9 The dynamics of a collision

To evaluate the collision integrals for a more complex potential than the hard sphere, a more detailed analysis of the particle collision dynamics than that presented in Section 2.3.1 is required. Here, the relationship between the deflection angle, χ, impact parameter b and dimensionless relative speed, g will be derived for an arbitrary spherically symmetric potential that vanishes at infinite separation. Thus making it possible to evaluate the dimensionless collision integral

$$W_{\ell,r} = 2\int_0^\infty \int_0^\infty \exp\left(-g^2\right) g^{2r+3} \left[1 - \cos^\ell\left(\chi\left(g,b\right)\right)\right] \left(\frac{b}{\sigma}\right) \mathrm{d}\left(\frac{b}{\sigma}\right) \mathrm{d}g. \tag{2.106}$$

Where ℓ and r are integer parameters that enter the equation through the derivation of the summational expressions given in Section 2.3.6. The significance of the variables is illustrated in Figures 2.3, 2.4 and 2.5. Chapman and Cowling give a derivation of the relationship for a purely repulsive potential,[9] but it is not immediately clear what the consequences are if the potential consists of both a repulsive and an attractive part. Therefore, rather than directly using the results from Chapman and Cowling, the derivation given here has been done to ensure that the results are valid for an arbitrary spherical potential. The final results are in accordance with those reported by Chapman and Cowling.

The final evaluation of the results requires a combination of numerical root solving and integration that is described further in Section 3.1.

The dynamics of a collision between two particles is governed by conservation of mass and momentum. To begin, denote the position of the centre of mass of the particles as $\mathbf{r}_1$ and $\mathbf{r}_2$. The intermolecular distance is $\mathbf{r}_{12} \equiv \mathbf{r}_2 - \mathbf{r}_1$. The force acting on the particles is then $\mathbf{F}_1 = \frac{\partial u_{12}(\mathbf{r}_{12})}{\partial \mathbf{r}_1} = -\frac{\partial u_{12}(\mathbf{r}_{12})}{\partial \mathbf{r}_{12}} = -\frac{\partial u_{12}(\mathbf{r}_{12})}{\partial \mathbf{r}_2} = -\mathbf{F}_2 \equiv -\mathbf{F}$, where u denotes the intermolecular potential. Newtons second law for the two particles is then

$$m_1 \ddot{\mathbf{r}}_1 = -\mathbf{F}, \qquad m_2 \ddot{\mathbf{r}}_2 = \mathbf{F}. \tag{2.107}$$

Where Newton notation, $\dot{\varphi}$ is used to indicate time-derivatives. To simplify further calculations, recognise that

$$\begin{aligned} m_1 m_2 \ddot{\mathbf{r}}_{12} &= m_1 m_2 (\ddot{\mathbf{r}}_2 - \ddot{\mathbf{r}}_1) = (m_1 + m_2)\mathbf{F} \\ &= m_0 \mathbf{F} \\ \ddot{\mathbf{r}}_{12} &= \frac{m_0}{m_1 m_2}\mathbf{F} = \frac{m_0}{m_1 m_2}\frac{\partial u_{12}}{\partial \mathbf{r}_{12}}, \end{aligned} \tag{2.108}$$

where $m_0 = m_1 + m_2$. That is, the two-particle system behaves equivalently to a single particle of unit mass orbiting a stationary potential $\frac{m_0}{m_1 m_2} u_{12}$, or a single particle of reduced mass $\frac{m_1 m_2}{m_0}$ orbiting a stationary potential u_{12}. The former, illustrated in Figure 2.3 is arbitrarily chosen as a basis for the remaining analysis in this section, and will be referred to as the single-particle frame of reference (FoR).

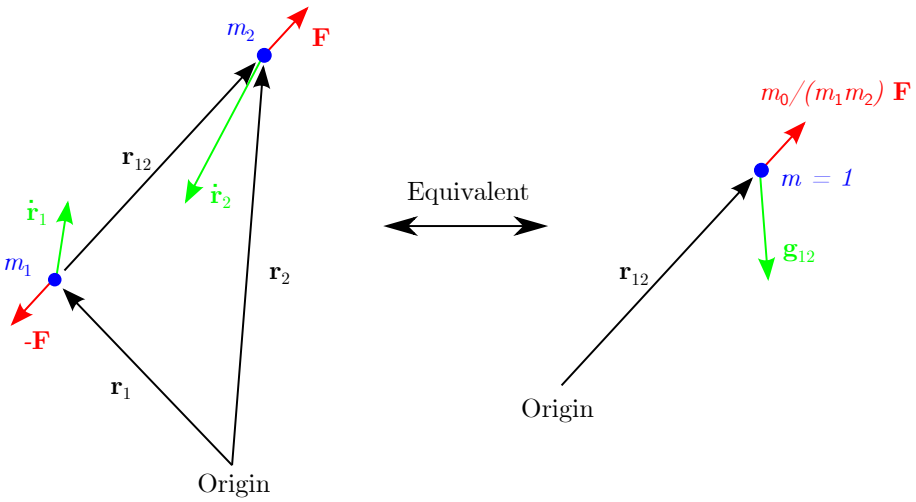

Figure 2.3: Illustration of two equivalent descriptions of the two particle system. Left: Two particles, each the centre of a potential u_{12}. Right: A single particle of unit mass with velocity $\mathbf{g}_{12}$, orbiting a stationary potential $\frac{m_0}{m_1 m_2} u_{12}$.

Due to conservation of angular momentum, the plane of orbit is constant. It is therefore convenient to define a polar coordinate system in this plane, as illustrated in Figure 2.4 to analyse the interaction. Furthermore, in the following analysis, the subscript on r is dropped as the treatment is now that of a one-particle system. Keep in mind that the distance r in the one-particle system is equivalent to r_{12} in the two-particle system. Keep

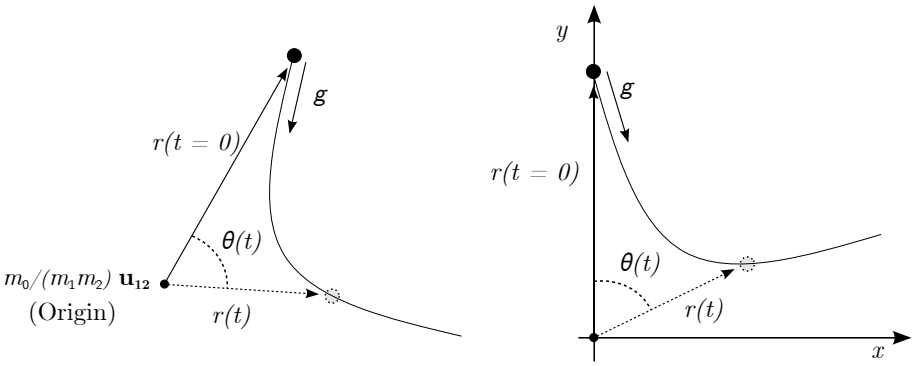

Figure 2.4: The polar coordinate system, and corresponding cartesian coordinate system in the plane of orbit.

also in mind that $r(t=0) = \infty$, such that the velocity $\mathbf{g}$ is the relative velocity of the particles before they begin to interact.

Denoting the position in cartesian coordinates as $\mathbf{s} = [r\sin\theta, r\cos\theta]$, and the velocity as $\dot{\mathbf{s}} = \left[\dot{r}\sin\theta + r\dot{\theta}\cos\theta, \dot{r}\cos\theta - r\dot{\theta}\sin\theta\right]$, the angular momentum of the particle is

$$\begin{aligned} L &= |\mathbf{s}\times\dot{\mathbf{s}}| \\ &= \left|r\sin\theta\left(\dot{r}\cos\theta - r\dot{\theta}\sin\theta\right) - r\cos\theta\left(\dot{r}\sin\theta + r\dot{\theta}\cos\theta\right)\right| \\ &= r^2\dot{\theta}. \end{aligned} \tag{2.109}$$

At $t = 0$ the angular momentum is

$$\begin{aligned} L &= |\mathbf{r}\times\mathbf{g}| \\ &= |\mathbf{r}||\mathbf{g}|\sin\left(\angle\{\mathbf{r},\mathbf{g}\}\right) \\ &= gb \end{aligned} \tag{2.110}$$

Where the final equivalency is acquired by noting that $r(0)\sin\left(\angle\{\mathbf{r},\mathbf{g}\}\right) = b$, as can be seen in Figure 2.5. The governing equation for angular momentum is thus

$$r^2\dot{\theta} = gb. \tag{2.111}$$

Conservation of energy must also be obeyed. At any time, the kinetic energy of the particle is $\frac{1}{2}|\dot{\mathbf{s}}|^2$, the total mechanical energy is thereby

$$\begin{aligned} E_{tot}^{mec} &= \frac{1}{2}|\dot{\mathbf{s}}|^2 + \frac{m_0}{m_1 m_2}u_{12}(r) \\ &= \frac{1}{2}\left(\dot{r}^2 + r^2\dot{\theta}^2\right) + \frac{m_0}{m_1 m_2}u_{12}(r). \end{aligned} \tag{2.112}$$

At $t = 0$ the velocity of the particle is $\mathbf{g}$ and the potential vanishes at infinite distance, such that the governing equation for conservation of energy is

$$\frac{1}{2}\left(\dot{r}^2 + r^2\dot{\theta}^2\right) + \frac{m_0}{m_1 m_2}u_{12}(r) = \frac{1}{2}g^2. \tag{2.113}$$

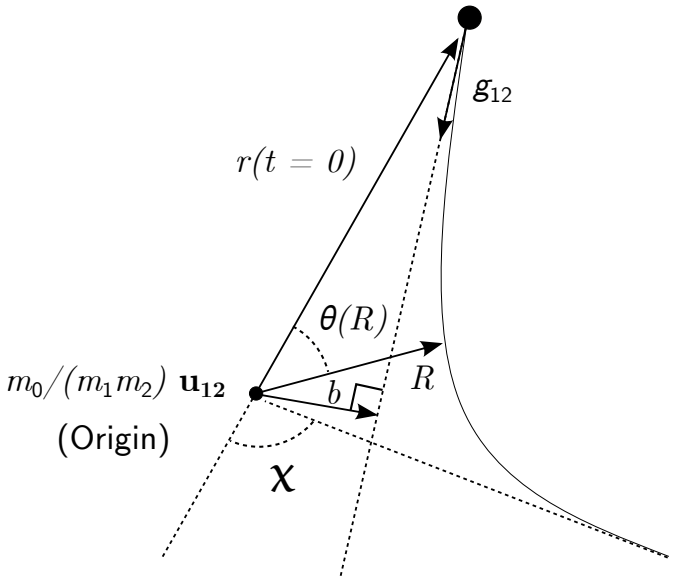

Figure 2.5: The distance of closest approach R, impact parameter b and deflection angle χ illustrated in the single-particle FoR.

Recognise that due to the symmetry of the intermolecular potential, $\chi(g,b) = \pi - 2\theta(R;g,b)$, where R is the distance of closest approach, as illustrated in Figure 2.5, and the semicolon indicates a parametric dependency. Now that the governing equations for the orbit have been developed, $\chi(g,b)$ will be determined by obtaining an explicit expression for $\theta(R;g,b)$. As R, and thereby χ, is not time-dependent, time can be eliminated from the governing equations without losing relevant information. This is accomplished by rewriting Equation 2.113 as

$$\frac{1}{2}\left[\left(\frac{\mathrm{d}r}{\mathrm{d}\theta}\right)^2 + r^2\right]\dot{\theta}^2 + \frac{m_0}{m_1m_2}u_{12}(r) = \frac{1}{2}g^2. \tag{2.114}$$

Inserting for $\dot{\theta}$ from Equation 2.111 yields

$$\frac{1}{2}\frac{g^2b^2}{r^4}\left[\left(\frac{\mathrm{d}r}{\mathrm{d}\theta}\right)^2 + r^2\right] + \frac{m_0}{m_1m_2}u_{12}(r) = \frac{1}{2}g^2. \tag{2.115}$$

To find the distance of closest approach, solve this equation as

$$\begin{aligned}\frac{\mathrm{d}r}{\mathrm{d}\theta} &= \pm\left(\frac{r^4}{b^2}\left[1 - \frac{2}{g^2}\frac{m_0}{m_1m_2}u_{12}(r)\right] - r^2\right)^{\frac{1}{2}} \\ &= \pm\left(\frac{r^4}{b^2}\left[1 - \frac{u_{12}(r)}{k_BTg^2}\right] - r^2\right)^{\frac{1}{2}}.\end{aligned} \tag{2.116}$$

Where $g = \left(\frac{m_1m_2}{2m_0k_BT}\right)^{\frac{1}{2}}\mathbf{g}$ is the dimensionless relative speed introduced in Section 2.3. It is evident that R is found at the point where $\frac{\mathrm{d}r}{\mathrm{d}\theta} = 0$, or

$$\frac{R^4}{b^2}\left[1 - \frac{u_{12}(R)}{k_BTg^2}\right] - R^2 = 0. \tag{2.117}$$

For some general collision, this equation may have several roots, corresponding to stable orbits. However, because we consider a situation where the particles start at infinite separation, simply requiring that the particles rotational or vibrational energy cannot change is enough to ensure that no such stable orbit exists. Due to conservation of energy, even a particle starting with $g = 0$ at infinite distance will always remain exactly at the escape velocity of the potential. Any particle with $g > 0$ will always have a velocity greater than the escape velocity.

To obtain an expression for θ, we invert Equation (2.116) such that

$$\frac{\mathrm{d}\theta}{\mathrm{d}r} = \pm\left(\frac{r^4}{b^2}\left[1 - \frac{u_{12}(r)}{k_B T g^2}\right] - r^2\right)^{-\frac{1}{2}}. \tag{2.118}$$

From the geometry of the encounter it is evident that

$$\frac{\mathrm{d}\theta}{\mathrm{d}r} = \left(\frac{r^4}{b^2}\left[1 - \frac{u_{12}(r)}{k_B T g^2}\right] - r^2\right)^{-\frac{1}{2}} \times \begin{cases} -1, & \theta < \theta(R; g, b, T) \\ 1, & \theta > \theta(R; g, b, T) \end{cases} \tag{2.119}$$

As θ is strictly increasing as a function of time, while r is decreasing until $\theta = \theta(R)$, after which r increases. Integrating Equation (2.119) now gives an explicit expression for θ,

$$\begin{aligned} \theta(r') &= \int_{\infty}^{r'} \left(\frac{\mathrm{d}\theta}{\mathrm{d}r}\right) \mathrm{d}r \\ \int_0^{\theta(R;g,b,T)} \mathrm{d}\theta &= \int_{\infty}^{R} -\left(\frac{r^4}{b^2}\left[1 - \frac{u_{12}(r)}{k_B T g^2}\right] - r^2\right)^{-\frac{1}{2}} \mathrm{d}r \\ \theta(R; g, b, T) &= \int_R^{\infty} \left(\frac{r^4}{b^2}\left[1 - \frac{u_{12}(r)}{k_B T g^2}\right] - r^2\right)^{-\frac{1}{2}} \mathrm{d}r. \end{aligned} \tag{2.120}$$

The dimensionless collision integral may now be evaluated numerically, the specifics of the numerics are presented in Section 3.1. In essence, for a given g, b, T the value of χ is given as

$$\chi(g, b; T) = \pi - 2\theta(R; g, b, T), \tag{2.121}$$

as shown geometrically in Figure 2.5. To evaluate the integrand of Equation (2.106) at a single point one must first solve Equation (2.117) for R, then evaluate the integral of Equation (2.120) to obtain θ from which χ is computed.

2.3.10 Evaluation of $\tilde{\chi}$

Until now, the intermolecular potential has been regarded as some arbitrary, spherical potential. From this point onwards, considerations will be restricted to a Mie potential, given as

$$u_{ij}^{Mie} = C\varepsilon_{ij}\left[\left(\frac{\sigma_{ij}}{r_{ij}}\right)^{\lambda_{r,ij}} - \left(\frac{\sigma_{ij}}{r_{ij}}\right)^{\lambda_{a,ij}}\right], \quad C = \frac{\lambda_{r_{ij}}}{\lambda_{r,ij} - \lambda_{a,ij}}\left(\frac{\lambda_{r,ij}}{\lambda_{a,ij}}\right)^{\frac{\lambda_{a,ij}}{\lambda_{r,ij} - \lambda_{a,ij}}}, \tag{2.122}$$

where ε is the potential well depth, σ_{ij} is the molecular size parameter and $\lambda_{a,ij}$ and $\lambda_{r,ij}$ are adjustable exponents. The use of $\tilde{\chi}^{CS}$, introduced in Section 2.3 as

$$\tilde{\chi}^{CS}(\rho;\sigma^{HS}) = \frac{1-\frac{1}{2}\eta}{(1-\eta)^3}, \quad \eta = \frac{\pi}{6}\rho\left(\sigma^{HS}\right)^3, \tag{2.123}$$

thereby implies an assumption that the rdf. of a Mie fluid at distances in the order of σ resemble that of a hard sphere fluid. There is also the underlying assumption that $\tilde{\chi}$ is independent of particle velocities, and that one may therefore use its equilibrium value even in the non-uniform state.

The question arising now is what value to use for σ when employing the CS-rdf at contact. As mentioned in Section 2.2, the SAFT-VR Mie EoS uses a hard sphere system as a reference state, and utilises the Barker-Henderson diameter to represent the hard-sphere diameter of the reference fluid. Papaioannou et. al. state that the choice of a hard sphere reference is due to the requirement of a highly accurate rdf for the reference fluid.[43] Still, the physical interpretation of the BH-diameter is dubious. Therefore a different diameter, more closely related to the physics of the collision is chosen here.

For the particle diameter, the idea is to take the average distance of closest approach (R) for particles that deflect, $\bar{\sigma}$. Deflection is here taken to mean interactions where $R > b$, that is, where the interaction has prevented one particle from entering the volume occupied by another.

It can be shown from Equation (2.117) that for any Mie potential, $R(\sigma, g) = \sigma$, and $R(b, g) > b \; \forall \; b < \sigma$. Thereby, the average is to be taken over all velocities and for b from 0 to σ. Formally

$$\bar{\sigma}_{ij} = \frac{1}{n_i n_j \sigma_{ij}} \int_0^\infty \int_0^\infty \int_0^{\sigma_{ij}} f_i f_j R(g_{ij}, b) \mathrm{d}b \mathrm{d}\mathbf{u}_i \mathrm{d}\mathbf{u}_j \tag{2.124}$$

where

$$n_i n_j \sigma_{ij} = \int_0^\infty \int_0^\infty f_i f_j \int_0^{\sigma} \mathrm{d}b \mathrm{d}\mathbf{u}_i \mathrm{d}\mathbf{u}_j \tag{2.125}$$

is a normalising factor. The integral of Equation (2.124) could be solved numerically, but this was decided against, largely because the resulting expression for $\bar{\sigma}_{ij}$ would contain the parameter $\tilde{\chi}$, leaving a polynomial equation in $\tilde{\chi}$ with potentially several roots upon inserting the expression into (2.123). While this would be a soluble problem, the benefit of the potential increase in precision in the evaluation $\bar{\sigma}$ is highly uncertain. Therefore the integral was simplified, first by assuming that the effect of particles deviating from the average particle velocity would largely cancel and therefore be insignificant. Specifically, the effect of low collision velocities is to increase the value of the integrand of Equation (2.124), while high collision velocities reduce it. Therefore, for particles of like type, the integral is simplified by simply using the average particle speed $\bar{u}_i = \sqrt{\frac{2k_B T}{m_i}}$ rather than integrating over the velocity distributions. For particles of the same type, this together gives the simplified integral

$$\bar{\sigma}_{ii} \approx \frac{1}{\sigma_i} \int_0^{\sigma_i} R(\bar{u}_i, b) \mathrm{d}b. \tag{2.126}$$

For particles of unlike type, under the standard assumption of uncorrelated collisions, the average relative speed at collisions is

$$\bar{g}_{ij} = \frac{\bar{u}_i + \bar{u}_j}{2}. \tag{2.127}$$

Thereby,

$$\bar{\sigma}_{ij} = \frac{1}{\sigma_{ij}} \int_0^{\sigma_{ij}} R(\bar{g}_{ij}, b) \mathrm{d}b. \tag{2.128}$$

This approach was chosen primarily for its simplicity, as this work focuses on behaviour in the low density region. For the results presented on conductivity in mixtures in Section 4.3, the single component density correction given in Equation (2.101) was applied, using the $\tilde{\chi}$ computed from an average $\bar{\sigma}$, computed as

$$\bar{\sigma} = \sum_i \sum_j x_i x_j \bar{\sigma}_{ij}. \tag{2.129}$$

The value of $\tilde{\chi}$ is thereby computed as

$$\tilde{\chi}_{ij} = \frac{1 - \frac{1}{2}\eta}{(1-\eta)^3}, \quad \eta = \frac{\pi}{6}\rho\bar{\sigma}_{ij}^3 \tag{2.130}$$

for pure fluids and for the diffusion correction in binary mixtures, whilst for the conductivity correction

$$\tilde{\chi} = \frac{1 - \frac{1}{2}\eta}{(1-\eta)^3}, \quad \eta = \frac{\pi}{6}\rho\bar{\sigma}^3 \tag{2.131}$$

is used in combination with the conductivity correction for a pure fluid. More accurate values for $\tilde{\chi}$ can be obtained if one is interested in employing Enskog theory directly to describe behaviour in the dense gas or low-density supercritical region, but this is somewhat more involved than the solution presented here.[9,36]

2.4 The Kempers Model

In this section, the derivation of the models proposed by Kempers will be presented.[15,19] The model is developed by regarding a closed two-bulb system, as illustrated in Figure 2.6, the two containers are kept at uniform temperature, pressure and composition, while the connecting tube is of negligible volume. The underlying assumptions are that the steady state of this system, when the containers are at different temperatures, is the state with a maximum in the canonical partition function (Q). The bulbs will be denoted with superscript α and β, symbols lacking a superscript will be used to refer to the system as a whole. It is further assumed that the Soret coefficient in an ideal gas mixture, denoted with superscript ig, is accurately described by kinetic gas theory.

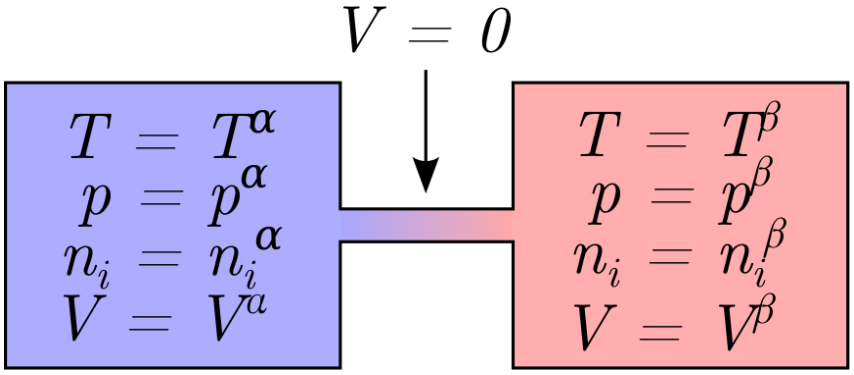

Figure 2.6: Illustration of the Kempers two-bulb system. The two containers are homogeneous, the connecting tube has negligible volume.

2.4.1 The 1989-approach

Instead of treating the problem of two bulbs that exchange particles, the bulbs may be treated as independent subsystems, under the constraint of total particle number conservation. In that case, $Q = Q^\alpha Q^\beta$ and $n_i^\alpha + n_i^\beta = n_i \ \forall \ i$. Additionally, the two subsystems are held at constant and equal volume, such that $\sum_i v_i^\alpha n_i^\alpha = \sum_i v_i^\beta n_i^\beta = \frac{V}{2}$, with V as the total system volume and v_i as the partial molar volume of species i. Under the current assumptions, the steady state compositions for given temperatures T^α and T^β are then given by the constrained maximisation

$$\begin{aligned} \max_{n_i^\alpha, n_i^\beta} \left\{ Q^\alpha Q^\beta \right\} &= \max_{n_i^\alpha, n_i^\beta} \left\{ \exp\left(-\frac{A^\alpha}{k_B T^\alpha} - \frac{A^\beta}{k_B T^\beta} \right) \right\} \\ &= \min_{n_i^\alpha, n_i^\beta} \left\{ \frac{A^\alpha}{T^\alpha} + \frac{A^\beta}{T^\beta} \right\} \\ n_i^\alpha + n_i^\beta &= n_i, \quad \forall \quad i \\ \sum_i v_i^\alpha n_i^\alpha &= \sum_i v_i^\beta n_i^\beta \end{aligned} \tag{2.132}$$

The subscripts on the min and max operators indicate the optimisation variables, and are to be understood such that for some function $\psi(\varphi_1, \varphi_2)$,

$$\begin{aligned} \max_{\varphi_1, \varphi_2} \left\{ \psi \right\} = \left(\varphi_1^{extrema}, \varphi_2^{extrema} \right) = \min_{\varphi_1, \varphi_2} \left\{ -\psi \right\} \\ \psi \left(\varphi_1^{extrema}, \varphi_2^{extrema} \right) = \psi_{max} \end{aligned} \tag{2.133}$$

By the Lagrange multiplier method, the target function corresponding to this optimisation is

$$\mathcal{L}\left(\mathbf{n}^\alpha, \mathbf{n}^\beta, \boldsymbol{\phi}, \gamma \right) = \frac{A^\alpha}{T^\alpha} + \frac{A^\beta}{T^\beta} - \sum_i \phi_i \left(n_i^\alpha + n_i^\beta - n_i \right) - \gamma \sum_i v_i^\alpha n_i^\alpha - v_i^\beta n_i^\beta \tag{2.134}$$

with ϕ and γ as the Lagrange multipliers. Differentiating with respect to the optimisation

variables yields the set of equations

$$\begin{aligned} \frac{\mu_i^\alpha}{T^\alpha} - \phi_i - \gamma v_i^\alpha = 0 \\ \frac{\mu_i^\beta}{T^\beta} - \phi_i + \gamma v_i^\beta = 0 \end{aligned} \tag{2.135}$$

Subtracting these two equations eliminates the ϕ_i, such that

$$\begin{aligned} \frac{\mu_i^\alpha}{T^\alpha} - \frac{\mu_i^\beta}{T^\beta} - \gamma \left(v_i^\alpha + v_i^\beta \right) = 0 \\ \underset{\alpha,\beta}{\Delta} \left(\frac{\mu_i}{T} \right) - \gamma \left(v_i^\alpha + v_i^\beta \right) = 0, \qquad i = \{1, ..., N\} \end{aligned} \tag{2.136}$$

where the notation $\underset{\alpha,\beta}{\Delta} \varphi \equiv \varphi^\alpha - \varphi^\beta$ has been introduced to denote the difference between the bulbs. Solving this equation for γ with $i = k$ gives

$$\gamma = \frac{1}{v_k^\alpha + v_k^\beta} \underset{\alpha,\beta}{\Delta} \left(\frac{\mu_k}{T} \right) \tag{2.137}$$

Inserting this back into the remaining $N - 1$ equations gives

$$\underset{\alpha,\beta}{\Delta} \left(\frac{\mu_i}{T} \right) - \left(\frac{v_i^\alpha + v_i^\beta}{v_k^\alpha + v_k^\beta} \right) \underset{\alpha,\beta}{\Delta} \left(\frac{\mu_k}{T} \right) = 0, \qquad i = \{1, ..., N\} \setminus \{k\}. \tag{2.138}$$

Dividing through by the length of the tube, Δz and taking the limit $\Delta z \to 0$, $\underset{\alpha,\beta}{\Delta} T \to 0$ yields the set of equations

$$\nabla \left(\frac{\mu_i}{T} \right) - \left(\frac{v_i}{v_k} \right) \nabla \left(\frac{\mu_k}{T} \right) = 0, \qquad i = \{1, ..., N\} \setminus \{k\}. \tag{2.139}$$

This set of equations may be solved, in combination with $\sum_i S_{T,i} x_i (1 - x_i) = 0$, following from the definition of the Soret coefficient. However, the observant reader will notice that the reference chemical potentials of the components do not cancel, leaving a result that will depend on the choice of reference state. This is the issue Kempers resolves with the 2001-approach.

2.4.2 The 2001-approach

In the 2001-approach,[15] the function subject to maximisation is instead the ratio of the partition function to the partition function in the ideal gas state. That is, the objective is to find

$$\max_{n_i^\alpha, n_i^\beta, n_i^{\alpha,ig}, n_i^{\beta,ig}} \left\{ \frac{Q}{Q^{ig}} \right\} = \max_{n_i^\alpha, n_i^\beta, n_i^{\alpha,ig}, n_i^{\beta,ig}} \left\{ \frac{Q^\alpha Q^\beta}{Q^{\alpha,ig} Q^{\beta,ig}} \right\} \tag{2.140}$$

The constraints are expanded to include $n_i^{\alpha,ig} + n_i^{\beta,ig} = n_i$, where the superscript ig indicates the ideal gas state. That is, the particle numbers in the ideal gas state are treated as independent variables, with the constraint that the total number of particles in

the ideal gas state must equal that in the real state. Kempers does not use the constraint that $\sum_i v_i^{\alpha,ig} n_i^{\alpha,ig} = \sum_i v_i^{\beta,ig} n_i^{\beta,ig} = \frac{V}{2}$. The resulting optimisation problem is

$$\begin{aligned} \min_{n_i^\alpha, n_i^\beta, n_i^{\alpha,ig}, n_i^{\beta,ig}} & \left\{ \frac{A^\alpha - A^{\alpha,ig}}{T^\alpha} + \frac{A^\beta - A^{\beta,ig}}{T^\beta} \right\} \\ n_i^\alpha + n_i^\beta &= n_i \\ n_i^{\alpha,ig} + n_i^{\beta,ig} &= n_i \\ \sum_i v_i^\alpha n_i^\alpha &= \sum_i v_i^\beta n_i^\beta \end{aligned} \tag{2.141}$$

Because the mole numbers in the ideal gas state and the real state are treated as independent variables, and the Helmholtz energy in each state is only a function of the mole numbers in that state (i.e. $A^\alpha = A^\alpha(\mathbf{n}^\alpha, T^\alpha, V^\alpha)$, $A^{\alpha,ig} = A^{\alpha,ig}(\mathbf{n}^{\alpha,ig}, T^\alpha, V^\alpha)$ etc.), this is exactly equivalent to conducting the two independent optimisations

$$\min_{n_i^\alpha, n_i^\beta} \left\{ \frac{A^\alpha}{T^\alpha} + \frac{A^\beta}{T^\beta} \right\} \qquad \min_{n_i^{\alpha,ig}, n_i^{\beta,ig}} \left\{ -\frac{A^{\alpha,ig}}{T^\alpha} - \frac{A^{\beta,ig}}{T^\beta} \right\} \tag{2.142}$$

$$n_i^\alpha + n_i^\beta = n_i \qquad n_i^{\alpha,ig} + n_i^{\beta,ig} = n_i \tag{2.143}$$

$$\sum_i v_i^\alpha n_i^\alpha = \sum_i v_i^\beta n_i^\beta \tag{2.144}$$

$$\tag{2.145}$$

The leftmost minimisation is equivalent to the problem in Equation (2.132), resulting in the set of Equations (2.139). The rightmost minimisation yields the Lagrange target-function

$$\mathcal{L}\left(\mathbf{n}^\alpha, \mathbf{n}^\beta, \phi\right) = -\frac{A^{\alpha,ig}}{T^\alpha} - \frac{A^{\beta,ig}}{T^\beta} - \sum_i \phi_i (n_i^{\alpha,ig} + n_i^{\beta,ig} - n_i). \tag{2.146}$$

Differentiation with respect to the target variables yields the set of equations

$$\begin{aligned} -\frac{\mu_i^{\alpha,ig}}{T^\alpha} - \phi_i &= 0 \\ -\frac{\mu_i^{\beta,ig}}{T^\beta} - \phi_i &= 0 \end{aligned} \tag{2.147}$$

Subtracting the first equation from the second yields the set of equations

$$\underset{\alpha,\beta}{\Delta} \left(\frac{\mu_i^{ig}}{T} \right) = 0. \tag{2.148}$$

As before, dividing by the length of the tube Δz, and taking the limit $\Delta z \to 0$, $\underset{\alpha,\beta}{\Delta} T \to 0$ then gives

$$\nabla \left(\frac{\mu_i^{ig}}{T} \right) = 0. \tag{2.149}$$

To arrive at the set of equations proposed by Kempers in 2001, first subtract Equation (2.149) for $i \neq k$ from equation (2.139), arriving at

$$\begin{aligned} \nabla\left(\frac{\mu_i}{T}\right) - \nabla\left(\frac{\mu_i^{ig}}{T}\right) - \left(\frac{v_i}{v_k}\right)\nabla\left(\frac{\mu_k}{T}\right) = 0, \qquad i = \{1,...,N\} \setminus \{k\} \\ \underset{ig}{\Delta}\left\{\nabla\left(\frac{\mu_i}{T}\right)\right\} - \left(\frac{v_i}{v_k}\right)\nabla\left(\frac{\mu_k}{T}\right) = 0 \end{aligned} \tag{2.150}$$

where $\underset{ig}{\Delta}\varphi \equiv \varphi - \varphi^{ig}$ denotes the difference between the real state and the ideal gas state. Finally, multiply Equation (2.149) for $i = k$ with $\frac{v_i}{v_k}$ and add the result to Equation (2.150), getting

$$\underset{ig}{\Delta}\left\{\nabla\left(\frac{\mu_i}{T}\right)\right\} - \left(\frac{v_i}{v_k}\right)\underset{ig}{\Delta}\left\{\nabla\left(\frac{\mu_k}{T}\right)\right\} = 0. \tag{2.151}$$

To solve this equation for the Soret coefficient, begin by expanding the gradients

$$\begin{aligned} \nabla\left(\frac{\mu_i}{T}\right) &= \left(\frac{\partial}{\partial T}\frac{\mu_i}{T}\right)_{p,x}\nabla T + \sum_j \left(\frac{\partial}{\partial x_j}\frac{\mu_i}{T}\right)_{T,p}\nabla x_j \\ &= -\frac{h_i}{T^2}\nabla T + \frac{1}{T}\sum_j \left(\frac{\partial \mu_i}{\partial x_j}\right)_{T,p}\nabla x_j, \end{aligned} \tag{2.152}$$

where the relationship

$$\begin{aligned} \mathrm{d}H &= T\mathrm{d}S + V\mathrm{d}p + \sum_j \mu_j \mathrm{d}n_j \\ \left(\frac{\partial H}{\partial n_i}\right)_{T,p} \equiv h_i &= T\left(\frac{\partial S}{\partial n_i}\right)_{T,p} + \mu_i \\ &= -T\left(\frac{\partial \mu_i}{\partial T}\right)_{\mathbf{n},p} + \mu_i \\ &= -T^2\left(\frac{\partial\left(\frac{\mu_i}{T}\right)}{\partial T}\right)_{\mathbf{n},p} \end{aligned} \tag{2.153}$$

has been used, with h_i denoting the partial molar enthalpy. Insert this expression into Equation (2.151) and divide through by ∇T to obtain a set of $N-1$ equations for the Soret coefficients,

$$\begin{aligned} \underset{ig}{\Delta}\left\{-\frac{h_i}{T^2} - \frac{1}{T}\sum_j\left(\frac{\partial \mu_i}{\partial x_j}\right)x_j(1-x_j)S_{T,j}\right\} \\ - \frac{v_i}{v_k}\underset{ig}{\Delta}\left\{-\frac{h_k}{T^2} - \frac{1}{T}\sum_j\left(\frac{\partial \mu_k}{\partial x_j}\right)x_j(1-x_j)S_{T,j}\right\} = 0. \end{aligned} \tag{2.154}$$

Given that the optimisation of the target function in Equation (2.146) does in fact yield the bulb compositions in the ideal gas steady state, and that kinetic gas theory can

accurately supply the Soret coefficients in the ideal gas state, this final set of equations can be solved for the Soret coefficients in the real state. This set of equations is termed the Kempers CoV model, due to the constraint of no volume translation. It can be shown that this is equivalent to the constraint of no pressure gradient.[19]

If, instead of imposing the constraint of no volume translation, one constrains the system such that the centre-of-mass is stationary i.e.

$$\sum_i n_i^\alpha m_i = \sum_i n_i^\beta m_i, \tag{2.155}$$

where m_i are the molar masses, the only change to the resulting equation will be swapping out the partial molar volumes with the molar masses. This result is termed the Kempers centre-of-mass (CoM) model.

3 Methods

The previously presented models and derivations have been implemented in a combination of C++ and Python. Numerical procedures are implemented in a C++ module with a Python interface, a Python wrapper was implemented to facilitate ease of use. This section explains and summarises the relevant numerical methods and implementation specific equations used in this work.

First, the numerical methods required to evaluate the integrals of Section 2.3.9 are covered. Later, in Sections 3.3 and 3.2, the Equations required for a closer analysis of the Kempers model and the assumptions behind it are presented.

3.1 Numerical methods

Before we begin, the goal of the Section is clearly stated: We wish to evaluate the double integral

$$W_{\ell,r} = 2\int_0^\infty \int_0^\infty \exp\left(-g^2\right) g^{2r+3} \left[1 - \cos^\ell\left(\chi\left(g,b\right)\right)\right] \left(\frac{b}{\sigma}\right) \mathrm{d}\left(\frac{b}{\sigma}\right) \mathrm{d}g \tag{3.1}$$

numerically. To do so, we must evaluate the deflection angle $\chi(g, b; T)$, which is computed as $\chi(g, b; T) = \pi - \theta(R; g, b, T)$, where

$$\theta(R; g, b, T) = \int_R^\infty \left(\frac{r^4}{b^2}\left[1 - \frac{u_{12}(r)}{k_B T g^2}\right] - r^2\right)^{-\frac{1}{2}} \mathrm{d}r. \tag{3.2}$$

The lower limit of integration, R, is the distance of closest approach, obtained by solving the Equation

$$\frac{R^4}{b^2}\left[1 - \frac{u_{12}(R)}{k_B T g^2}\right] - R^2 = 0. \tag{3.3}$$

The complete method therefore consists of several discrete parts: A root solver to determine R; a numerical integration scheme to determine $\theta(R; g, b, T)$, and thereby $\chi(g, b; T)$; and finally a 2d numerical integration scheme to evaluate $W_{\ell,r}$. Note that the temperature, T, is treated as a parametric dependency, meaning that $W_{\ell,r}$ must be computed at a given temperature.

These functions and equations are to a certain degree badly behaved, and applying commonly known integration schemes and root solvers was not directly successful. A part of the problem lies in the fact that the behaviour of $\frac{\mathrm{d}\theta}{\mathrm{d}r}(r; g, b, T)$ and Equation (3.3), which must be solved to obtain a value for R, depend upon the molecular parameters, as well as having a parametric dependency on g, b and T. Therefore robust algorithms for solving Equation (3.3) and evaluating the integral of Equation (3.2), which is required to obtain a value for χ, that are reliable for a large set of parameters are required. Further, the integrand of Equation (3.1), the dimensionless collision integral, is costly to evaluate and badly behaved. This section describes the integration and root solving algorithms implemented to handle these issues.

3.1.1 Solving for R

When implementing Newtons method to solve Equation (3.3) it is desirable to express the equation in such a way that the left hand side is either strictly increasing or decreasing in a wide region around the root. This makes the method less dependent upon a good initial guess, which is hard to obtain as the root is a function of the parameters g and b, as well as the temperature. Analysing the Equation, one finds that this can be achieved by dividing by $\frac{R^4}{b^2}$ to obtain

$$\psi_R(R; g, b, T) \equiv 1 - \frac{u_{12}(R)}{k_B T g^2} - \left(\frac{b}{R}\right)^2 = 0 \tag{3.4}$$

Where ψ_R is only a placeholder to refer to the function whose root determines R. Differentiation of ψ_R with respect to R yields

$$\psi'_R(R; g, b, T) = -\frac{u'_{12}(R)}{k_B T g^2} + \frac{2b^2}{R^3}. \tag{3.5}$$

For $b >> \sigma_{12}$, there will be very little interaction between the particles, except for at very small Tg ($Tg < 150$). Therefore b is used as an initial guess. However, note that due to the attractive part of the interaction potential, ψ_R may have a local minima at $r < b$, with the root residing at a yet lower value of r. This would result in the Newton iteration continuing to infinity. Therefore, the implemented algorithm checks the second derivative of ψ_R in each step, if the second derivative is negative, the iteration is restarted after reducing the initial guess by a factor of 0.1. This was tested and found to be a robust and efficient method of finding the root of Equation (3.4).

3.1.2 Evaluating θ

It is immediately clear that the integrand of Equation (3.2) is divergent at $r = R$, as this is implied by the solution of equation (3.3). Further, as shown in Figure 3.1, the integrand decreases rapidly at first, but does not converge very quickly. The algorithm used to evaluate the integral implements a trapezoidal integration rule, denoting $\psi_\theta(r; g, b, T) \equiv \frac{\mathrm{d}\theta}{\mathrm{d}r}$,

$$I[r_a, r_b] = \sum_i \frac{\psi_\theta(r_i) + \psi_\theta(r_{i+1})}{2} \Delta r_i \approx \int_{r_a}^{r_b} \psi_\theta \mathrm{d}r. \tag{3.6}$$

Where $I[r_a, r_b]$ denotes the numerical approximation to the integral on the interval from r_a to r_b. This integration rule was chosen as it both gives solid control of the integration error and is fairly simple to implement. Due to the large second derivative of ψ_θ with respect to r when $|r - R| \approx 0$, high resolution is required at small r. However, how high the resolution must be varies greatly with the parameters g, b and T. Therefore it was made use of the fact that for the trapezoidal integration scheme

$$\epsilon_{abs} = \left| I[r_a, r_b] - \int_{r_a}^{r_b} \psi_\theta \mathrm{d}r \right| \leq \frac{\max\limits_{(r_a, r_b)} \{|\psi''_\theta(r)|\} (r_b - r_a)^3}{12N^2} \tag{3.7}$$

where ϵ_{abs} denotes the absolute error in the integral, $\max\limits_{(r_a, r_b)} \{|\psi''_\theta(r)|\}$ denotes the maximum absolute value of the second derivative of the integrand on the interval (r_a, r_b), and N

denotes the number of intervals. Utilising this, a tolerance, ϵ_{tol}^{step}, may be selected for each interval, and the length of that interval can be determined as

$$\Delta r_i = \left(\frac{12\epsilon_{tol}^{step}}{\max\limits_{(r_i,\, r_i+\Delta r_i)} \{|\psi_\theta''(r)|\}} \right)^{\frac{1}{3}} \tag{3.8}$$

ensuring that the error over a single integration step never exceeds ϵ_{tol}^{step}. The second derivative of the integrand of Equation (3.2), i.e. $\frac{\mathrm{d}^3\theta}{\mathrm{d}r^3}$ is obtained by straight forward differentiation as

$$\begin{aligned}
\psi_\theta''(r) &= \frac{3}{4}\varphi^{-\frac{5}{2}}\varphi'(r) - \frac{1}{2}\varphi^{-\frac{3}{2}}\varphi''(r) \\
\varphi &= \frac{r^4}{b^2}\left(1 - \frac{u_{12}(r)}{k_B T g}\right) - r^2 \\
\varphi'(r) &= \frac{4r^3}{b^2}\left(1 - \frac{u_{12}(r)}{k_B T g}\right) + \frac{r^4}{b^2}\frac{u_{12}'(r)}{k_B T g} - 2r \\
\varphi''(r) &= \frac{12r^2}{b^2}\left(1 - \frac{u_{12}(r)}{k_B T g}\right) + \frac{8r^3}{b^2}\frac{u_{12}'(r)}{k_B T g} + \frac{r^4}{b^2}\frac{u_{12}''(r)}{k_B T g} - 2
\end{aligned} \tag{3.9}$$

Noting that the second derivative is strictly decreasing in the most critical region (at small r), the step length is computed as

$$\Delta r_i = \left(\frac{12\epsilon_{tol}^{step}}{|\psi_\theta''(r_a)|} \right)^{\frac{1}{3}}. \tag{3.10}$$

To assess whether the integral has converged at a given point, the integration algorithm moves forward iteratively. In the first iteration, 100 integration steps are conducted, as this was found to be slightly less that what was most often required to achieve convergence. In the following iterations, the value of the integral is stored and $N_{0.1}$ integration steps are conducted, where $N_{0.1} = \frac{N_t}{9}$ and N_t is the total number of integration steps that have been conducted in previous iterations. This means that if N_i denotes the total number of integration steps conducted after iteration i, $N_1 = 0.9N_2 = (0.9)^2 N_3 = ... = (0.9)^{i-1}N_i$. The algorithm terminates when the change in the integral after an iteration is less than a set tolerance, ϵ_{conv}. The integration is illustrated in Figure 3.1.

After termination, the relative error of the total integral is checked, and if exceeding a tolerance ϵ_{tol}^{tot}, the step error tolerance ϵ_{tol}^{step} is reduced, and the integral is recomputed.

3.1.3 Evaluating $W_{\ell,r}$

The integrand of Equation (3.1) is expensive to evaluate, and as shown in Figure 3.2 high resolution is required in certain regions to achieve satisfactory precision due to large first and second derivatives. It is unfeasible to conduct the integration with this high resolution over a region large enough to ensure that the integral has converged, without a higher capacity for parallelization than what was possible with the tools available during this work. Additionally, the shape of the integrand varies with the parameters ℓ, r and T as well as the molecular parameters. The evaluation of a single diffusion coefficient,

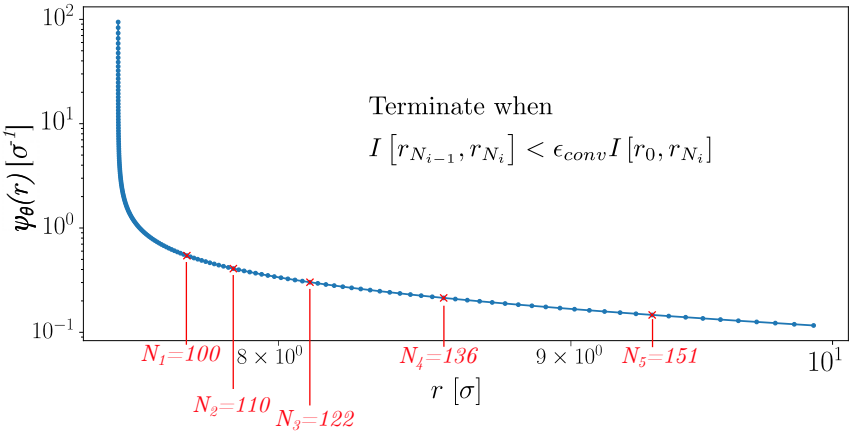

Figure 3.1: Illustration of the need for high refinement of the integral of Equation (3.2), and the manner in which convergence is determined.

at a given temperature, to the first Enskog approximation, requires that the integral of Equation (3.1) is evaluated nine times for different combinations of ℓ, r, and the number increases rapidly with increasing order of approximation. This makes it unfeasible to manually consider each integral. The implementation developed in this work is written to utilise two processor cores, with the option of using up to eight, to simultaneously evaluate several integrals. Additionally, a solution for storing the value of evaluated integrals for later use was implemented.

To achieve reliable and efficient evaluation of the dimensionless collision integral an adaptive meshing algorithm was developed and implemented. This was used in combination with a planar linear interpolation scheme.

Planar linear interpolation

Given a set of three points, $P = \{p_1, p_2, p_3\} \subset \mathbb{R}^3$, denote the corresponding set of points in the (x, y)-plane as $\tilde{P} = \{\tilde{p}_1, \tilde{p}_2, \tilde{p}_3\} \subset \mathbb{R}^2$. A plane can be constructed to interpolate the integrand in P, express this interpolating plane as

$$z(x, y) = Ax + By + C \tag{3.11}$$

Further, ensure $x_1 \leq x_2 \leq x_3$, by reordering the points if necessary. Now, determine the functional form of the lines connecting each pair of points in $\tilde{P}$, denoted l_{ij} for the line passing through $(\tilde{p}_i, \tilde{p}_j)$. These have the form

$$l_{ij} = A_{ij}^{(l)} x + B_{ij}^{(l)}, \quad A_{ij}^{(l)} = \frac{y_j - y_i}{x_j - x_i}, \quad B_{ij}^{(l)} = y_j - A_{ij}^{(l)} x_j \tag{3.12}$$

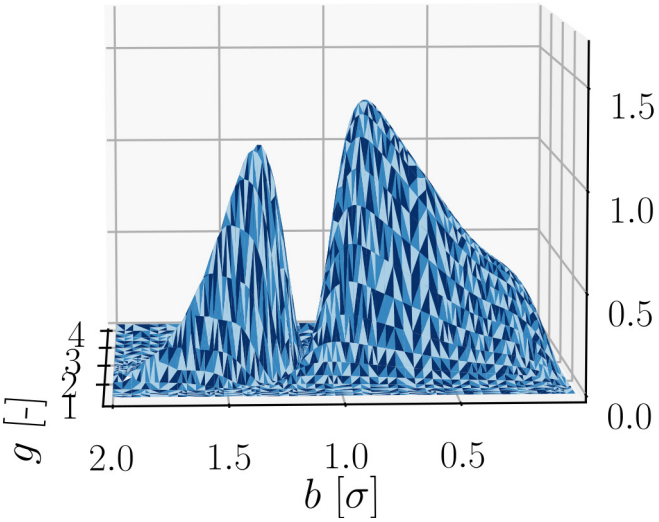

Figure 3.2: Illustrative example of the form of the integrand of Equation (3.1). Interpolating the integrand in such a manner that one captures the "valley" between the peaks is non-trivial, as the form of said valley is dependent on the potential parameters and the temperature, as well as the parameters r and ℓ. The function has been triangulated by the adaptive meshing scheme described in Section 3.1.3, with exaggerated refinement to clearly illustrate the form of the function. Note that the surface consists of triangles, areas that look like parallelograms consist of two bordering triangles with the same colour.

The integral of the interpolating plane may now be written as

$$I[p_1, p_2, p_3] = \int_{x_1}^{x_2} \int_{l_{12}}^{l_{13}} z(x, y) \mathrm{d}y \mathrm{d}x + \int_{x_2}^{x_3} \int_{l_{12}}^{l_{23}} z(x, y) \mathrm{d}y \mathrm{d}x, \quad y_2 < y_3 \vee (y_2 = y_3 \wedge y_2 > y1) \tag{3.13}$$

$$I[p_1, p_2, p_3] = \int_{x_1}^{x_2} \int_{l_{13}}^{l_{12}} z(x, y) \mathrm{d}y \mathrm{d}x + \int_{x_2}^{x_3} \int_{l_{13}}^{l_{23}} z(x, y) \mathrm{d}y \mathrm{d}x, \quad y_2 > y_3 \vee (y_2 = y_3 \wedge y_2 < y1) \tag{3.14}$$

Only the first term of the first case is treated explicitly here, the remaining terms are obtained by appropriate index-swapping.

$$\begin{aligned} \int_{x_1}^{x_2} \int_{l_{12}}^{l_{13}} z(x, y) \mathrm{d}y \mathrm{d}x &= \int_{x_1}^{x_2} \left[(Ax + C)\, y + \frac{B}{2} y^2 \right]_{l_{12}}^{l_{13}} \mathrm{d}x \\ &= \int_{x_1}^{x_2} (Ax + C) \left(\left(A_{13}^{(l)} - A_{12}^{(l)} \right) x + B_{13}^{(l)} - B_{12}^{(l)} \right) \\ &\qquad + \frac{B}{2} \left[\left(A_{13}^{(l)} x + B_{13}^{(l)} \right)^2 - \left(A_{12}^{(l)} x + B_{12}^{(l)} \right)^2 \right] \mathrm{d}x \\ &\equiv \int_{x_1}^{x_2} \tilde{A}_{12}^{(13)} x^2 + \tilde{B}_{12}^{(13)} x + \tilde{C}_{12}^{(13)} \mathrm{d}x \end{aligned} \tag{3.15}$$

where

$$\begin{aligned}
\tilde{A}_{12}^{(13)} &= A\left(A_{13}^{(l)} - A_{12}^{(l)}\right) + \frac{B}{2}\left[\left(A_{13}^{(l)}\right)^2 - \left(A_{12}^{(l)}\right)^2\right] \\
\tilde{B}_{12}^{(13)} &= A\left(B_{13}^{(l)} - B_{12}^{(l)}\right) + B\left(A_{13}^{(l)}B_{13}^{(l)} - A_{12}^{(l)}B_{12}^{(l)}\right) + C\left(A_{13}^{(l)} - A_{12}^{(l)}\right) \\
\tilde{C}_{12}^{(13)} &= \frac{B}{2}\left[\left(B_{13}^{(l)}\right)^2 - \left(B_{12}^{(l)}\right)^2\right] + C\left(B_{13}^{(l)} - B_{12}^{(l)}\right)
\end{aligned} \tag{3.16}$$

The integral in question is then

$$\int_{x_1}^{x_2}\int_{l_{12}}^{l_{13}} z(x,y)\mathrm{d}y\mathrm{d}x = \frac{\tilde{A}_{12}^{(13)}}{3}\left(x_2^3 - x_1^3\right) + \frac{\tilde{B}_{12}^{(13)}}{2}\left(x_2^2 - x_1^2\right) + \tilde{C}_{12}^{(13)}\left(x_2 - x_1\right). \tag{3.17}$$

Adaptive meshing

The implemented integration scheme is exact for any function $\psi(x,y)$ that satisfies $\left(\frac{\partial^2\psi}{\partial x^2}\right) = \left(\frac{\partial^2\psi}{\partial x\partial y}\right) = \left(\frac{\partial^2\psi}{\partial y^2}\right) = 0$ over the entire integration domain. It is assumed that, similarly to the analogous one-dimensional trapezoid scheme, the error in the two dimensional scheme scales linearly with the second derivative, and is proportional to the cube of the step length. That is, the absolute integration error in each subinterval $(x, x+h_x)\times(y, y+h_y)$ is assumed to be of the form

$$\left|\epsilon_i^{abs.}\right| \sim \left|\left(\frac{\partial^2 f}{\partial x^2}\right)h_x^3\right| + \left|\left(\frac{\partial^2 f}{\partial y^2}\right)h_y^3\right| + \left|\left(\frac{\partial^2 f}{\partial x\partial y}\right)(h_x+h_y)^3\right| \tag{3.18}$$

The following meshing algorithm increases the mesh resolution in regions with high second derivatives to ensure precise integration. At the same time, large step sizes are permitted in regions with small second derivatives to prevent unnecessary function evaluations from making the integration unnecessarily computationally intensive.

Let $\mathcal{S} = \{(x_0, x_0+\Delta x)\times(y_0, y_0+\Delta y)\}$ be the total domain of integration. Further, let

$$\begin{aligned}
\mathcal{S}^* &= \left\{\left(x_i^{\mathcal{S}^*}, y_i^{\mathcal{S}^*}, h_x^{\mathcal{S}^*}, h_y^{\mathcal{S}^*}\right) \mid \left(x_i^{\mathcal{S}^*}, y_i^{\mathcal{S}^*}\right) \subseteq \mathcal{S} \ \wedge\ h_x^{\mathcal{S}^*} = x_{i+1}^{\mathcal{S}^*} - x_i^{\mathcal{S}^*},\ h_y^{\mathcal{S}^*} = y_{j+1}^{\mathcal{S}^*} - y_j^{\mathcal{S}^*}\right\} \\
\mathcal{S}_{ij}^*\left(\mathcal{S}^*\right) &= \left\{(x,y) \ \in\ \left(x_i^{\mathcal{S}^*}, x_i^{\mathcal{S}^*} + h_x^{\mathcal{S}^*}\right)\times\left(y_j^{\mathcal{S}^*}, y_j^{\mathcal{S}^*} + h_y^{\mathcal{S}^*}\right)\right\} \\
\mathcal{S}_{ij}^{\Delta}(h_x', h_y', \mathcal{S}^*) &= \left\{\left(x_{i'}, y_{j'}\right) \subset \mathcal{S}_{ij}^*\left(\mathcal{S}^*\right) \mid x_{i'+1} - x_{i'} = h_x' \ \wedge\ y_{j'+1} - y_{j'} = h_y'\right\}
\end{aligned} \tag{3.19}$$

Such that $\mathcal{S}^*$ is some discrete subset of $\mathcal{S}$, $\mathcal{S}_{ij}^*$ is a continuous subset of $\mathcal{S}$, bounded by

$\mathcal{S}^*$, and $\mathcal{S}_{ij}^{\Delta}$ is a discrete subset of $\mathcal{S}_{ij}^*$. The mappings

$$\mathcal{S}_{ij}^{x}\left(\mathcal{S}^*\right) \;:\; \mathcal{S}^* \mapsto \left\{ (x_k, y_\ell, h'_x, h'_y) \mid (x_k, y_\ell) \in \; \mathcal{S}_{ij}^{\Delta}(h'_x, h'_y, \mathcal{S}^*) \;:\; h'_x = \frac{h_x^{\mathcal{S}^*}}{2},\; h'_y = h_y^{\mathcal{S}^*} \right\} \tag{3.20}$$

$$\mathcal{S}_{ij}^{y}\left(\mathcal{S}^*\right) \;:\; \mathcal{S}^* \mapsto \left\{ (x_k, y_\ell, h'_x, h'_y) \mid (x_k, y_\ell) \in \; \mathcal{S}_{ij}^{\Delta}(h'_x, h'_y, \mathcal{S}^*) \;:\; h'_x = h_x^{\mathcal{S}^*},\; h'_y = \frac{h_y^{\mathcal{S}^*}}{2} \right\} \tag{3.21}$$

$$\mathcal{S}_{ij}^{xy}\left(\mathcal{S}^*\right) \;:\; \mathcal{S}^* \mapsto \left\{ (x_k, y_\ell, h'_x, h'_y) \mid (x_k, y_\ell) \in \; \mathcal{S}_{ij}^{\Delta}(h'_x, h'_y, \mathcal{S}^*) \;:\; h'_x = \frac{h_x^{\mathcal{S}^*}}{2},\; h'_y = \frac{h_y^{\mathcal{S}^*}}{2} \right\} \tag{3.22}$$

may then be used to recursively generate discrete subsets of $\mathcal{S}$ with increased resolution in each iteration, the domains and mappings are illustrated in Figure 3.3.

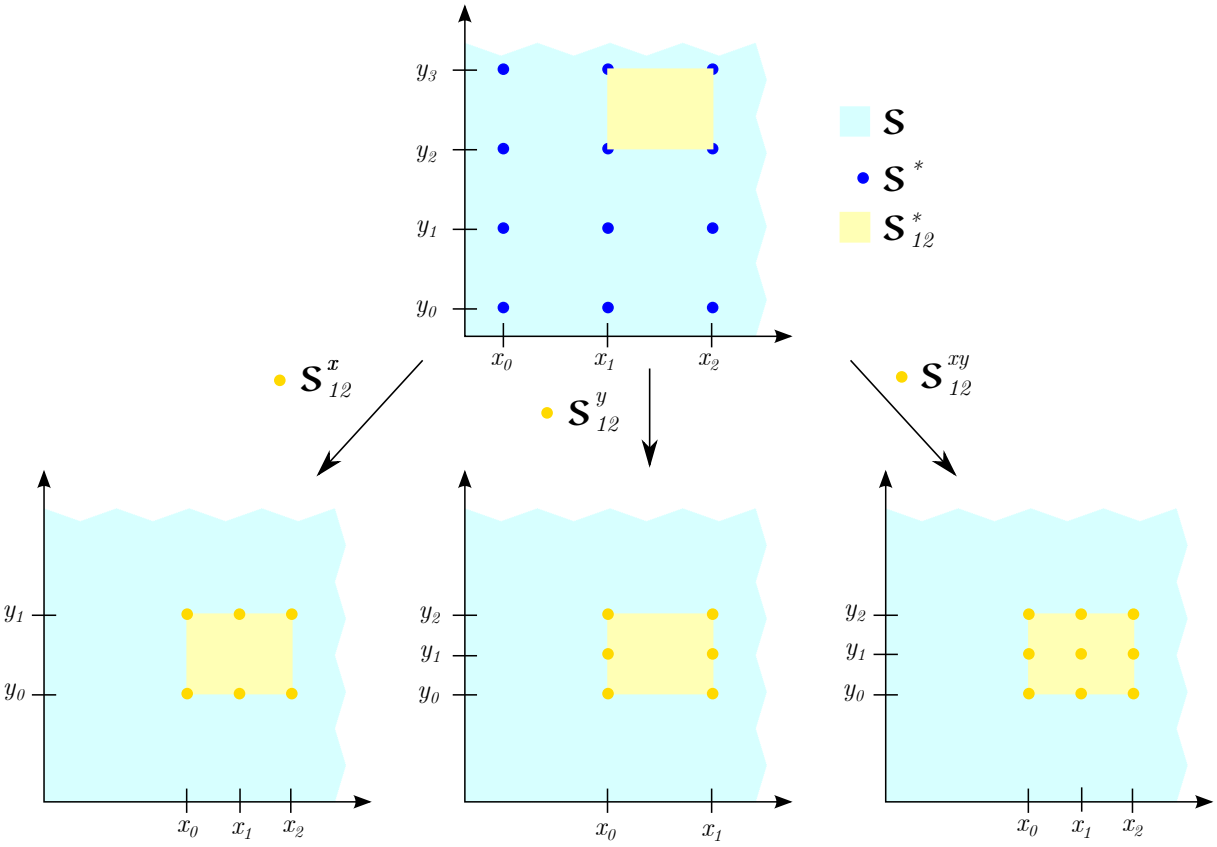

Figure 3.3: Domains and mappings of Equations (3.19)-(3.22), used to recursively refine the mesh used to interpolate the integrand of Equation (3.1).

To integrate a function $\psi(x, y)$ over $\mathcal{S}$, the integration algorithm starts with a large step size in each direction, denoted $h_x = N_x \delta x$ and $h_y = N_y \delta y$, where $(N_x, N_y) = \{(2^{n_x}, 2^{n_y}) : (n_x, n_y) \in \mathbb{N}^2\}$ and $\delta x, \delta y$ denote the minimum step size (i.e. maximum re-

finement) in each direction. The numerical second derivatives of ψ are computed as

$$\begin{aligned}
\left(\frac{\partial^2\psi}{\partial x^2}\right) &\approx \left(\Delta_x^2\psi\right)_{i,j} \equiv \frac{\psi_{i,j} - 2\psi_{i+1,j} + \psi_{i+2,j}}{(h_x)^2} \\
\left(\frac{\partial^2\psi}{\partial y^2}\right) &\approx \left(\Delta_y^2\psi\right)_{i,j} \equiv \frac{\psi_{i,j} - 2\psi_{i,j+1} + \psi_{i,j+2}}{(h_y)^2} \\
\left(\frac{\partial^2\psi}{\partial x\partial y}\right) &\approx \left(\Delta_{xy}^2\psi\right)_{i,j} \equiv \frac{\psi_{i,j} - 2\psi_{i+1,j+1} + \psi_{i+2,j+2} - h_x^2\Delta_x^2\psi - h_y^2\Delta_y^2\psi}{2h_xh_y}
\end{aligned} \tag{3.23}$$

where $\psi_{k,l} = \psi(x_0 + kh_x, y_0 + lh_y)$ and the equivalencies define the $\Delta_x^2\psi$, $\Delta_y^2\psi$ and $\Delta_{xy}^2\psi$ - finite difference operators. Once the numerical second derivatives are computed, the conditions of Equations (3.24)-(3.28) are checked successively.

$$\text{(I)} \quad \left|\left(\Delta_x^2 z\right)_{i,j}\right| > \epsilon \;\wedge\; \left|\left(\Delta_y^2 z\right)_{i,j}\right| < \epsilon \;\wedge\; \left|\left(\Delta_{xy}^2 z\right)_{i,j}\right| < \epsilon \;\wedge\; N_x > 1, \tag{3.24}$$

$$\text{(II)} \quad \left|\left(\Delta_x^2 z\right)_{i,j}\right| < \epsilon \;\wedge\; \left|\left(\Delta_y^2 z\right)_{i,j}\right| > \epsilon \;\wedge\; \left|\left(\Delta_{xy}^2 z\right)_{i,j}\right| < \epsilon \;\wedge\; N_y > 1, \tag{3.25}$$

$$\text{(III)} \quad \left|\left(\Delta_x^2 z\right)_{i,j}\right| + \left|\left(\Delta_y^2 z\right)_{i,j}\right| + \left|\left(\Delta_{xy}^2 z\right)_{i,j}\right| > \epsilon \;\wedge\; N_x > 1 \;\wedge\; N_y > 1, \tag{3.26}$$

$$\text{(IV)} \quad \left|\left(\Delta_x^2 z\right)_{i,j}\right| + \left|\left(\Delta_y^2 z\right)_{i,j}\right| + \left|\left(\Delta_{xy}^2 z\right)_{i,j}\right| > \epsilon \;\wedge\; N_x > 1, \tag{3.27}$$

$$\text{(V)} \quad \left|\left(\Delta_x^2 z\right)_{i,j}\right| + \left|\left(\Delta_y^2 z\right)_{i,j}\right| + \left|\left(\Delta_{xy}^2 z\right)_{i,j}\right| > \epsilon \;\wedge\; N_y > 1, \tag{3.28}$$

Here, ϵ is some predetermined tolerance value. Upon reaching a condition that is true, the algorithm selects a map, following the rules

$$\text{(I)} \;\vee\; \text{(IV)} \mapsto \mathcal{S}_{ij}^x, \qquad \text{(II)} \;\vee\; \text{(V)} \mapsto \mathcal{S}_{ij}^y, \qquad \text{(III)} \mapsto \mathcal{S}_{ij}^{xy},$$

to generate a subdomain and calls itself recursively on that subdomain.

If no condition is true, the algorithm steps across the current domain, following the pattern $p_0 = (x_0, y_0)$, $p_1 = (x_0, y_1)$, $p_2 = (x_1, y_0)$, ..., $p_{2k} = (x_k, y_0)$, $p_{2k+1} = (x_k, y_1)$. Upon reaching the edge of the current domain, at $x_k = x_N$, two steps are conducted in the y-direction, and the step in the x-direction is reversed, such that the stepping follows the pattern $p_{N+2k} = (x_{N-k}, y_1)$, $p_{N+2k+1} = (x_{N-k}, y_2)$. The pattern is illustrated in Figure 3.4.

To verify the reliability of the implemented integration algorithm, several functions with analytic integrals were meshed and integrated numerically. As shown in Figure 3.5, the meshing algorithm successfully increased resolution in areas with large second derivatives. The resulting numeric integrals had errors of typically less than 3 %, even with large initial grid size. To minimise the number of function evaluations, the integrands' value in each gridpoint is stored, such that it will not be recomputed for each triangle that uses the point.

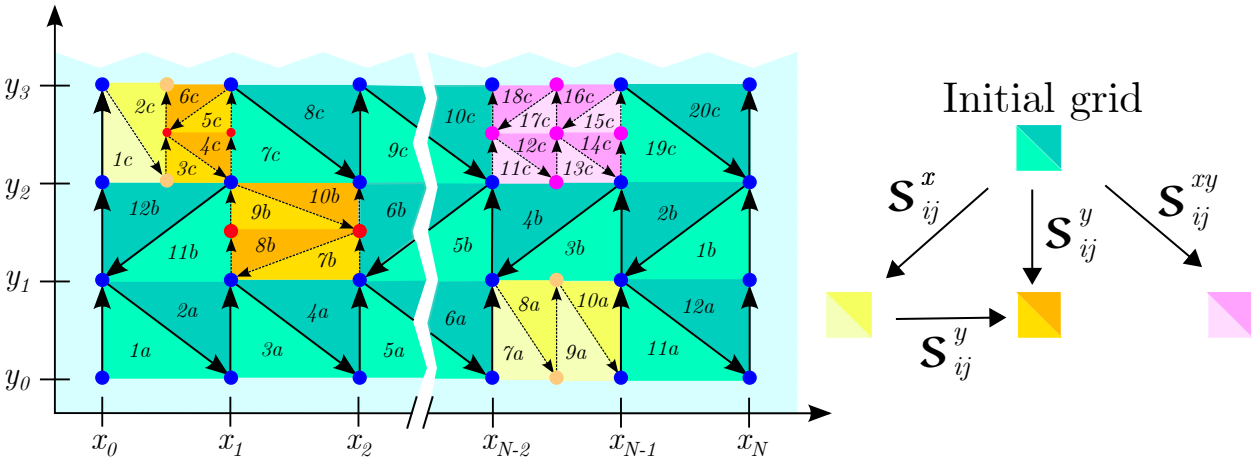

Figure 3.4: The stepping algorithm used to generate the recursively refined integration mesh. Arrows indicate integration steps, numbers indicate the order in which the interpolating triangles are generated, going in the order $1a-12a-1b-12b-1c-20c$. Refined regions are indicated, with yellow regions refined by the map $\mathcal{S}^x_{ij}$, orange regions refined by $\mathcal{S}^y_{ij}$ and purple regions refined by $\mathcal{S}^{xy}_{ij}$. The region $3c-6c$ is doubly refined, first by $\mathcal{S}^x_{ij}$, then by $\mathcal{S}^y_{ij}$.

Refining the algorithm parameters

From geometric considerations one will find that for a hard sphere

$$\chi^{HS} = \cos^{-1}\left[1-2\left(1-\left(\frac{b}{\sigma^{HS}_{ij}}\right)^2\right)\right]\times\begin{cases}1, & b<\sigma^{HS}_{ij}\\ 0, & b>\sigma^{HS}_{ij}\end{cases} \tag{3.29}$$

After testing the implemented algorithm for the functions shown in Figure 3.5, appropriate parameters required to precisely and efficiently evaluate the dimensionless collision integral were determined. This was done by using the pseudo-hard-sphere potential,

$$u_{p-HS}(r_{ij}) = \begin{cases}\left(\frac{\sigma_{ij}}{r_{ij}}\right)^{\varphi} + \frac{\varphi(\varphi+1)}{2}\left(\frac{r_{ij}}{\sigma_{ij}}\right)^2 - \varphi\left(\varphi-\frac{\varphi}{\sigma_{ij}}+1\right)r_{ij} & \\ \qquad +\varphi\left((\varphi+1)\sigma_{ij}-\frac{\varphi}{2}-\frac{3}{2}\right)-1 & r_{ij}<\sigma_{ij}\\ 0 & r_{ij}>\sigma_{ij}\end{cases} \tag{3.30}$$

to compute χ, R and $W_{\ell,r}$ numerically, and comparing the result to the known analytical solutions for hard spheres. This potential was chosen due to the root solver and integration scheme requiring continuous first and second derivatives to behave as intended, and the given potential satisfies

$$u_{p-HS}(\sigma) = u'_{p-HS}(\sigma) = u''_{p-HS}(\sigma) = 0. \tag{3.31}$$

An exponent of $\varphi = 20$ was chosen arbitrarily as a large exponent to force the potential to rise steeply. Using the integration parameters shown in Table 3.1, the integration error when compared to the analytic solutions for a hard sphere were consistently below 1 % for $\ell, r < 9$.

The entirety of the implementation developed in this work will be made available in a public repository on GitHub, and can be supplied upon request.[44]

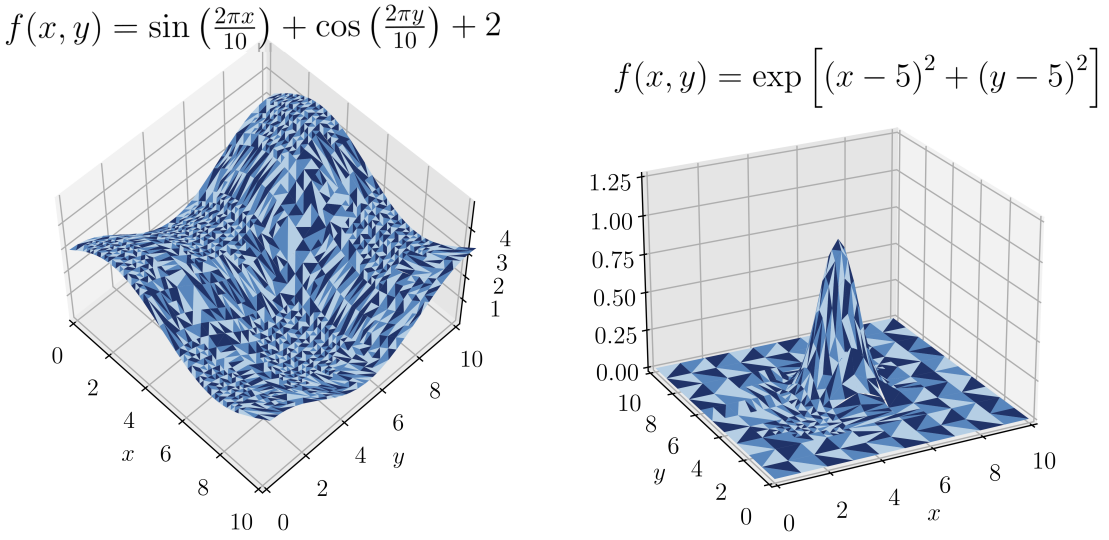

(a) $\epsilon_r = 0.38$ %

(b) $\epsilon_r = 0.48$ %

Figure 3.5: Visualisation of the triangulation of two test functions. $\epsilon_r = \frac{|I_{\text{exact}} - I_{\text{numeric}}|}{I_{\text{exact}}}$ is the relative error in the numeric integrals. In (a), notice the individual refinement in the x- and y- directions.

Table 3.1: Parameters used with the integration scheme presented in Section 3.1 throughout this work. ϵ_0 refers to the tolerance for refinement, used in Equations (3.24)-(3.28), δ is the minimum step size along each axis and N is the initial step size in multiples of δ. g_N and $\left(\frac{b}{\sigma}\right)_N$ are the cutoff values of the integration domain.

Parameter	Value	Parameter	value
N_g	4	$N_{\left(\frac{b}{\sigma}\right)}$	16
δ_g	0.5	$\delta_{\left(\frac{b}{\sigma}\right)}$	0.05
g_N	7.5	$\left(\frac{b}{\sigma}\right)_N$	5
ϵ_0	10^{-5}		

3.2 A modified Kempers approach

When one views the 2001-approach as two independent optimisations, it is not immediately clear why the real state is assumed to obey Equation (2.139), given as

$$\nabla\left(\frac{\mu_i}{T}\right) - \left(\frac{v_i}{v_k}\right)\nabla\left(\frac{\mu_k}{T}\right) = 0, \qquad i = \{1, ..., N\} \setminus \{k\}. \tag{3.32}$$

while the ideal gas state does not. Additionally, it has previously been noted that the Enskog solutions for hard spheres without density corrections do not represent an ideal gas, but an infinitely dilute mixture of hard spheres.[25] The difference between the two is discussed in more detail in Section 4.6. It has been proposed that one should therefore not use the ideal gas state as a reference, but rather a hard sphere state, which may be accurately described within the Boublík formalism.[45,46]

If, following Kempers, one assumes that all systems obey Equation (3.32) in the steady state, and that the Soret coefficient in an infinitely dilute mixture of hard spheres is accurately described by kinetic gas theory, one can set up Equation (3.32) for both the hard sphere state and the real state,

$$\begin{aligned} \nabla\left(\frac{\mu_i}{T}\right) - \frac{v_i}{v_k}\nabla\left(\frac{\mu_k}{T}\right) &= 0 \\ \nabla\left(\frac{\mu_i^{HS}}{T}\right) - \frac{v_i^{HS}}{v_k^{HS}}\nabla\left(\frac{\mu_k^{HS}}{T}\right) &= 0 \end{aligned} \tag{3.33}$$

Now, subtracting the two, as in the 2001-approach, and inserting the expansion of $\nabla\left(\frac{\mu_i}{T}\right)$ from Equation (2.152), one arrives at

$$\begin{aligned} \underset{HS}{\Delta}\left\{-\frac{h_i}{T^2} - \frac{1}{T}\sum_j\left(\frac{\partial\mu_i}{\partial x_j}\right)x_j(1-x_j)S_{T,j}\right\} \\ - \underset{HS}{\Delta}\left\{\frac{v_i}{v_k}\left(-\frac{h_k}{T^2} - \frac{1}{T}\sum_j\left(\frac{\partial\mu_k}{\partial x_j}\right)x_j(1-x_j)S_{T,j}\right)\right\} = 0, \end{aligned} \tag{3.34}$$

where $\underset{HS}{\Delta}\varphi \equiv \varphi - \varphi^{HS}$ indicates the difference between the real value and the hard sphere value for some variable φ. Together with the condition that $\sum_j x_j(1-x_j)S_{T,j} = 0$, and with $S_{T,i}^{HS}$ supplied from kinetic gas theory, this set of equations can be solved for the Soret coefficients in the real state.

All thermodynamic quantities required to solve this set of equations, with the exception of $\left(\frac{\partial\mu_i}{\partial x_j}\right)_{T,p}$, are directly available in the thermodynamic library ThermoPack.[32] A relationship allowing one to compute $\left(\frac{\partial\mu_i}{\partial x_j}\right)_{T,p}$ from quantities that are available is derived in Appendix C. The entirety of the implementation of the Kempers model can be found in a public repository on GitHub.[47]

3.3 Kempers: Evaluation of the steady state assumptions

To compare the predictions by the Kempers model to Kinetic gas theory, and investigate how the two relate to the Helmholtz energy of the two-bulb system, Kempers target function of minimisation,

$$\tau \equiv \frac{A^\alpha}{T^\alpha} + \frac{A^\beta}{T^\beta} \tag{3.35}$$

is computed for a two-container system with a small, finite temperature difference. The system average temperature is taken to be

$$T = \frac{T^\alpha + T^\beta}{2}. \tag{3.36}$$

Note that this choice is made for simplicity, using a mole-average temperature may be reasonable, but makes the mathematics of the problem far more involved. It is assumed that when dealing with temperature differences on the order of 0.1 K, the difference between the bulb average used here, and the mole average is negligible. The two bulb temperatures are related to the temperature difference, ΔT as

$$T^\alpha = T - \frac{1}{2}\Delta T, \qquad T^\beta = T + \frac{1}{2}\Delta T. \tag{3.37}$$

The bulbs are considered as two separate, closed volumes held at T^α and T^β, with a fixed total number of moles $\mathbf{n} = \mathbf{n}^\alpha + \mathbf{n}^\beta$. The volume of the two bulbs is held constant, and for simplicity is set to be equal. Given a distribution of component 1, $\Delta n_1 = n_1^\beta - n_1^\alpha$ and component 2, $\Delta n_2 = n_2^\beta - n_2^\alpha$, one can compute

$$n_1^\alpha = \frac{n_1 - \Delta n_1}{2}, \quad n_1^\beta = \frac{n_1 + \Delta n_1}{2}. \tag{3.38}$$

Such that instead of considering the four mole numbers, we may instead consider the two component separations. These will be our free variables. Given that we have two degrees of freedom, imposing any constraint on the system will uniquely define a curve in the $(\Delta n_1, \Delta n_2)$-plane. Thus, the consequence of constraining the minimisation of τ can be investigated. The first curve we consider is that of equal bulb mass, $\Delta m = 0$, given by

$$\begin{aligned} \Delta m = m_1 \Delta n_1 + m_2 \Delta n_2 = 0 \\ \Delta n_2 = -\frac{m_1}{m_2}\Delta n_1. \end{aligned} \tag{3.39}$$

According to the Kempers-CoM model, the steady state is the minima in τ along this curve. The second to consider is the curve corresponding to no pressure difference, $\Delta p = 0$. From the total differential of pressure at constant volume,

$$\begin{aligned} \mathrm{d}p = \left(\frac{\partial p}{\partial T}\right)_{\mathbf{n},V} \mathrm{d}T + \sum_i \left(\frac{\partial p}{\partial n_i}\right)_{T,V,n_k} \mathrm{d}n_i = 0 \\ \Delta n_2 \approx -\frac{\left(\frac{\partial p}{\partial T}\right)_{\mathbf{n},V} \Delta T + \left(\frac{\partial p}{\partial n_1}\right)_{T,V,n_2} \Delta n_1}{\left(\frac{\partial p}{\partial n_2}\right)_{T,V,n_1}}. \end{aligned} \tag{3.40}$$

The minima in τ along this curve is the steady state predicted by the Kempers-CoV model.

Finally, to investigate the steady state predicted by the Enskog solutions, we find the curve of fixed compositional difference $x_1^\beta - x_1^\alpha = \Delta x$, given by

$$\begin{aligned}
\Delta x_1 &= \frac{n_1^\beta}{n_1^\beta + n_2^\beta} - \frac{n_1^\alpha}{n_1^\alpha + n_2^\alpha} \\
&= \frac{n_1 + \Delta n_1}{n + \Delta n} - \frac{n_1 - \Delta n_1}{n - \Delta n} \\
\Delta x_1 \left(n^2 - (\Delta n)^2\right) &= (n_1 + \Delta n_1)(n - \Delta n) - (n_1 - \Delta n_1)(n + \Delta n) \\
&= 2\left(n\Delta n_1 - n_1 \Delta n\right) \\
-\Delta x_1 (\Delta n)^2 + 2n_1 \Delta n + \Delta x_1 n^2 - 2n\Delta n_1 &= 0.
\end{aligned} \tag{3.41}$$

Closer investigation reveals that only one of the roots of this equation will be a physical solution, the other will have $|\Delta n| > n$ or $|\Delta n_1| > n_1$.

In addition to computing these curves, it is of interest to investigate the steady state pressure gradient as predicted by the Enskog solutions. Recall Equation (2.55),

$$\bar{\mathbf{u}}_1 - \bar{\mathbf{u}}_2 = -\frac{1}{3}\rho \left[\{\mathbf{D}, \mathbf{D}\}\, \mathbf{d}_{12} + \{\mathbf{D}, \mathbf{\Lambda}\} \nabla \ln T\right]. \tag{3.42}$$

In the steady state, the left hand side vanishes. Expanding $\mathbf{d}_{12}$ and inserting the transport coefficients for the bracket integrals yields

$$\begin{aligned}
0 = -\frac{1}{3}\rho \left[\frac{3\rho}{\rho_1 \rho_2} D_{12} \left(\nabla x_1 + \frac{\rho_1 \rho_2 (m_2 - m_1)}{\rho \rho_m} \nabla \ln p\right) + \frac{3\rho}{\rho_1 \rho_2} D_T \nabla \ln T\right] \\
\nabla x_1 = -\frac{D_T}{T D_{12}} \nabla T - \frac{\rho_1 \rho_2 (m_2 - m_1)}{p \rho \rho_m} \nabla p.
\end{aligned} \tag{3.43}$$

Inserting for Equation (3.41), and taking finite differences as an approximation to the gradients yields

$$\frac{n_1 + \Delta n_1}{n + \Delta n} - \frac{n_1 - \Delta n_1}{n - \Delta n} \approx -\frac{D_T}{T D_{12}} \Delta T - \frac{\rho_1 \rho_2 (m_2 - m_1)}{p \rho \rho_m} \Delta p. \tag{3.44}$$

From the total differential of pressure,

$$\Delta p \approx \left(\frac{\partial p}{\partial T}\right)_{\mathbf{n}, V} \Delta T + \sum_i \left(\frac{\partial p}{\partial n_i}\right)_{T, V, n_k} \Delta n_i. \tag{3.45}$$

Given a thermal diffusion ratio, and a separation of component 1, Equation (3.44) and (3.45) can be solved numerically for Δn_2. The resulting curve describes the steady state relation between Δn_1 and Δn_2 for a given thermal diffusion ratio. Along this curve, both Δx_1 and Δp may vary while Equation (3.43) is obeyed. That is, if a thermal diffusion ratio is supplied from the Enskog solutions, this curve describes the steady states permitted by the Enskog solutions.

To summarise, the relation between the molar separation of the components of a binary system, Δn_1 and Δn_2, subjected to a temperature difference ΔT have been derived under three constraints. The first is that of equal container mass, the second is equal container pressure, the third is that the Enskog solutions are obeyed. Kempers assumes that the steady state is characterised by a minimum in the target function τ, given in Equation (3.35), along one of the first two curves.

4 Results

This Section consists of two main parts: The first focuses on the Enskog solutions, the second on the Kempers model.

First the stability and convergence of the implementation of the Enskog solutions for Mie fluids is investigated. The results are similar to what has previously been found regarding the stability and convergence of these equations when using a hard sphere potential.[25] Then a review of the Mie potential parameters used in this work is conducted. After these preliminary investigations, the Enskog solutions for Mie fluids are used to predict transport coefficients at different conditions, for a variety of both mixtures and pure fluids. The results of these predictions are compared to both experimental and simulation data as well as predictions obtained from the Enskog solutions for hard spheres.

The second part begins with testing the proposed modification to the Kempers model, before an analysis of the assumptions behind the Kempers model is conducted. In this analysis the implementation of the Enskog solutions is used to investigate whether Kempers assumptions regarding the steady state being at a maximum in the canonical partition function is consistent with the Enskog solutions. Furthermore, the assumption that kinetic gas theory may be used to predict the thermal diffusion coefficient in the ideal gas state is investigated, and the concept of transport coefficients in an ideal gas mixture is discussed in more detail.

4.1 Stability and convergence of the Enskog solutions

Before studying the physical predictions acquired from the Enskog solutions a convergence and stability analysis was conducted. It has previously been shown that using the analytic hard sphere solutions for the collision integrals the solutions converge at around approximation order $\approx$ 4-5, and that numerical instability becomes significant at orders > 7.[25] The notable result from the previous analysis is the dramatic increase in the condition number of the matrix of Equation (2.79) with increasing order of approximation, resulting in floating point error propagating to large errors in the matrix inversion.

A simple convergence analysis reveals that the same is true when employing a Mie potential as when using the HS-potential, the solutions destabilise at approximation order $\approx 7 - 8$. Given the previously obtained results regarding the nature of this instability, it was not investigated further.[25] An interesting discovery however, was that the diffusion factors d_{-1}, d_0 and d_1 converged far more quickly for a Mie potential than for a HS model. In most cases the changes were on the order of 1 % from the first approximation to the converged value at the 3rd to 5th approximation.

The reason for this more rapid convergence for the Mie potential was investigated, but no clear explanation was found. However, it was noted that if one component was in trace concentrations (< 1 ‰) the convergence took longer, requiring up to the 6th or 7th approximation before converging. As previously found,[25] having one component in trace concentration stabilises the numerics, such that one can go to higher order approximations before the solutions become unstable.

Following these observations, the 3rd Enskog approximation was chosen as the default for

all computations. This order of approximation is used unless a different order is explicitly stated.

4.2 Review of Mie parameters

With the exception of H_2O, all Mie parameters used to represent real fluids in this work are currently available in the ThermoPack database.[32] This section gives an overview regarding what physical properties the parameters have been fitted to, and to what degree the parameters have been successful in reproducing those properties. A summary of the parameters and some reported deviations from data, either obtained from experiment, a reference EoS, or simulations, is given in Table 4.1.

With the exception of hydrogen and deuterium heat capacities, and CO_2 and deuterium speed of sound, SAFT-type equations of state appear to quite reliably reproduce the equilibrium behaviour of these fluids. Aasen et al., who have regressed the parameters for hydrogen, deuterium and neon, report significantly improved accuracy when using the Feynman-Hibbs quantum corrected Mie potential.[31] The implementation of the Enskog solutions developed in this work makes it possible to utilise such a potential, but this route was not pursued. However, Aasen et al. also report mixing parameters k_{ij} and ℓ_{ij} for mixtures of helium, neon and deuterium. These are used in this work when computing cross-interaction parameters for mixtures of these components.

For computations involving water, the temperature dependent parameters reported by Lobanova et. al. were used.[48] These are given as

$$\begin{aligned} \sigma &= 3.119 - 4.554 \cdot 10^{-4} T - 8.720 \cdot 10^{-8} T^2 + 1.262 \cdot 10^{-9} T^3, \quad [\text{Å}] \\ \varepsilon &= 586.8 - 0.3077 T + 1.105 \cdot 10^{-5} T^2, \quad [k_B] \end{aligned} \tag{4.1}$$

with $(\lambda_r, \lambda_a) = (8, 6)$. These parameters have been regressed to reproduce the vapour-liquid equilibrium properties of water. As shown in Table 4.1, the agreement with experimental data is not excellent. However, water is commonly known as a notoriously difficult molecule to model with a simple potential model such as the Mie potential, due to the high degree of hydrogen bonding, and the polar nature of the molecule. It is worth mentioning that when using these parameters in MD simulations they report systematically under-predicting the self diffusion coefficient of water.

An important point to note is that, with the exception of oxygen, the parameters here are fit to equilibrium properties. This carries the implication that quality of the model predictions should be representative of the predictive power of the Enskog solutions for Mie fluids, rather than a result of parameter fitting.

4.3 Analysis of the Enskog solutions

The Enskog solutions provide a means of computing both diffusion coefficients and conductivities of gases, in addition to the Soret coefficient. The implemented model was tested with regard to it's ability to reliably reproduce the conductivities, diffusivities and thermal diffusion coefficient of a large number of gases and supercritical fluids. The Mie potential parameters given in Table 4.1 were used for all computations. In computations

Table 4.1: Mie potential parameters used in this work. The rightmost columns show deviations from reference data for some common properties, the vapour pressure p_vap, the saturated liquid density ρ_{liq}^{sat}, the enthalpy of vaporisation $\Delta_{vap}H$, the critical temperature T_c, the speed of sound u_s and the isobaric heat capacity C_p, predicted by either a SAFT-type EoS or MD simulations, as reported by those that have regressed the parameters. The reference data is obtained either from experimental measurements, MD or a reference EoS.

					Reported deviations [%]						
Specie	σ [Å]	ε [k_B]	λ_a [-]	λ_r [-]	p_{vap}	ρ_{liq}^{sat}	$\Delta_{vap}H$	T_c	u_s	C_p	Ref.
Xe	3.9011	227.55	6.0	12.0	3	0.5	2				[49]
O_2[(a)]	3.433	113.0	6.0	12.0							[50]
CO_2	3.1916	231.88	5.1646	27.557	0.40	1.18	3.26		10.70	3.49	[43]
Ne	2.8019	29.875	6.0	9.6977	0.06	0.4		1.69	1.37	5.98	[31]
CH_4	3.7412	153.36	6.0	12.65	0.63	0.78	2.86		1.29	4.73	[43]
D_2	3.1538	21.2	6.0	8.0	2.15	5.24		1.25	9.34	45.15	[31]
He[(b)]	3.353	4.44	6.0	14.84							[51]
H_2	3.2574	17.931	6.0	8.0	3.84	9.01		3.38	3.35	93.32	[31]
Kr[(c)]	3.64	166.66	6.0	12.0							[52]
Ar	3.404	117.84	6.0	12.085	0.21	0.66	3.09	2.19	2.13	1.77	[53]
N_2[(d)]	3.656	98.94	6.0	12.26							[54]
H_2O	(e)	(e)	6	8	4	1	15.9	3.09	-	34.6	[48]

[(a)] Fitted to diffusion coefficient for use in metallurgical modelling.
[(b)] Values obtained from the correlation proposed by Meija et al.[55]
[(c)] It is not reported how the parameters are obtained.
[(d)] Deviations in the order of 2-5 % measured against interfacial tensions.
[(e)] Temperature dependent parameters given in Equation (4.1).

using a hard sphere potential, the Mie potential σ-parameter was used for the hard sphere diameter.

The average absolute deviation (AAD) between predictions and measurements is reported as

$$\text{AAD} = \frac{1}{N}\sum_i \frac{|\varphi_i - \hat{\varphi}_i|}{\varphi_i} \tag{4.2}$$

where φ_i are the measured values, $\hat{\varphi}_i$ are the predicted values, and N is the number of measurements. Similarly, the average deviation (AD) is reported as

$$\text{AD} = \frac{1}{N}\sum_i \frac{\varphi_i - \hat{\varphi}_i}{\varphi_i}. \tag{4.3}$$

Both values are used, as a large AAD may be due to large spread in experimental data that centres around model predictions, in which case the AD should be small. If both the AAD and AD are large, this is indicative of a systematic discrepancy between model predictions and reported data. There may be systematic discrepancies that are not captured by these

measures, but they are deemed sufficient to give a good first indication of the models quality. In section 4.3.3 an additional measure, the Pearson correlation coefficient, ρ_P, computed as

$$\rho_P = \frac{\mathrm{Cov}[\varphi, \hat{\varphi}]}{\mathrm{Var}[\varphi]^2 \mathrm{Var}[\hat{\varphi}]^2} \tag{4.4}$$

where $\mathrm{Cov}[\varphi, \hat{\varphi}]$ is the covariance of predicted and reported values, and $\mathrm{Var}[\varphi]$ is the variance of φ, is used to analyse the discrepancy between measured and predicted values.

4.3.1 Diffusion

For a large variety of binary noble-gas mixtures, the Enskog solutions for Mie fluids reliably reproduced experimental results, as shown in Figure 4.1. The average absolute deviation over 193 data points was 2.77 %, with 88 % of the predictions lying within ±5 %, and 96.8 % of predictions lying within ±7.5 % of data reported by Hogervorst, with a reported accuracy of 1-3 %.[56]

In contrast, using a hard-sphere potential the AAD was 26.4 %, with a large, systematic under-prediction of the diffusion coefficient, especially at high temperatures. Predictions using hard sphere potentials are shown in Figure B.1.

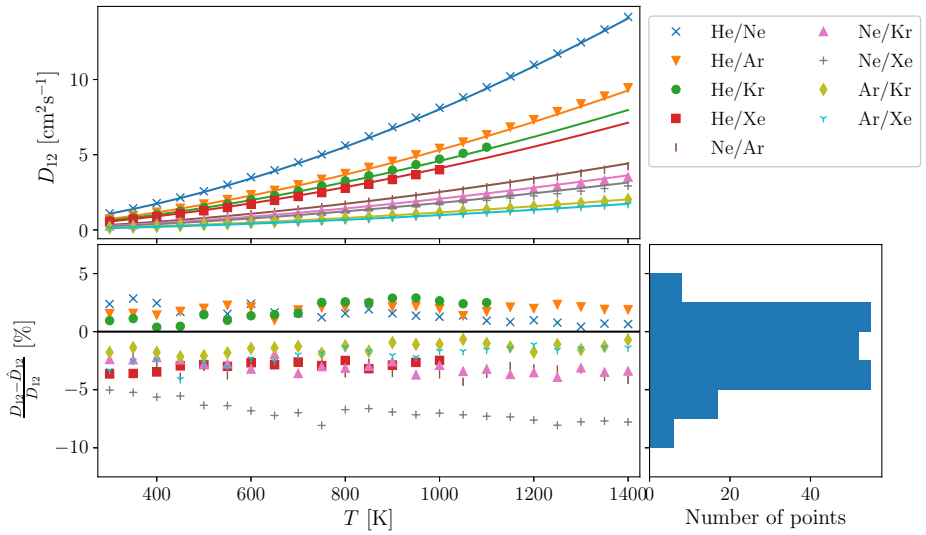

Figure 4.1: Predicted (lines) and measured (marks) diffusion coefficients of noble-gas mixtures at $p = 1\,\mathrm{atm}$, densities supplied to the Enskog solutions were computed using the SAFT-VR Mie EoS. Predctions made using Mie potentials. Helium mixtures contain 98.5 % Helium, the remaining mixtures contain 99 % of the first component. Data reported by Hogervorst.[56]

Yoshida et al. report the self diffusion coefficient of water along several super-critical isotherms.[57] As shown in Figure 4.2 the Enskog solutions for Mie fluids reproduce the diffusion coefficient at the lower reported densities, but becomes unreliable at higher densities and temperatures, with predicted values deviating by 10-20 % from those reported.

It is evident that the density corrections discussed in Section 2.3.7 are unable to capture all the effects of increased density. However, as previously mentioned, the water molecule is notoriously difficult to model, as it is highly polar and prone to forming hydrogen-bonds. In light of this, the discrepancies of 10-20 % are in fact smaller than what one might expect. Additionally, it is notable that the clear trend of under-predicting the diffusion coefficient is the same as that reported by Lobanova et al. when using these parameters in MD-simulations.[48]

Predictions using a hard sphere potential are shown in Figure B.2. Deviations from reported data when using a hard sphere potential is significant, ranging up to 40 % even at lower densities.

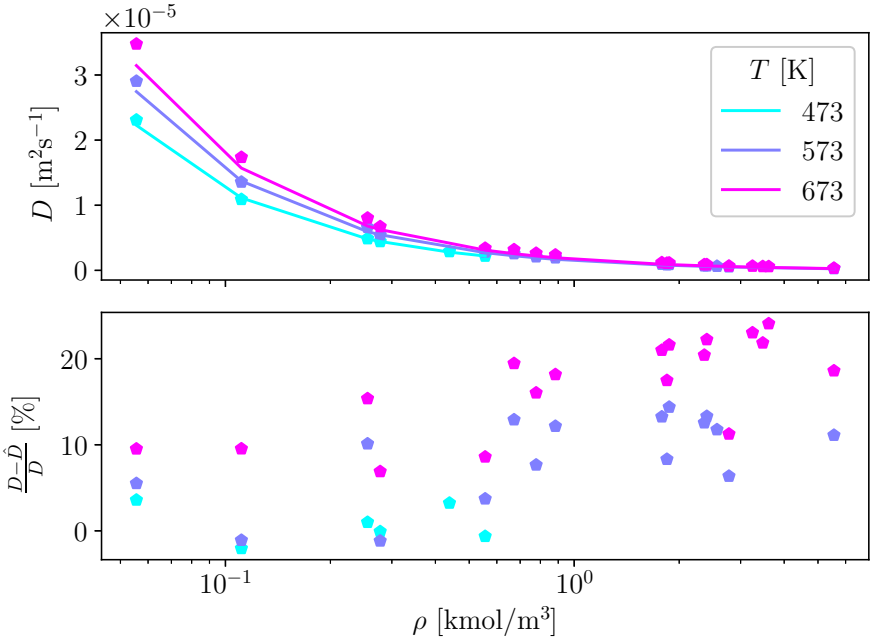

Figure 4.2: Self-diffusion coefficient of supercritical water at several isotherms. Lines are predictions by the Enskog solutions for Mie fluids, marks are data reported by Yoshida et al.[57]

Despite the discrepancy between the Enskog solutions and reported data for water at high temperatures and densities, the disagreement was notably $\lesssim 10$ % at temperatures at or below 573 K when using a Mie potential. Therefore, the high-density regime was investigated further. As shown in Figure 4.3, the deviation from measured data increases rapidly as the density becomes liquid-like.

Afshin et al. report their simulation results in reduced units, and do not report the potential parameters they have used, other than the exponents. The values shown in Figure 4.3 are computed using the Mie parameters of Helium but with repulsive and attractive exponents 14 and 7. Using other sets of Mie parameters only resulted in scaling of the results. These results were not compared to predictions using a hard sphere potential, as the results would depend upon the choice of the ε-value one uses to obtain the temperature from the reported dimensionless temperature.

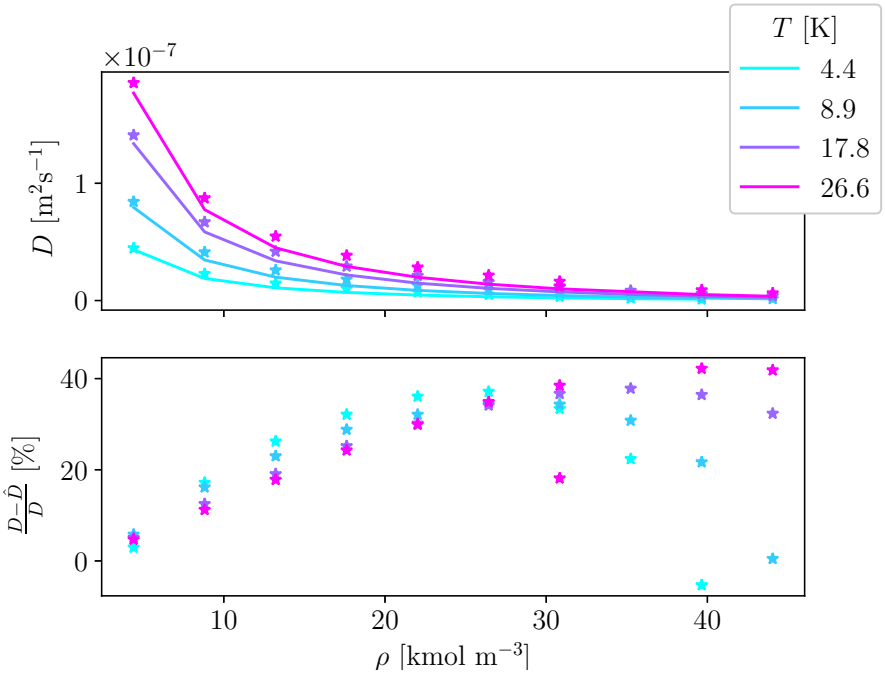

Figure 4.3: The self-diffusion coefficient of the Mie-14-7 fluid, as predicted by the Enskog solutions for Mie fluids and measured by MD-simulation, along several isotherms. Measurements by Afshin et al.[58] Values computed using Mie parameters for helium.

To compare the different data sets, the reduced phase point of the measurements shown in Figures 4.1, 4.2 and 4.3, in addition to measurements for a CO_2/CH_4 mixture reported by Geuvara-Carrion et al,[59] is shown in Figure 4.4. The reduced phase point is computed as

$$\begin{aligned} \rho^* &= \rho N_A \sigma^3, & \sigma &= \sum_i \sum_j x_i x_j \sigma_{ij}, \\ T^* &= T \frac{k_B}{\varepsilon}, & \varepsilon &= \sum_i \sum_j x_i x_j \varepsilon_{ij} \end{aligned} \tag{4.5}$$

where the cross-interaction parameters are obtained via the LB mixing rules. It is clear from Figure 4.4 that the deviation between the predicted and measured diffusion coefficient is stable and on the order of $\lesssim 10 - 15\%$ until a reduced density of ≈ 0.1, after which it increases rapidly. There does not appear to be a clear correlation between the temperature and the deviation from measured data. Notably, a reduced density of 0.1 corresponds to an average inter-particle distance of only $\approx 2.15\sigma$, a relatively short distance when having in mind the assumptions behind the Enskog solutions.

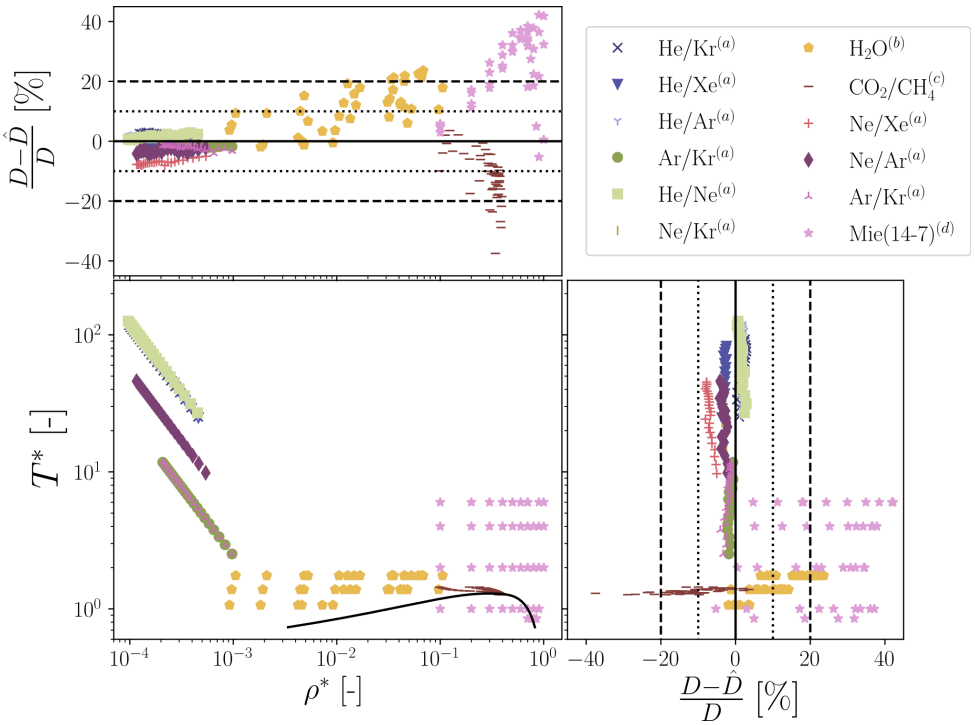

Figure 4.4: Relative discrepancy between the Enskog solutions for diffusion using a Mie potential and reported values presented in Section 4.3, and the reduced phase point of the reported data. The black solid line in the central figure indicates the phase envelope of the LJ-fluid as computed with SAFT-VR Mie. Dotted and dashed lines indicate the 10th and 20th percentiles respectively. $^{(a)}$Hogervorst,[56] $^{(b)}$Yoshida et al.,[57] $^{(c)}$Guevara-Carrion et al.,[59] $^{(d)}$Afshin et al.[58]

4.3.2 Conductivity

Further, the Enskog solutions' ability to reproduce experimental conductivities was investigated. As shown in Figure 4.5, the predictive capability of the solutions varies notably between different species, and deteriorates rather quickly with increasing density for some species.

Using hard sphere potentials the disagreement between predictions and measurements ranged from -40 % to +30 %, even at the lowest densities. Very few predictions made with the hard sphere potentials were within ±10 % of measurements. Conductivity predictions made with hard sphere potentials are shown in Figure B.3.

For predictions made with Mie potentials, the reduced state point of the various measurements was investigated. This revealed that the disagreement between predictions and measurements increases far more rapidly at low reduced temperatures, as shown in Figure 4.6. As all the presented conductivity measurements are in the gas phase, it is deemed unlikely that long time-correlations and thereby correlated collisions are the reason for the deviations, even at low temperature. However, it was commented in Section 2.3.10 that the implemented density corrections for conductivity in mixtures are a simplification. These results may be indicative that the assumptions made when simplifying the density corrections are better at higher temperatures.

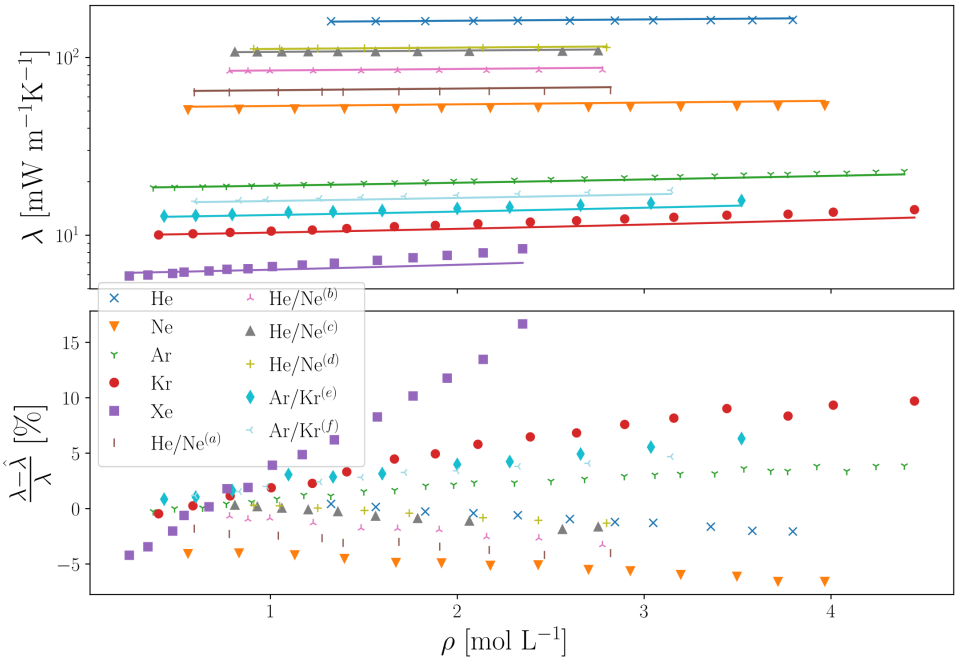

Figure 4.5: Conductivity of noble gases and noble gas mixtures at varying density. Predictions by the Enskog solutions with Mie potentials. All measurements at 35 °C.$^{(a)}x_{\mathrm{He}} = 0.2172$, $^{(b)}x_{\mathrm{He}} = 0.4662$, $^{(c)}x_{\mathrm{He}} = 0.6823$, $^{(d)}x_{\mathrm{He}} = 0.7156$, $^{(e)}x_{\mathrm{Ar}} = 0.4088$, $^{(f)}x_{\mathrm{Ar}} = 0.7059$. Measurements reported by Assael et al.[60]

4.3.3 The thermal diffusion ratio

Vargaftik has compiled an extensive set of thermal diffusion ratios for dilute gas mixtures at varying composition and temperature.[61] For 970 of these data points, Mie potential parameters have been acquired, as presented in Section 4.2. Before comparing the experimental values to model predictions, the data set for each mixture was visually inspected. In total 32 data points were disregarded as clear outliers, these were evenly distributed throughout the data set when regarding mixture components, composition, temperature and reduced temperature.

As shown in Figure 4.7, there is a clear trend of the Enskog solutions over-predicting the thermal diffusion ratio when supplied with a Mie potential. However, closer inspection revealed that practically all the bias could be attributed to various mixtures containing hydrogen. Aasen et al. have shown that hydrogen mixtures can exhibit significant non-ideality, and that quantum effects can play a significant role in the behaviour of hydrogen.[31] When predicting equilibrium properties of hydrogen and hydrogen mixtures they find that a Feynmann-Hibbs corrected Mie potential gives significant improvement in model predictions compared to an ordinary Mie potential. Additionally, they report mixing parameters k_{ij} and l_{ij} for mixtures of hydrogen with neon and helium. Using the mixing parameters they report in the computation of the cross interaction parameters, as described in Section 2.2 removed the bias in the predictions regarding these mixtures. It is therefore likely that the mixtures of hydrogen with carbon dioxide, nitrogen, and oxygen, indicated in Figure 4.7a also have a bias due to the mixing rule being skewed,

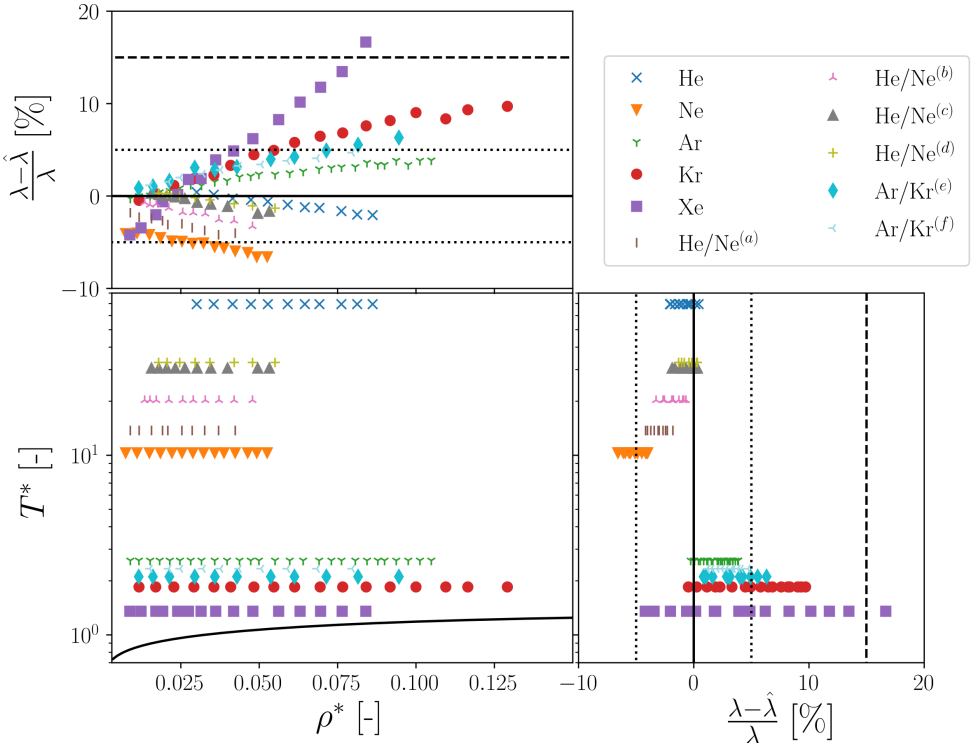

Figure 4.6: The reduced phase point of the measurements presented in in Figure 4.5. The solid black line in the central figure indicates the vapour-liquid equilibria for the Lennard-Jones fluid, computed using the SAFT-VR Mie EoS. Dotted and dashed lines indicate the 5th and 10th percentiles respectively. $^{(a)}x_{\mathrm{He}} = 0.2172$, $^{(b)}x_{\mathrm{He}} = 0.4662$, $^{(c)}x_{\mathrm{He}} = 0.6823$, $^{(d)}x_{\mathrm{He}} = 0.7156$, $^{(e)}x_{\mathrm{Ar}} = 0.4088$, $^{(f)}x_{\mathrm{Ar}} = 0.7059$. Measurements reported by Assael et al.[60]

and possibly due to quantum effects that are not captured by the Mie potential.

Separating the hydrogen mixtures for which no mixing parameters are supplied from the remaining data set, as shown in Figure 4.7b, clearly demonstrates that the bias for over-predicting the thermal diffusion ratio with the Mie potential is largely confined to these specific mixtures. The remaining data points, indicated as blue dots and a blue field in Figure 4.7, are close to normally distributed about the model predictions. It is noted that all the mixtures with large, systematic discrepancies between predictions and measurements contain multi-atomic species, all of which have a non-zero quadrupole moment. For these species, the approximations of a spherical potential and neglecting rotational or vibrational energy are expected to be worse than for monoatomic species.

The AAD of the thermal diffusion coefficients is significant at 16.4 % for the data set as a whole, and looking at Table 4.2 it is clear that very few mixtures have average deviations close to zero. However, the bias does not appear to correlate clearly with anything other than the presence of hydrogen. The correlation between the relative deviation and molar masses, molar mass differences, temperature, reduced temperature, molecular size, molecular density and potential well depth was checked, as shown in Appendix A. The largest correlation coefficient was observed between the deviation and the maximum well depth among the two components, but this appears to arise more from the varying size of the

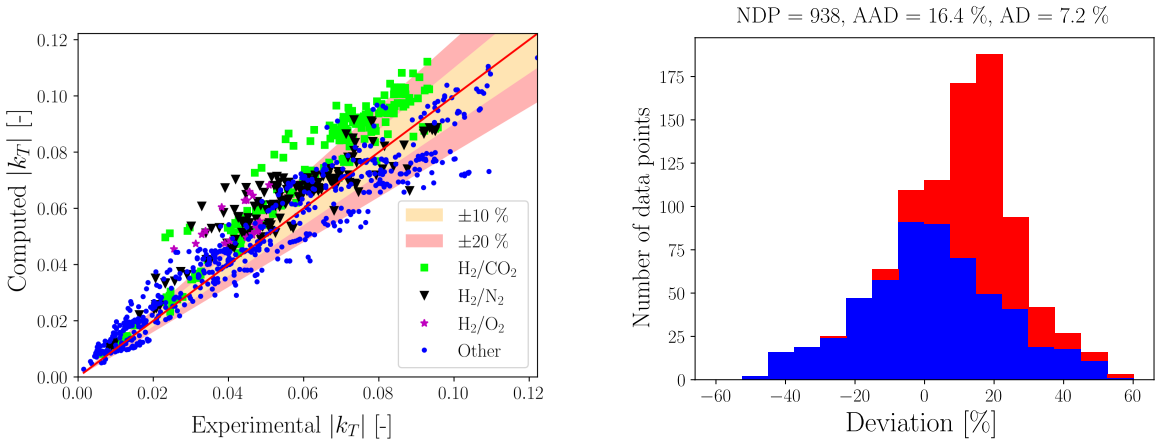

(a) (b)

Figure 4.7: (a) Correlation between predicted and reported thermal diffusion ratio using a Mie potential. Mixtures that showed systematic deviations when using the Mie potential are indicated. (b) Stacked distribution of deviation between predicted and measured thermal diffusion ratios using a Mie potential. Red fields are the specific mixtures indicated in (a), blue fields are the remaining mixtures, indicated with blue dots in (a). AAD and AD are computed using all points.

data sets than any actual underlying correlation. Furthermore, the apparent correlation of error with the presence of hydrogen may be due to systematic experimental errors, as hydrogen gas is notorious for being able to diffuse well through most substances, possibly leading to systematically erroneous measurements.

Due to the manner in which the entirety of the data centres around the model predictions, even though few of the individual mixtures' data sets do, it is believed that the large deviations are primarily due to experimental error. This is supported by the large standard deviation in the discrepancy both within the individual data sets, and the the data set as a whole, as well as the lack of a clear correlation between the deviation and any physical property of the mixtures.

For comparison, Figure 4.8 shows the predictions obtained from the Enskog solutions when using a hard sphere (HS) potential. The HS diameters were set to be equal to the σ-parameters of the Mie potentials used for the predictions displayed in Figure 4.7. There is no doubt that there is a large, systematic error in the predictions. Additionally, as can be seen in Figure 4.8b, the errors to not appear to follow a normal distribution as one would expect if they were the result of experimental error.

Just as with the Mie-potential predictions displayed in Figure 4.7, an investigation was made into whether the errors correlated with any physical parameters. It was found that the error correlated weakly with the inverse temperature, but that this correlation was amplified by the reduced mass of the particles, the combined descriptor

$$\hat{\epsilon}_T = \frac{m_1 m_2}{m_1 + m_2} \frac{1}{T} \tag{4.6}$$

visually appeared to capture a correlation in the discrepancy between measurements and

Table 4.2: Average deviation (AD) and average absolute deviation (AAD) between data reported by Vargaftik and predictions by the Enskog solutions for Mie fluids and hard spheres (HS).[61] The mixtures for which mixing parameters reported by Aasen et al. were available, these were used in the computations for Mie fluids.[31]

	AD [%]		AAD [%]				AD [%]		AAD [%]		
Mixture	Mie	HS	Mie	HS	NDP	Mixture	Mie	HS	Mie	HS	NDP
H_2/CO_2	15.8	49.8	16.2	49.8	194	H_2/D_2	-6.7	45.2	19.5	45.2	27
H_2/N_2	12.3	55.3	14.7	55.3	165	H_2/O_2	21.0	63.9	21.0	63.9	22
He/Ar	-3.3	33.2	10.7	33.2	85	N_2/Ar	-29.3	58.9	29.8	58.9	22
He/Ne	-16.5	25.1	16.7	25.1	66	D_2/N_2	6.2	55.0	7.8	55.0	15
H_2/He	17.0	50.5	19.2	50.5	58	He/N_2	-25.8	21.7	25.9	21.7	14
N_2/CO_2	32.1	66.2	32.5	66.2	58	Ne/Xe	9.6	55.6	14.2	55.6	11
Ne/Ar	0.0	50.9	8.2	50.9	48	D_2/Ne	9.1	53.3	9.1	53.3	11
O_2/CO_2	7.7	54.4	14.9	54.4	43	He/Xe	4.6	38.5	8.1	38.5	11
H_2/Ne	-11.0	40.4	15.3	40.4	42	Ar/Xe	17.1	76.7	17.1	76.7	5
H_2/Ar	12.6	55.3	13.6	55.3	39	H_2/CH_4	24.9	54.3	24.9	54.3	2

predictions, shown in Figure A.4. Further, the discrepancy appeared to correlate with the inverse of the mass difference. This correlation was also amplified by the reduced mass of the species, this correlation was largely captured by the descriptor

$$\hat{\epsilon}_m = \frac{m_1 m_2}{m_1 + m_2} \frac{1}{|\Delta m|}, \tag{4.7}$$

as shown in Figure A.5. Finally, there appeared to be a positive correlation between the mole fraction of the heavier component and the discrepancy. From these observations, the combined descriptor

$$\hat{\epsilon} = \frac{m_1 m_2}{m_1 + m_2} \left(\frac{1}{T} + \frac{0.05}{|\Delta m|} \right) + 0.05 x_2 \tag{4.8}$$

was constructed, where x_2 is the mole fraction of the heavier component. The scaling factors of 0.05 were introduced such that the different terms of the descriptor would be of approximately the same order of magnitude. The correlations for the individual descriptors $\hat{\epsilon}_T$, $\hat{\epsilon}_m$ and x_2 are shown in Appendix A.

As shown in Figure 4.9 there is a convincing correlation between $\hat{\epsilon}$ and the discrepancy, and the correlation coefficient is 0.59. This is not a very high correlation coefficient, but given the large spread in the data, it is significant. More important is the fact that visually, it is clear that the discrepancy increases with $\hat{\epsilon}$, both within most of the mixtures and between mixtures.

The fact that a simple function of the physical parameters of the system correlates significantly with the discrepancy between predictions and measurements indicates that this discrepancy cannot be wholly attributed to measurement error or inaccurate estimates for the hard-sphere diameters. In fact, taking a closer look at the three terms that constitute $\hat{\epsilon}$ one can deduce a physical significance.

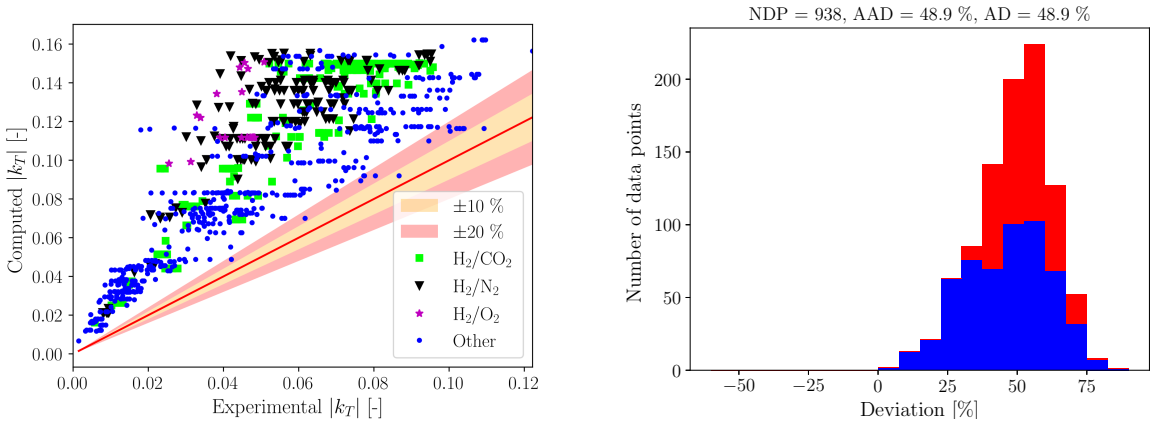

(a) (b)

Figure 4.8: (a) Correlation between predicted and reported thermal diffusion ratio using a HS potential, with HS-diameters equal to the σ-parameters of the Mie potentials used for the predictions in Figure 4.7. Mixtures that showed systematic deviations when using the Mie potential are indicated. (b) Stacked distribution of deviation between predicted and measured thermal diffusion ratios using a HS potential. Red fields are the specific mixtures indicated in (a), blue fields are the remaining mixtures, indicated with blue dots in (a). AAD and AD are computed using all points.

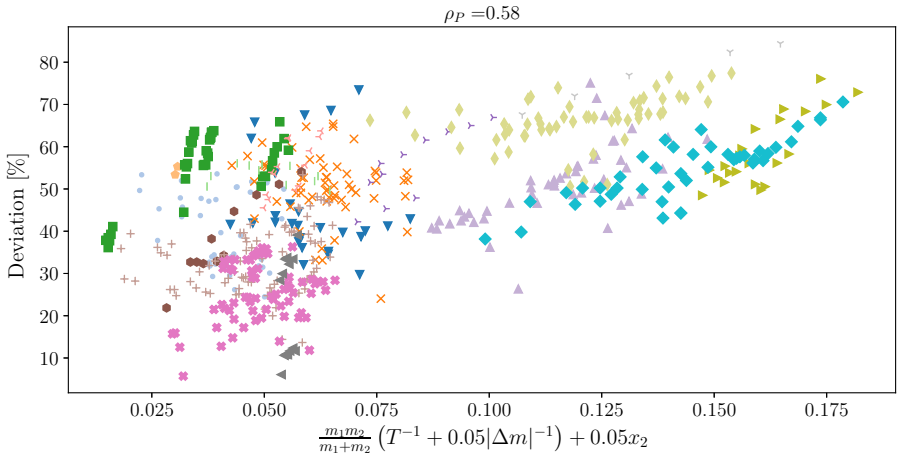

Figure 4.9: Correlation between the descriptor $\hat{\epsilon}$ and the discrepancy between thermal diffusion ratios measured by Vargaftik,[61] and predicted by the 5th order Enskog solutions with a HS potential. Different mixtures are indicated with different colours and markers.

The first term, $\hat{\epsilon}_T = \frac{m_1 m_2}{m_1+m_2}\frac{1}{T}$, is closely related to the average relative speed as, $\bar{g}_{12} \propto \hat{\epsilon}_T^{-\frac{1}{2}}$. That is, the discrepancy increases with decreasing average relative speed during collisions. Assuming that the Mie potential is a somewhat realistic model for the molecular interactions, this makes sense. The softness of the potential and the attractive part of the potential have a larger impact on the collision dynamics at low relative speeds, while the particles behave more like hard spheres during high-speed collisions.

The second term, $\hat{\epsilon}_m = \frac{m_1 m_2}{m_1+m_2}\frac{1}{|\Delta m|}$ is largest for particles of similar mass. In fact, taking m_2 to be the larger mass, $\hat{\epsilon}_m$ can be rewritten to only be a function of the mass ratio,

$$\hat{\epsilon}_m = \frac{m_1 m_2}{m_1+m_2}\frac{1}{|\Delta m|} = \frac{m_1/m_2}{1-(m_1/m_2)^2}, \quad m_2 > m_1. \tag{4.9}$$

As mentioned in Section 1.1, several authors discuss that the Soret effect may be split into an isotope effect and configurational or chemical effects.[1,23] This term captures the fact that for particles of similar mass, the isotope effect will be weak, and the thermal diffusion ratio will to a larger degree be determined by chemical effects, which in turn are determined by the interaction potential. Therefore, it is reasonable that the hard sphere potential systematically gives worse predictions for particles of similar mass.

The final term, x_2, the mole fraction of the heavier component, captures the fact that for most mixtures, the discrepancy between predictions and measurements increased with the mole-average molecular mass. This may also have its roots in the fact that molecular masses are connected to the average molecular speed, such that at high mole fractions of the heavy component, the average molecular speed is lower. As argued when interpreting the significance of $\hat{\epsilon}_T$, faster moving molecules behave more like hard spheres. Therefore it is not unreasonable that a hard sphere model will become less accurate as the number of heavy molecules increase, at the expense of lighter molecules. Thus, this term also appears to have a reasonable physical interpretation.

Despite this analysis, one could argue that using the σ-parameters from a Mie potential to approximate the HS diameters is inaccurate, and that one could achieve more accurate predictions by estimating the HS-diameters in some other way. However, the dependency of the thermal diffusion ratio of hard spheres on temperature and molecular masses, as predicted by the Enskog solutions, is independent of the hard sphere diameters. This means that improving accuracy at some temperature, or for some mixture, even by fitting the hard sphere diameters would likely decrease accuracy at another temperature or for another mixture. This is discussed in more detail in Section 4.6.

4.4 The modified Kempers model

Using the the modified Kempers approach presented in Section 3.2, the Soret coefficient for several mixtures was predicted and compared to simulation data for Mie fluids. The SAFT-VR Mie EoS was used to compute the required thermodynamic properties, using the parameters indicated in Table 4.3. Computing the Soret coefficient for only a few mixtures, shown in Table 4.3 quickly indicated that this approach did not give systematic improvement compared to Kempers 2001 model.

Further investigation was made into how the discrepancy between model predictions and

reported data varied with potential parameters, molecular masses and the state point. However the results were the same as those previously seen,[25] namely that the Kempers model varies between giving predictions in somewhat agreement with data to missing by orders of magnitude. Additionally, the disagreement did not clearly correlate with any meaningful property, other the fact that predictions improved in the low density regime in which the model reduces to the Enskog solutions. The modified Kempers approach was therefore quickly abandoned, and for the case of brevity only the values in Table 4.3 are reported, as an illustrative example of the quality and consistency of the model predictions across the board.

Table 4.3: Soret coefficients of the first component in various equimolar mixtures at the reduced state point $T^* = 0.85$, $\rho^* = 0.81$. Reported values by Reith and Müller-Pathe.[62] Predicted values using (a) the modified Kempers CoV model, (b) the Kempers 2001 CoV model. The state point has been reduced using the cross interaction parameters obtained via the LB mixing rules. All mixtures used the Lennard-Jones (12-6) exponents.

Mixture	Reported S_T [mK^{-1}]	Predicted (a) S_T [mK^{-1}]	Predicted (b) S_T [mK^{-1}]
Xe,Kr	5.1	10.3	8.2
Ar,CH_4	9.3	20.6	9.0
Xe,Ar	18.6	3.8	44.7
Kr,CH_4	22.3	25.5	6.4
Xe,CH_4	23.1	17.6	28.2

Component	σ [Å]	ε [k_B]
Ar	3.405	120.27
Kr	3.633	167.18
Xe	3.975	206.87
CH_4	3.740	152.75

4.5 Kempers assumptions of the steady state

To investigate the assumption that the steady state for a two-bulb system such as the one described in Section 2.4 is a minimum in the target function

$$\tau = \frac{A^{\alpha}}{T^{\alpha}} + \frac{A^{\beta}}{T^{\beta}} \tag{4.10}$$

the target function was computed as a function of Δn_1 and Δn_2 for an ideal gas, using the Sackur-Tetrode equation to compute the pure component entropies. Then, the placement of the curves corresponding to $\Delta p = 0$, $\Delta m = 0$ and the steady state predicted by the Enskog solutions, as derived in Section 3.3, were superimposed on this surface.

Note that without density corrections, the Enskog solutions predict that the Soret coefficient is independent of density. The predicted value is that at infinite dilution. Also, without density corrections, the Enskog solutions recover the ideal gas law, regardless of the intermolecular potential that is used. Because the Enskog solutions for Mie fluids are consistent with the ideal gas law, τ is computed for an ideal gas, rather than using e.g. the SAFT-VR Mie EoS at very low density. It should be commented that SAFT-VR Mie reduces to the ideal gas law at infinite dilution. As a consistency check, the analysis presented in this section was also conducted using the SAFT-VR Mie EoS at very low density. This gave results that, for all practical purposes, were equivalent to those presented here.

The procedure of superimposing the curves corresponding to various constraints on the target function surface allows visualisation of how the target function is permitted to vary with bulb mole numbers when subjected to these constraints. Figure 4.10 displays the target function of an ideal He/Xe mixture with $x_{\mathrm{He}} = 0.5$ (blue grid). Note that the absolute value of the global minimum has been subtracted, such that the global minimum is at $0\,\mathrm{J\,K^{-1}}$, this is simply for clearer visualisation and only changes the absolute value of the target function, not the location of any minima. The red line indicates the path along the surface satisfying $\Delta p = 0$, as determined from Equation (3.40). Likewise, the green line indicates the path along which $\Delta m = 0$. The blue line indicates the steady state predicted by the Enskog solutions, as derived in Section 3.3. The marks on each line indicate the constrained minimum in the target function along that line.

To elaborate, the Enskog solutions permit that the steady state lies somewhere on the blue curve, along which the compositional- and pressure difference may vary. The steady state with no pressure difference that satisfies the Enskog solutions is thereby the intersection between the red and blue curves. The steady state with equal container mass is the intersection between the green and blue curves. It is immediately clear neither of these intersections coincide with the constrained minima along the curves, as assumed by Kempers.

While Figure 4.10 is an illustrative example, this was checked for a variety of mixtures and at varying conditions. For some mixtures the steady states were closer to the minima, for others further away. There did not appear to be a systematic manner of predicting how far away from the minima the steady states would be for a given mixture. Furthermore, for some mixtures the steady state of equal pressure was closer to the minima than that of equal mass, while for others the opposite was true.

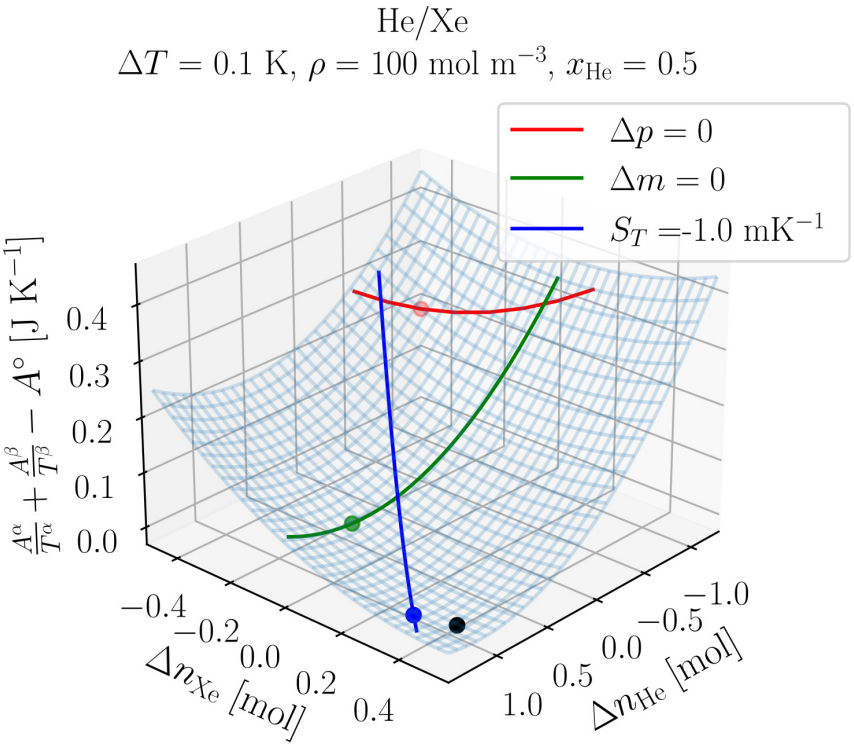

Figure 4.10: The objective function in the Kempers approach, normalised to the global minimum A°, for an ideal He/Xe mixture, with $x_{\mathrm{He}} = 0.5$ at $T = 300\,\mathrm{K}$, with a total mole number of $n = 1000\,\mathrm{mol}$. The red line indicates the curve of no pressure difference, the green line indicates no mass difference, the blue line indicates the separation determined by the Enskog solutions at the bulb average conditions, as derived in Section 3.3. Marks indicate the constrained minimum along each curve, the black mark indicates the global minimum.

These observations are very similar to what has been observed regarding the predictions of the Kempers model: Sometimes predictions are close to measurements, but determining beforehand whether the model will work for a given mixture beforehand has proven itself to be a significant challenge.[25] Also, sometimes the Kempers centre-of-volume model yields better predictions than the centre-of-mass model, while other times the opposite is true, with no clear manner of determining which is appropriate for a given system without checking.

This draws the fundamental assumptions behind the Kempers model heavily into question, and two possible explanations for these observations immediately present themselves: Either the Enskog solutions do not correctly predict the Soret coefficient, even for an ideal gas; or the steady state is not at a minimum, constrained or otherwise, in the target function. Both possibilities are in direct contradiction to Kempers' initial assumptions.

4.6 Thermal diffusion in an Ideal gas

As mentioned in Section 3.2 there is a distinction between a fluid at infinite dilution, and an ideal gas. Strictly, an ideal gas consists of non-interacting point particles. Although both hard spheres and Mie fluids behave as such when regarding equilibrium properties

at infinite dilution, this is not the case regarding non-equilibrium properties. From the derivation in Section 2.3, one will find that the collision integrals vanish for non-interacting particles. Investigating the limiting case in which the collision integrals vanish, one finds that the solutions to Equation (2.79), that yield the polynomial expansion coefficients from which the thermal diffusion ratio is determined, become ill defined, depending on the manner in which the integrals vanish. Explicitly, the limit is different if one lets the radius of the spheres in a hard sphere mixture approach zero from the case in which one lets the well depth parameters of a Mie fluid approach zero. Even restricting the case to that of hard spheres, the limit will be different depending on the mixing rule employed to obtain the cross-interaction diameter, and the ratio of the hard sphere diameters. It should be mentioned that this was only investigated for the 3rd approximation, i.e. there may exist a well defined limit to some Nth approximation, even though the limit to a lower order approximation is not well defined. This is however of little immediate practical consequence. The argument still stands that for some finite approximation to the Enskog solutions, the transport coefficients in the limit of non-interacting particles depends on how one approaches the limit and is therefore ill-defined.

Table 4.4: Mie potential parameters, and the hard sphere diameters producing the same thermal conductivity for the pure fluids at 300 K, 10 mol m^{-3} at the 3rd Enskog approximation.

Potential	σ [Å]	m [g mol^{-1}]	ε [k_B]	λ_a [-]	λ_r [-]
u_1^{Mie}	3.5	10	250	6	12
u_2^{Mie}	3	5	150	6	12
HS1	4.2747	10			
HS2	3.2978	5			

To demonstrate the consequences of this, the hard sphere diameter of two species, simply termed HS1 and HS2, were fit to the pure component conductivity of two Mie fluids, using the potentials u_1^{Mie} and u_2^{Mie} at $T = 300\,\mathrm{K}$, $\rho = 10\,\mathrm{mol\,m^{-3}}$, where the state point was chosen arbitrarily. The Mie potential parameters and the regression results are shown in Table 4.4. As shown in Figure 4.11, using these HS-diameters gave a reasonable match between the HS-conductivity and Mie-conductivity of the mixture at the same state point. However, as shown in Figure 4.12, the temperature dependency is completely different. Furthermore, the diffusion coefficient in the mixtures is completely different. This is by no means surprising, but recognise the fact that because these predictions are made using the non-density corrected Enskog solutions, both these predictions are for an ideal gas.

This underlines the fact that speaking of the transport properties of an ideal gas, as Kempers does, is not fruitful. The transport properties of a fluid at infinite dilution depend upon the interaction potentials, even though equilibrium properties do not. This is by no means news,[9,23,36] but in the context of the Kempers model it shows that predicting the thermal diffusion coefficient through residual properties that may be determined from equilibrium thermodynamics is bound to fail. This is because different equations of state, based on different underlying potentials, will predict the same ideal gas behaviour in the low density limit, while the transport coefficients behave differently based on the underlying potential.

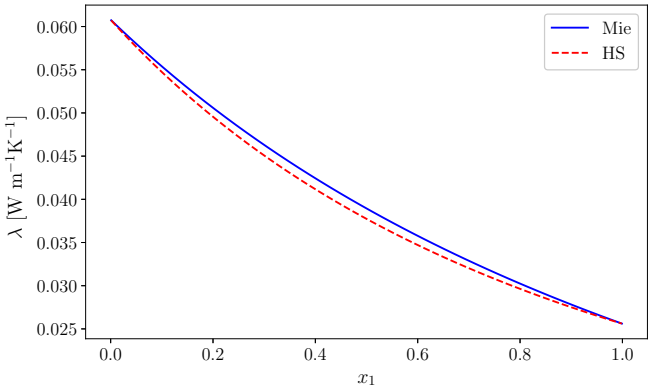

Figure 4.11: Conductivity of the mixture described by the parameters shown in Table 4.4 at 300 K, 10 mol m^{-3}. Computed to the 3rd Enskog approximation.

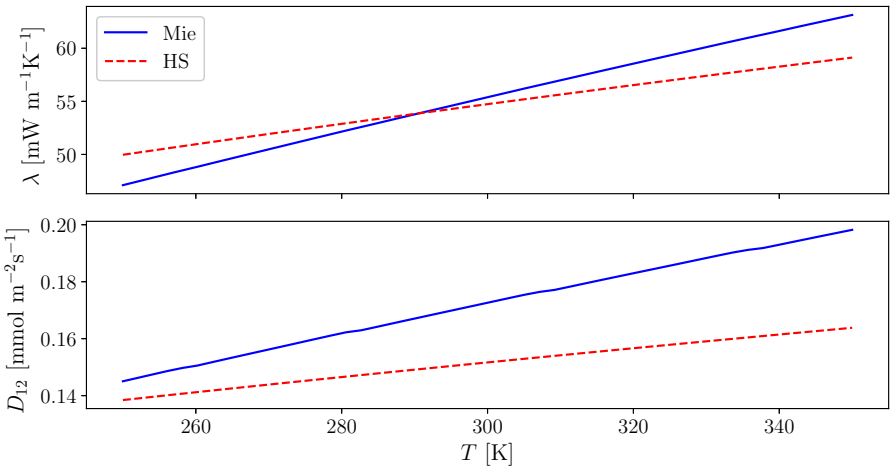

Figure 4.12: Temperature dependency of the conductivity and diffusion coefficient of the hard sphere mixture and Mie mixture described by the parameters in Table 4.4, at $x_1 = 0.1$, $\rho = 10\,\mathrm{mol\,m^{-3}}$.

These results also tie into the argument presented in Section 4.3, regarding the possibility that the poor predictions obtained from the Enskog solutions using hard sphere potentials were due to poor estimates of the hard sphere diameters. Even when fitting the hard sphere diameters to pure component conductivities predictions for the mixture deviated from those obtained from a Mie potential. Recall from Figure 4.5 that the Enskog solutions using a Mie potential predicted the conductivities of mixtures with high accuracy. This demonstrates that using a Mie potential is a significant improvement, even compared to fitting hard sphere diameters to data. Furthermore, the results shown in Figure 4.12 illustrate the fact that fitting hard sphere diameters to one property, in this case conductivity, at a given temperature does not give reasonable predictions for another property, diffusion, or even for conductivity at other temperatures.

5 Conclusion

The Enskog solutions for Mie fluids have been shown to reliably predict diffusion coefficients, conductivities and thermal diffusion coefficients in dilute gas systems, both for pure fluids and mixtures. Notably, the parameters used in the predictions have almost exclusively been obtained from fitting to equilibrium properties rather than transport properties. This is remarkable for several reasons, one is that the issue of obtaining good parameters for the prediction of transport coefficients becomes a far simpler one to solve. There is a plethora of available experimental and simulation data for the equilibrium behaviour of fluids, and SAFT-type equations of state provide a connection between potential parameters and equilibrium behaviour. The results presented here show that one can safely transfer parameters from a SAFT-type EoS to the Enskog solutions and reliably predict transport coefficients. Further, the fact that the SAFT-VR Mie EoS and the Enskog solutions yield reliable predictions of equilibrium and non-equilibrium behaviour respectively, when supplied with the same potential parameters, indicates that the underlying theories are consistent with each other regarding the mechanisms of interaction between particles.

The hard sphere Enskog solutions have been widely used, sometimes with various corrections to the collision integrals, as mentioned in Section 2.3.6. Here, it has been shown that using a Mie potential to explicitly compute the collision integrals not only accurately captures the temperature dependency of the transport coefficients, but also reliably captures the compositional dependency in a manner that hard sphere potentials do not. In summary, explicitly solving the collision integrals using Mie potentials not only provides a great increase in prediction reliability, but also makes obtaining good potential parameters simpler and additionally provides a powerful link between the equilibrium and non-equilibrium behaviour of Mie fluids.

A closer investigation into the Kempers model revealed that the underlying assumptions likely do not hold. The assumption that the steady state of an ideal gas is at a maximum in the canonical partition function appears to be inconsistent with Enskog theory. Given the demonstrated reliability of the predictions obtained from the Enskog solutions in the low density regime, it is deemed unlikely that this is due to a fault in Enskog theory. Regardless, part of Kempers assumptions are that Kinetic gas theory will accurately predict the Soret coefficient in the ideal gas state.

Further, the concept of transport coefficients in an ideal gas was discussed. Both a hard sphere system and a Mie fluid are thermodynamically ideal gases at infinite dilution, but the Enskog solutions provide different transport coefficients for the two. The argument can then be made that even the concept of thermal diffusion in an ideal gas is at best imprecise and at worst meaningless, at least within the framework of Enskog theory. This has ramifications for the manners in which it can be reasonable to split the Soret coefficient into different contributions. Specifically, separating the Soret coefficient into an ideal part and a residual part does not appear to be fruitful, while a separation into an isotopic and a chemical part may still be reasonable.

6 Further work

In light of the fact that the Kempers model is likely fundamentally flawed, the search for an approach to developing a first-principles model of the Soret effect should continue. Approaches with their roots in irreversible thermodynamics or transition theory are so far largely unable to reproduce gas-phase behaviour.[23] For large, complex molecules, kinetic gas theory is also known to be imprecise.[36] In light of this, it should be recognised that modern developments within computer simulations the past 10-20 years greatly facilitates the expansion of an accurate kinetic theory to more advanced molecules, and the possibility of using a kinetic theory in combination with one of the aforementioned approaches to modelling thermal diffusion may be fruitful to pursue.

Work has been conducted on incorporating long time-correlations into a kinetic theory to account for cage- and vortex effects that become significant at high densities.[36] Furthermore, there have been attempts at including vibrational and rotational terms to the energy transfer into the Chapman-Enskog solution method.[63–65] These are interesting developments, that appear fruitful to follow further. The implementation of the Enskog solutions developed in this work may prove useful in this regard. If one wishes to accurately describe more advanced systems, having a good starting point that is reliable for simple molecules at low-medium densities is a necessary prerequisite.

The solution implemented here for Mie potentials is valid for an arbitrary spherical potential, which makes it possible to use in combination with somewhat more complex potentials, such as the Feynman-Hibbs quantum corrected Mie potential.[31] This potential has been shown to reliably reproduce the low-temperature behaviour of some fluids that are poorly described by the Mie potential. The approach used in this work; using a potential that gives reliable predictions for equilibrium properties in combination with the Enskog solutions, should be investigated further, as it appears to be fruitful. Regarding the fact that parameters fit to equilibrium data yield reliable predictions regarding transport phenomena: It is tempting to suggest that one could fit parameters to measured transport coefficients before using them to model equilibrium behaviour. There are likely several potential pitfalls to this approach, but a preliminary investigation into its feasibility may be of interest.

References

[1] M. Rahman and M. Saghir, "Thermodiffusion or soret effect: Historical review," *International Journal of Heat and Mass Transfer*, vol. 73, pp. 693–705, 2014.

[2] S. Kjelstrup, D. Bedeaux, E. Johannessen, and J. Gross, *Non-Equilibrium Thermodynamics for Engineers*. World Scientific Publishing, 2 ed., 2017.

[3] L. Onsager, "Reciprocal relations in irreversible processes. i.," *Phys. Rev.*, vol. 37, pp. 405–426, Feb 1931.

[4] K. Dill and S. Bromberg, *Molecular Driving Forces*. Garland Science, 2 ed., 2011.

[5] K. B. Oldham, J. C. Myland, and A. M. Bond, *Electrochemical Science and Technology*. Wiley, 1 ed., 2013.

[6] C. Guy and J. Schott, "Modelling of soret diffusion in radioactive waste glass," *Applied Geochemistry*, vol. 7, pp. 33–40, 1992. Geochemistry of Radioactive Waste Disposal: a French Contribution.

[7] P. M. Doran, *Bioprocess engineering principles*. Elsevier, 2 ed., 2013.

[8] W. Köhler and K. I. Morozov, "The soret effect in liquid mixtures – a review," *Journal of Non-Equilibrium Thermodynamics*, vol. 41, no. 3, pp. 151–197, 2016.

[9] S. Chapman and T. G. Cowling, *The mathematical theory of non-uniform gases*. Bentley House, 200 Euston Road, London, N.W. 1: Cambridge university press, 3 ed., 1970.

[10] E. Cohen and H. Hartley, *Transport Phenomena in Fluids*. New York, USA: Marcel Dekker, 1969.

[11] J. O. Hirschfelder, C. F. Curtiss, and R. B. Bird, *Molecular Theory of Gases and Liquids*. John Wiley & Sons, 1954.

[12] R. C. Reid, J. M. Prausnitz, and B. E. Poling, *The properties of gases & liquids*. McGraw-Hill Book Company, 4 ed., 1987.

[13] C. Debuschewitz and W. Köhler, "Molecular origin of thermal diffusion in *benzene + cyclohexane* mixtures," *Phys. Rev. Lett.*, vol. 87, p. 055901, Jul 2001.

[14] E. Eastman, "Thermodynamics of non-isothermal systems," *Journal of the American Chemical Society*, vol. 48, no. 6, pp. 1482–1493, 1926.

[15] L. J. T. M. Kempers, "A comprehensive thermodynamic theory of the soret effect in a multicomponent gas, liquid, or solid," *The Journal of Chemical Physics*, vol. 115, no. 14, pp. 6330–6341, 2001.

[16] P.-A. Artola, B. Rousseau, and G. Galliéro, "A new model for thermal diffusion: Kinetic approach," *Journal of the American Chemical Society*, vol. 130, no. 33, pp. 10963–10969, 2008.

[17] K. B. Haugen and A. Firoozabadi, "On measurement of thermal diffusion coefficients in multicomponent mixtures.," *The Journal of chemical physics*, vol. 122, no. 1, 2005.

[18] A. Firoozabadi, K. Ghorayeb, and K. Shukla, "Theoretical model of thermal diffusion factors in multicomponent mixtures," *AIChE Journal*, vol. 46, no. 5, pp. 892–900, 2000.

[19] L. J. T. M. Kempers, "A thermodynamic theory of the soret effect in a multicomponent liquid," *The Journal of Chemical Physics*, vol. 90, no. 11, pp. 6541–6548, 1989.

[20] I. Prigogine, L. De Brouckere, and R. Amand, "Recherches sur la thermodiffusion en phase liquide: (première communication)," *Physica*, vol. 16, no. 7, pp. 577–598, 1950.

[21] L. J. Tichacek, W. Kmak, and H. Drickamer, "Thermal diffusion in liquids; the effect of non-ideality and association.," *The Journal of Physical Chemistry*, vol. 60, no. 5, pp. 660–665, 1956.

[22] R. G. Mortimer and H. Eyring, "Elementary transition state theory of the soret and dufour effects," *Proceedings of the National Academy of Sciences*, vol. 77, no. 4, pp. 1728–1731, 1980.

[23] H. Hoang and G. Galliero, "Predicting thermodiffusion in simple binary fluid mixtures," *The European Physical Journal E*, vol. 45, no. 5, p. 42, 2022.

[24] K. G. Denbigh, "The heat of transport in binary regular solutions," *Transactions of the Faraday Society*, vol. 48, pp. 1–8, 1952.

[25] V. G. Jervell, "Thermodynamic Modelling of the Soret Coefficient." unpublished, 2021.

[26] M. Eslamian and M. Z. Saghir, "Dynamic thermodiffusion theory for ternary liquid mixtures," *Journal of Non-Equilibrium Thermodynamics*, vol. 35, no. 1, pp. 51–73, 2010.

[27] N. F. Carnahan and K. E. Starling, "Equation of state for nonattracting rigid spheres," *The Journal of chemical physics*, vol. 51, no. 2, pp. 635–636, 1969.

[28] H. Hansen-Goos and R. Roth, "A new generalization of the carnahan-starling equation of state to additive mixtures of hard spheres," *The Journal of chemical physics*, vol. 124, no. 15, p. 154506, 2006.

[29] R. Dohrn and J. M. Prausnitz, "A simple perturbation term for the carnahan-starling equation of state," *Fluid phase equilibria*, vol. 61, no. 1-2, pp. 53–69, 1990.

[30] J. T. Cripwell, C. E. Schwarz, and A. J. Burger, "Polar (s)pc-saft: Modelling of polar structural isomers and identification of the systematic nature of regression issues," *Fluid Phase Equilibria*, vol. 449, pp. 156–166, 2017.

[31] A. Aasen, M. Hammer, E. A. Mūller, and Ø. Wilhelmsen, "Equation of state and force fields for feynman–hibbs-corrected mie fluids. ii. application to mixtures of helium, neon, hydrogen, and deuterium," *The Journal of Chemical Physics*, vol. 152, no. 7, p. 074507, 2020.

[32] SINTEF, "ThermoPack." `https://github.com/SINTEF/thermopack/`, 2020.

[33] S. Stephan, K. Langenbach, and H. Hasse, "Interfacial properties of binary lennard-jones mixtures by molecular simulation and density gradient theory," *The Journal of Chemical Physics*, vol. 150, no. 17, p. 174704, 2019.

[34] H. Van Beijeren and M. Ernst, "The non-linear enskog-boltzmann equation," *Physics Letters A*, vol. 43, no. 4, pp. 367–368, 1973.

[35] H. Van Beijeren and M. H. Ernst, "The modified enskog equation," *Physica*, vol. 68, no. 3, pp. 437–456, 1973.

[36] E. Cohen, "Fifty years of kinetic theory," *Physica A: Statistical Mechanics and its Applications*, vol. 194, no. 1, pp. 229–257, 1993.

[37] S. Loyalka, E. Tipton, and R. Tompson, "Chapman–enskog solutions to arbitrary order in sonine polynomials i: Simple, rigid-sphere gas," *Physica A: Statistical Mechanics and its Applications*, vol. 379, no. 2, pp. 417–435, 2007.

[38] E. Tipton, R. Tompson, and S. Loyalka, "Chapman–enskog solutions to arbitrary order in sonine polynomials ii: Viscosity in a binary, rigid-sphere, gas mixture," *European Journal of Mechanics-B/Fluids*, vol. 28, no. 3, pp. 335–352, 2009.

[39] E. Tipton, R. Tompson, and S. Loyalka, "Chapman–enskog solutions to arbitrary order in sonine polynomials iii: Diffusion, thermal diffusion, and thermal conductivity in a binary, rigid-sphere, gas mixture," *European Journal of Mechanics - B/Fluids*, vol. 28, no. 3, pp. 353 – 386, 2009.

[40] R. Tompson, E. Tipton, and S. Loyalka, "Chapman–enskog solutions to arbitrary order in sonine polynomials iv: Summational expressions for the diffusion- and thermal conductivity-related bracket integrals," *European Journal of Mechanics - B/Fluids*, vol. 28, no. 6, pp. 695 – 721, 2009.

[41] M. López de Haro, E. G. D. Cohen, and J. M. Kincaid, "The enskog theory for multicomponent mixtures. i. linear transport theory," *The Journal of Chemical Physics*, vol. 78, no. 5, pp. 2746–2759, 1983.

[42] S. Chapman and T. G. Cowling, *The mathematical theory of non-uniform gases*. Bentley House, 200 Euston Road, London, N.W. 1: Cambridge university press, 2 ed., 1952.

[43] T. Lafitte, A. Apostolakou, C. Avendaño, A. Galindo, C. S. Adjiman, E. A. Müller, and G. Jackson, "Accurate statistical associating fluid theory for chain molecules formed from mie segments," *The Journal of chemical physics*, vol. 139, no. 15, p. 154504, 2013.

[44] V. G. Jervell, "KineticGas." `https://github.com/vegardjervell/Kineticgas`, 2022.

[45] T. Boublík, "Background correlation functions in the hard sphere systems," *Molecular Physics*, vol. 59, no. 4, pp. 775–793, 1986.

[46] V. Papaioannou, T. Lafitte, C. Avendaño, C. S. Adjiman, G. Jackson, E. A. Müller, and A. Galindo, "Group contribution methodology based on the statistical associat-

ing fluid theory for heteronuclear molecules formed from mie segments," *The Journal of Chemical Physics*, vol. 140, no. 5, p. 054107, 2014.

[47] V. G. Jervell, "Kempers01." `https://github.com/vegardjervell/Kempers01`, 2021.

[48] O. Lobanova, C. Avendaño, T. Lafitte, E. A. Müller, and G. Jackson, "Saft-γ force field for the simulation of molecular fluids: 4. a single-site coarse-grained model of water applicable over a wide temperature range," *Molecular Physics*, vol. 113, no. 9-10, pp. 1228–1249, 2015.

[49] J. Vrabec, J. Stoll, and H. Hasse, "A set of molecular models for symmetric quadrupolar fluids," *The Journal of Physical Chemistry B*, vol. 105, no. 48, pp. 12126–12133, 2001.

[50] R. Chen and W. Yuen, "Short-time oxidation behavior of low-carbon, low-silicon steel in air at 850–1180 °c: Ii. linear to parabolic transition determined using existing gas-phase transport and solid-phase diffusion theories," *Oxidation of Metals*, vol. 73, 04 2009.

[51] C. Herdes, T. S. Totton, and E. A. Müller, "Coarse grained force field for the molecular simulation of natural gases and condensates," *Fluid Phase Equilibria*, vol. 406, pp. 91–100, 2015.

[52] I. M. van de Ven-Lucassen, A. M. Otten, T. J. Vlugt, and P. J. Kerkhof, "Molecular dynamics simulation of the maxwell-stefan diffusion coefficients in lennard-jones liquid mixtures," *Molecular Simulation*, vol. 23, no. 1, pp. 43–54, 1999.

[53] S. Dufal, T. Lafitte, A. Galindo, G. Jackson, and A. J. Haslam, "Developing intermolecular-potential models for use with the saft-vr mie equation of state," *AIChE Journal*, vol. 61, no. 9, pp. 2891–2912, 2015.

[54] R. A. Aziz, "A highly accurate interatomic potential for argon," *The Journal of chemical physics*, vol. 99, no. 6, pp. 4518–4525, 1993.

[55] A. Mejía, C. Herdes, and E. A. Müller, "Force fields for coarse-grained molecular simulations from a corresponding states correlation," *Industrial & Engineering Chemistry Research*, vol. 53, no. 10, pp. 4131–4141, 2014.

[56] W. Hogervorst, "Diffusion coefficients of noble-gas mixtures between 300 k and 1400 k," *Physica*, vol. 51, no. 1, pp. 59–76, 1971.

[57] K. Yoshida, N. Matubayasi, and M. Nakahara, "Self-diffusion of supercritical water in extremely low-density region," *The Journal of Chemical Physics*, vol. 125, no. 7, p. 074307, 2006.

[58] A. Eskandari Nasrabad, N. M. Oghaz, and B. Haghighi, "Transport properties of mie(14,7) fluids: Molecular dynamics simulation and theory," *The Journal of Chemical Physics*, vol. 129, no. 2, p. 024507, 2008.

[59] G. Guevara-Carrion, S. Ancherbak, A. Mialdun, J. Vrabec, and V. Shevtsova, "Diffusion of methane in supercritical carbon dioxide across the widom line," *Scientific reports*, vol. 9, no. 1, pp. 1–14, 2019.

[60] M. J. Assael, M. Dix, A. Lucas, and W. A. Wakeham, "Absolute determination of the thermal conductivity of the noble gases and two of their binary mixtures as a function of density," *J. Chem. Soc., Faraday Trans. 1*, vol. 77, pp. 439–464, 1981.

[61] N. Vargaftik, *Tables on the Thermophysical Properties of Liquids and Gases*. 1025 Vermont Ave, NW Washington DC 20005: Hemisphere Publishing Corporation, 2 ed., 1975.

[62] D. Reith and F. Müller-Plathe, "On the nature of thermal diffusion in binary lennard-jones liquids," *The Journal of Chemical Physics*, vol. 112, no. 5, pp. 2436–2443, 2000.

[63] D. Schruben, "Novel kinetic theory of the classical isotropic oscillator gas, the flexible shell model," *Journal of Statistical Physics*, vol. 153, no. 5, pp. 911–930, 2013.

[64] E. Kustova and E. Nagnibeda, "Strong nonequilibrium effects on specific heats and thermal conductivity of diatomic gas," *Chemical physics*, vol. 208, no. 3, pp. 313–329, 1996.

[65] E. V. Kustova and G. M. Kremer, "Chemical reaction rates and non-equilibrium pressure of reacting gas mixtures in the state-to-state approach," *Chemical Physics*, vol. 445, pp. 82–94, 2014.

A Correlation of deviation between kinetic gas theory and reported k_T

To closely investigate the substantial deviation between thermal diffusion ratios obtained from the Enskog solutions and those reported by Vargaftik,[61] the discrepancy between the two was investigated as a function of temperature, molar masses, the potential size parameters, σ, the potential well depth parameters, ε, and combinations of these, collectively termed the descriptors. For the hard sphere solutions, only descriptors involving the molar masses, temperature and hard sphere diameters were considered. The correlation between each descriptor and the discrepancy was inspected visually in addition to computing the Pearson correlation coefficients.

For the Mie fluid solutions, no convincing trends presented themselves, as shown in Figures A.1-A.3. Some of the correlation coefficients were relatively large, at 0.4, but visually this appears to arise from the large variance in the number of measurements for each mixture. The combined descriptors $\frac{\varepsilon}{\sigma^3}$, $\frac{m}{\sigma^3}$ and $T^* = \frac{k_B T}{\varepsilon}$ were also investigated, yielding similar results to those shown in Figures A.1-A.3.

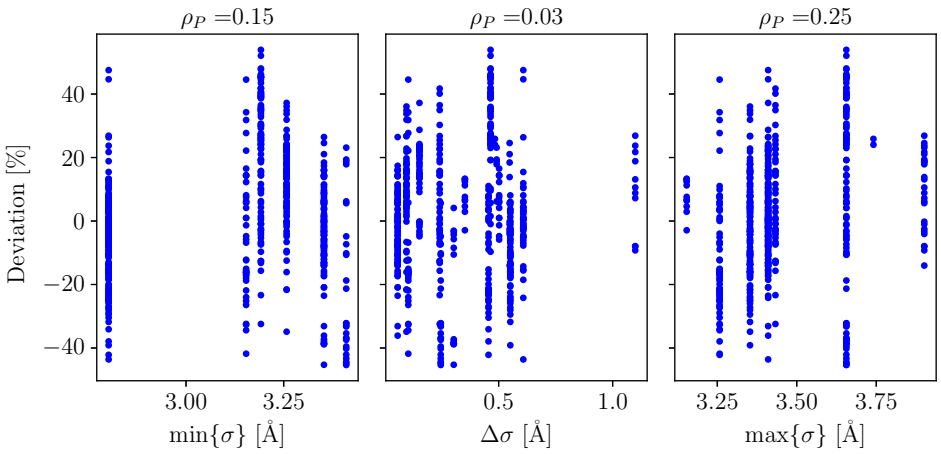

Figure A.1: Correlation between deviation between thermal diffusion ratios obtained from the Enskog solutions for Mie fluids and data reported by Vargaftik, and various descriptors derived from the Mie potential σ-parameter.[61] ρ_P is the Pearson correlation coefficient for each descriptor.

For the hard-sphere solutions, some more convincing trends revealed themselves. These are discussed in detail in Section 4.3.3, the results for the individual descriptors are presented here for completeness. As shown in Figure A.4 and A.5, the correlation of the discrepancy with the descriptors $\hat{\epsilon}_T$ and $\hat{\epsilon}_m$ is clear and convincing. For the case of the descriptor x_2, the mole fraction of the heavier component, one must view each mixture individually to see that there appears to be a weak correlation, as shown in Figure A.6. When used in combination with the other descriptors, as shown in Figure 4.9 and discussed in Section 4.3.3, the result is convincing.

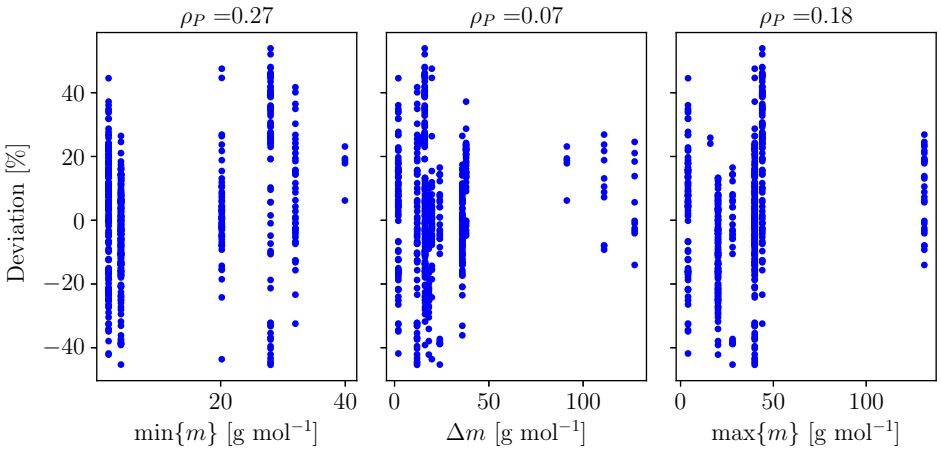

Figure A.2: Correlation between deviation between thermal diffusion ratios obtained from the Enskog solutions for Mie fluids and data reported by Vargaftik, and various descriptors derived from the molar masses.[61] ρ_P is the Pearson correlation coefficient for each descriptor.

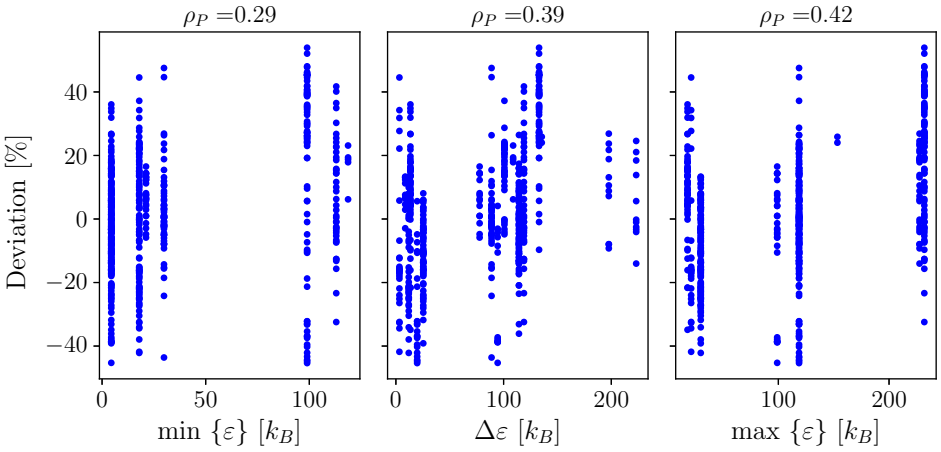

Figure A.3: Correlation between deviation between thermal diffusion ratios obtained from the Enskog solutions for Mie fluids and data reported by Vargaftik, and various descriptors derived from the Mie potential ε-parameter.[61] ρ_P is the Pearson correlation coefficient for each descriptor.

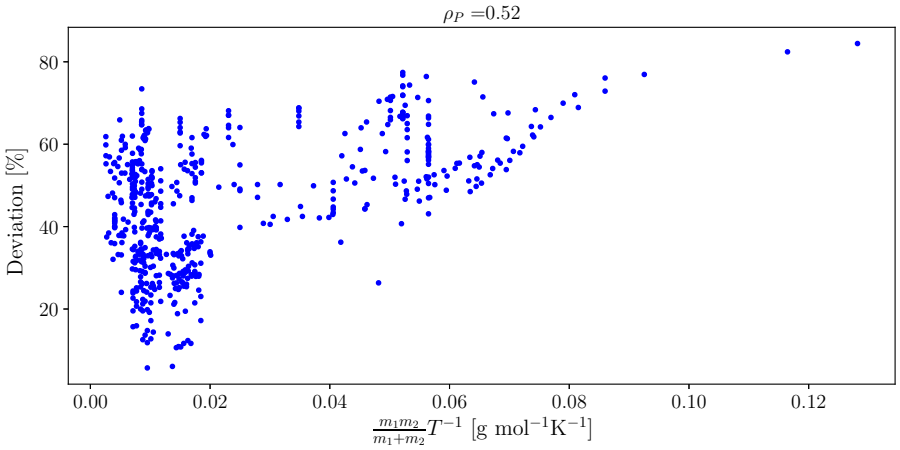

Figure A.4: Correlation between the deviation between the Enskog hard sphere solutions for the thermal diffusion ratio and data reported by Vargaftik, and the descriptor $\hat{\epsilon}_T$.

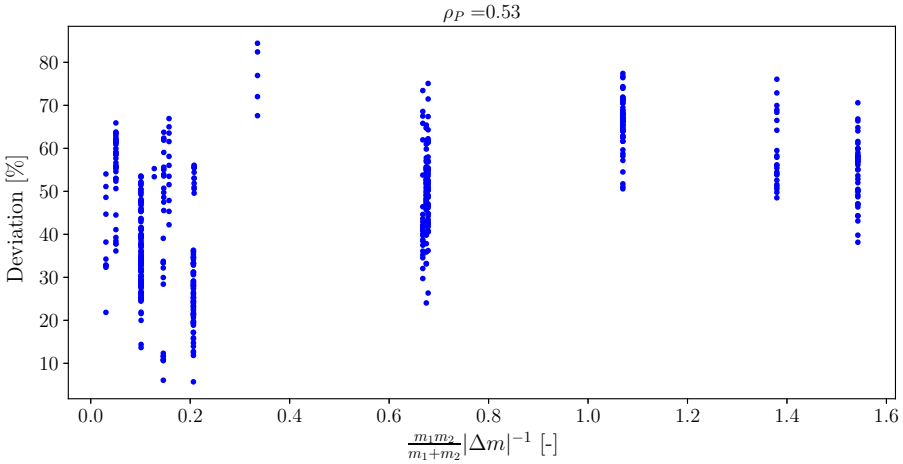

Figure A.5: Correlation between the deviation between the Enskog hard sphere solutions for the thermal diffusion ratio and data reported by Vargaftik, and the descriptor $\hat{\epsilon}_m$.

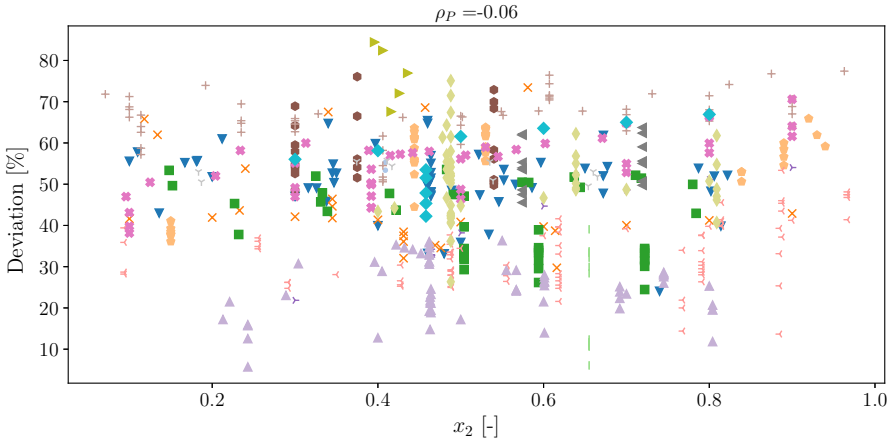

Figure A.6: Correlation between the deviation between the Enskog hard sphere solutions for the thermal diffusion ratio and data reported by Vargaftik, and the mole fraction of the heavier component, x_2. Different mixtures are indicated with different colours and markers.

B Enskog solutions with a hard sphere potential

For comparison with the predictions made by the implementation of the Enskog solutions with a Mie potential, presented in Section 4.3, the same computations were made with a hard sphere potential. In all cases, the hard sphere diameter was set equal to the Mie potential σ-parameter. The results using a hard sphere potential are discussed in Section 4.3, and are collected here for reference.

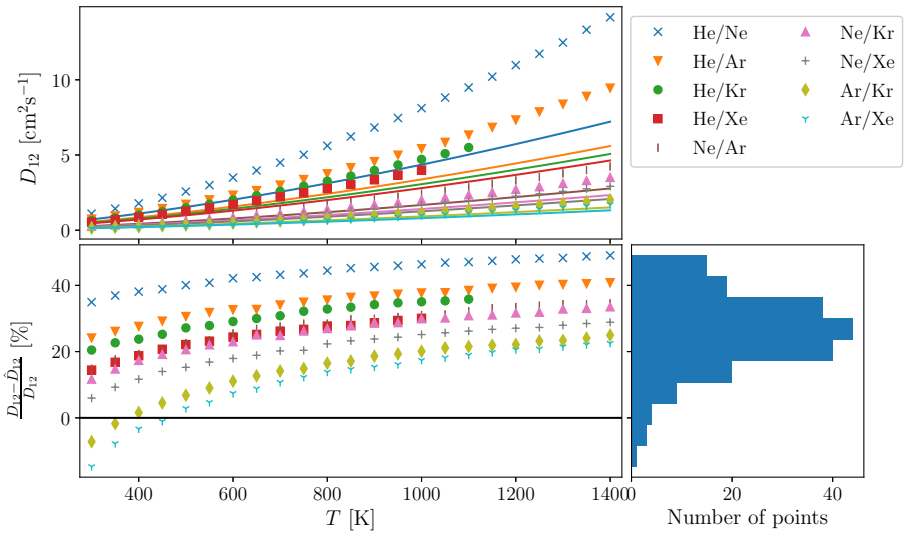

Figure B.1: Predicted and measured diffusion coefficients of noble-gas mixtures at $p = 1$ atm, densities supplied to the Enskog solutions were computed using the SAFT-VR Mie EoS, predictions made using a hard sphere potential. Helium mixtures contain 98.5 % Helium, the remaining mixtures contain 99 % of the first component. Data reported by Hogervorst.[56]

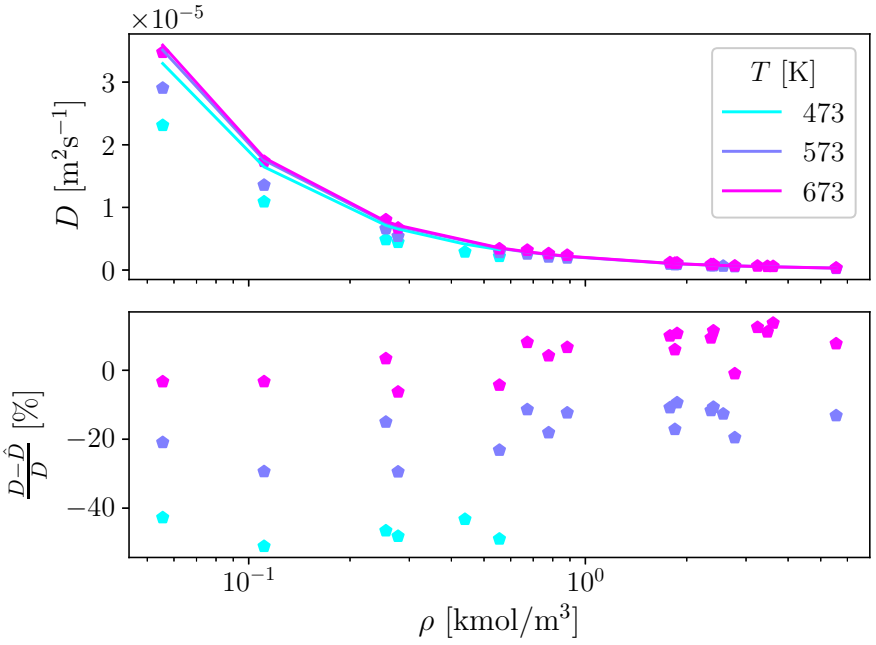

Figure B.2: Self-diffusion coefficient of supercritical water at several isotherms. Lines are predictions by the Enskog solutions with a hard sphere potential, marks are data reported by Yoshida et al.[57]

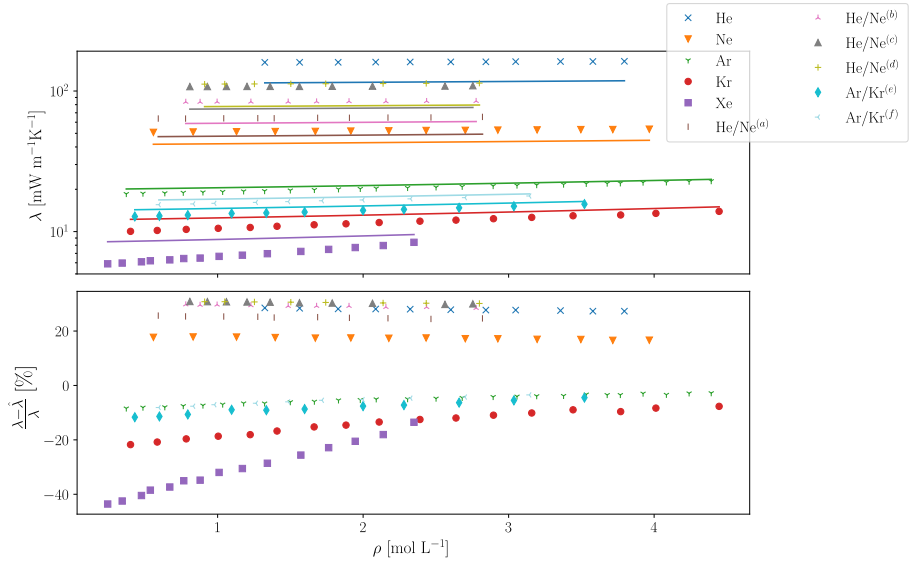

Figure B.3: Conductivity of noble gases and noble gas mixtures at varying density. Predictions by the Enskog solutions with a hard sphere potential. All measurements at 35 °C. $^{(a)}x_{\mathrm{He}} = 0.2172$, $^{(b)}x_{\mathrm{He}} = 0.4662$, $^{(c)}x_{\mathrm{He}} = 0.6823$, $^{(d)}x_{\mathrm{He}} = 0.7156$, $^{(e)}x_{\mathrm{Ar}} = 0.4088$, $^{(f)}x_{\mathrm{Ar}} = 0.7059$. Measurements reported by Assael et al.[60]

C Evaluating partial molar properties required by the Kempers model

The Kempers model requires several partial molar properties, most of which are directly available in the EoS-package ThermoPack.[32] Here, the quantity $\left(\frac{\partial \mu_i}{\partial x_j}\right)_{T,p}$ is related to other quantities that are directly available.

Begin from the definition of the chemical potential as the derivative of Helmholtz energy and invert the order of differentiation,

$$\left(\frac{\partial \mu_i}{\partial n_j}\right)_{T,p} = \left(\frac{\partial}{\partial n_j}\left(\frac{\partial A}{\partial n_i}\right)_{T,V}\right)_{T,p} = \left(\frac{\partial}{\partial n_i}\left(\frac{\partial A}{\partial n_j}\right)_{T,p}\right)_{T,V}. \tag{C.1}$$

From the total differential of the Helmholtz energy, $dA = -SdT - pdV + \sum_i \mu_i dn_i$,

$$\begin{aligned}
\left(\frac{\partial A}{\partial n_j}\right)_{T,p} &= -p\left(\frac{\partial V}{\partial n_j}\right)_{T,p} + \mu_j \\
\left(\frac{\partial}{\partial n_i}\left(\frac{\partial A}{\partial n_j}\right)_{T,p}\right)_{T,V} &= \left(\frac{\partial \mu_j}{\partial n_i}\right)_{T,V} - v_j\left(\frac{\partial p}{\partial n_i}\right)_{T,V} - p\underbrace{\left(\frac{\partial v_j}{\partial n_i}\right)_{T,V}}_{=0} \\
\left(\frac{\partial \mu_i}{\partial n_j}\right)_{T,p} &= \left(\frac{\partial \mu_j}{\partial n_i}\right)_{T,V} - v_j\left(\frac{\partial p}{\partial n_i}\right)_{T,V}.
\end{aligned} \tag{C.2}$$

The total differential of the chemical potential at constant pressure and temperature is

$$d\mu_i = \sum_j \left(\frac{\partial \mu_i}{\partial n_j}\right)_{T,p,n_{k\neq j}} dn_j. \tag{C.3}$$

Further inserting for the total differential of the mole number of each species yields

$$\begin{aligned}
d\mu_i &= \sum_j \left(\frac{\partial \mu_i}{\partial n_j}\right)_{T,p,n_{k\neq j}} (x_j dn + n dx_j) \\
d\mu_i &= \sum_j \left(\frac{\partial \mu_i}{\partial n_j}\right)_{T,p,n_{k\neq j}} n dx_j + \left(\underbrace{\sum_j \left(\frac{\partial \mu_i}{\partial n_j}\right)_{T,p,n_{k\neq j}} x_j}_{=0}\right) dn \\
&= \sum_j \left(\frac{\partial \mu_i}{\partial x_j}\right)_{T,p,n_{k\neq j}} dx_j
\end{aligned} \tag{C.4}$$

where the second term on the right hand side of the second line vanishes by the Gibbs-Duhem relation, and the partial derivative of interest may be readily identified as $\left(\frac{\partial \mu_i}{\partial x_j}\right)_{T,p,n_{k\neq j}} =$

$n\left(\frac{\partial \mu_i}{\partial n_j}\right)_{T,p,n_{k\neq j}}$. This expression was validated numerically by evaluating the total derivative of μ_i at varying composition and total number of moles.

Vegard Gjeldvik Jervell

The Kinetic Gas Theory of Mie fluids

NTNU
Kunnskap for en bedre verden